2010

Plasma Electrolytic Oxidation (PEO)Coatings on a Zirconium Alloy for Improved Wear and Corrosion Resistance

Ying Chen
University of Windsor

Recommended Citation

Chen, Ying, "Plasma Electrolytic Oxidation (PEO)Coatings on a Zirconium Alloy for Improved Wear and Corrosion Resistance" (2010). *Electronic Theses and Dissertations*. 179.
https://scholar.uwindsor.ca/etd/179

Plasma Electrolytic Oxidation (PEO) Coatings on a Zirconium Alloy for Improved Wear and Corrosion Resistance

by

Ying Chen

A Thesis
Submitted to the Faculty of Graduate Studies
through Engineering Materials
in Partial Fulfillment of the Requirements for
the Degree of Master of Applied Science at the
University of Windsor

Windsor, Ontario, Canada

2010

Plasma Electrolytic Oxidation (PEO) Coatings on a Zirconium Alloy For Improved Wear and Corrosion Resistance

by

Ying Chen

APPROVED BY:

Dr. V. Stoilov

Department of Mechanical, Automotive and Materials Engineering

Dr. A. Fartaj

Department of Mechanical, Automotive and Materials Engineering

Dr. X. Nie, Co-advisor

Department of Mechanical, Automotive and Materials Engineering, Advisor

Dr. D.O. Northwood, Co-advisor

Department of Mechanical, Automotive and Materials Engineering, Advisor

Dr. H. Hu, Chair of Defense

DECLARATION OF CO-AUTHORSHIP/PREVIOUS PUBLICATIONS

I hereby declare that this thesis incorporates material that is the result of a joint research undertaken under the supervision of professors Derek O. Northwood and Xueyuan Nie. The research collaboration is covered in Chapter 4 and 5 of the thesis. In all cases, the key ideas, primary contributions, experimental designs, data analysis and interpretation, were performed by the author, and the contributions of the co-authors was in the capacity of supervision of the research in the form of technical advice and suggestions.

I am aware of the University of Windsor Senate Policy and Authorship and I certify that I have properly acknowledged the contribution of other researchers to my thesis, and have obtained written permission from each of the co-authors to include the above materials in my thesis.

I certify that, with the above qualification, this thesis, and the research to which it refers, is the product of my own work.

This thesis includes 2 original papers that have been previously published/submitted for publication in peer reviewed journals, as follows:

1. Y. Chen, X. Nie & D. O. Northwood, Plasma Electrolytic Oxidation (PEO) coatings on a zirconium alloy for improved wear and corrosion resistance, WIT Transactions on Engineering Sciences, 66(2010)183-194.

2. Y. Chen, X. Nie & D.O. Northwood. Investigation of Plasma Electrolytic Oxidation (PEO) coatings on a Zr-2.5Nb alloy using high temperature/pressure autoclave and tribological tests, Surface & Coatings Technology (2010), In Press. doi: 10.1/j.surfcoat.2010.08.038.

I certify that I have obtained permission from the copyright owners to include the above published materials in my thesis. I certify that the above material describes work completed during my registration as a graduate student at the University of Windsor.

I certify that, to the best of my knowledge, my thesis does not infringe upon anyone's copyright nor violate any proprietary rights and that any ideas, techniques, quotations, or any other material from the work of other people included in my thesis, published or otherwise, are fully acknowledged in accordance with the standard referencing practices. Furthermore, to the extent that I have included copyrighted material that surpasses the bounds of fair dealing within the meaning of the Canada Copyright Act, I certify that I have obtained a written permission from the copyright owner(s) to include such material(s) in my thesis.

I declare that this is a true copy of my thesis, including any final revisions, as approved by my thesis committee and the Graduate Studies office, and that this thesis has not been submitted for a higher degree to any other University or Institution.

ABSTRACT

A Plasma Electrolytic Oxidation (PEO) process was used to produce thin oxide coatings on a Zr-2.5wt%Nb alloy. Effects of current density on surface morphologies and wear properties of PEO coatings were investigated and compared to the substrate and the black oxide coating. Corrosion properties at ambient and high temperature/pressure conditions were studied using potentiodynamic polarization tests and autoclave tests, respectively. Autoclave tests were carried out at 300°C and 10MPa in 0.05M LiOH solutions. After the autoclave tests, PEO coatings had larger weight gains in the first 10-day-exposure than the black oxide coating. However, the black oxide coating exhibited a similar weight gain to PEO coatings after the tests. PEO coatings prepared at low current densities had lower weight gains. Although the black oxide coating exhibited a good corrosion resistance, it had a much lower wear resistance than the PEO coatings.

DEDICATION

To My Parents,

Jianping Chen and Zhiyin Chen,

For their endless support, encouragement, and love

ACKNOWLEDGEMNTS

I would like to express my whole-heartedly gratitude to Dr. Xueyuan Nie and Dr. Derek. O. Northwood both, for their instructive and excellent supervision during my studies and research work, as well as their kindness and patience.

I also wish to thank Mr. John Robinson for his generous technical help in machine building, sample preparationm and XRD and SEM analysis.

Special thanks are given to my group members, Dr. Linlin Wang, Junfeng Su, Peng Zhang and Dr. Riyad Hussein for their selfless help and suggestions

Last but not least, my deepest love and gratitude to my beloved parents, Jianpin Chen and Ziyin Chen, whose spiritual presence was a constant inspiration for continuation.

TABLE OF CONTENTS

LIST OF TABLES

LIST OF FIGURES

Chapter 1: INTRODUCTION

1.1 Motivation

Canada's leading role and eminent accomplishments in nuclear development now span more than half a century. The structural material used in the core section of atomic reactors, as well as the fuel-element cladding, should absorb as few thermal neutrons as possible. Zirconium has satisfactory nuclear and physical characteristics and good mechanical properties at room and elevated temperatures. It also has good corrosion resistance in most coolants used in nuclear reactors and it can be readily shaped.

In the CANDU-PHW nuclear reactors, Zr-2.5Nb is currently used for the manufacture of pressure tubes because of its low cross sectional neutron absorption, high corrosion resistance, high strength and creep resistance. The Zr-2.5Nb CANDU pressure tubes are heated for 24hr at 400°C in an autoclave to form a black adherent oxide film of ~1 to 2 μm in thickness was produced [1] This thin black oxide film has corrosion protective properties. However, this black oxide could be damaged during the regular refueling process, thus causing hydrogen/oxygen ingression. There is thus the need for a more wear resistant coating that also has improved corrosion resistance.

The surface reaction between the zirconium tubing and the coolant water in nuclear reactors leads to the oxidation of the tubing and the release of hydrogen. The pick-up of hydrogen in zirconium alloys induces embittlement of the tubes due to hydride formation.

This embrittlement is manifest as reduced ductility and crack growth resistance which can shorten the useful lifetime. Therefore, there is a great incentive to minimize the amount of oxidation and hydriding that zirconium alloys experience in reactor. Since the oxide film formed on the surface of zirconium alloys can act as a barrier against hydrogen permeation and further oxidation, the corrosion behavior and the useful lifetime of the zirconium tubes are closely related to properties of the oxide film.

Electrolytic plasma processing (EPP) is a plasma-assisted electrochemical treatment that is both cost-effective and environmentally friendly. This versatile technique can be widely used in metal surface cleaning, metal-coating, carburizing, nitriding, and oxidizing. When EPP is an anodic oxidizing process, it is called plasma electrolytic oxidation (PEO). The technique is basically the anodic polarization of a metal in an aqueous electrolyte except that a much higher voltage is used. A number of studies have examined in the coating formation mechanisms and characteristics of the coating deposited on the metals like Aluminum, Magnesium and Titanium [2-8]. There have been very few studies on zirconium alloys such as Zr-2.5Nb [9, 10].

In this study, Zr-2.5Nb was used as anode in the PEO process and oxidized in a silicate solution. A complex Zr-Si-O ceramic coating with a high adhesion, hardness, and uniform thickness was made on the substrate material. Different parameters (current density, treatment time and concentration of electrolyte) were used during PEO process. About 5 to 6 μm thick coatings were produced in a very short treatment time (<4min). The surface of the PEO coatings was quite smooth compared to the black oxide coating produced commercially. Long PEO treatment times gave thick coatings which would adversely affect heat transfer in reactor. Therefore, a DC power source was used in this study to produce a thinner oxide film.

1.2 Objectives and contents of this study

The objectives of this study were to:

1. Deposit protective silicate coatings on Zr-2.5Nb alloy in Na_2SiO_3 and KOH electrolyte with different concentration ratios and current densities.
2. Characterize the corrosion behavior of different types of PEO coatings and compare with black oxide coating, at both ambient and high temperature and pressure conditions were used.
3. Optimize the PEO process parameters for Zr-2.5Nb in the coating production, based on the observed corrosion and wear behavior.

1.3 Organization of the thesis

This thesis contains seven chapters. Chapter 1 gives introductory information on the usage of Zr-2.5Nb in nuclear industry applications and the need for improved corrosion and wear resistance, and outlines the study plan.

Chapter 2, which is the Literature Review, summarizes the usage of pressure tubes in the nuclear industry and its material development in the last 60 years. Due to the long time, high temperature/pressure and radioactive service conditions, the corrosion resistance properties have assumed significant importance. Furthermore, sliding wear problems resulting from online refueling are a not-insignificant accelerate corrosion. Chapter2 also describes the evolution of the Plasma Electrolytic Oxidation (PEO) process and its applications to light metals such as Al, Mg Ti and Zr.

In Chapter 3, the experimental procedures and instrumentation are described. The results and analysis are given in Chapter 4. Chapter 5 gives the conclusions from the research described in Chapter 4 and presents some suggestions for future work.

Chapter 2: LITERATURE REVIEW

2.1 Introduction to the CANDU nuclear reactor

In Canada, nuclear energy has been utilized for over sixty years in many fields for peaceful purposes: electricity generation, medicine, agriculture, research and manufacturing. The CANDU-PHW (Canadian Deuterium Uranium-pressurized Heavy Water) reactors, which are the current nuclear energy generator, supply 53% of the electricity used in Ontario, 6.1% in New Brunswick, and around 3.0% in Quebec in 2008. The CANDU nuclear power reactor has been operated safely for 50 years.

There were 436 operable nuclear power reactors in 30 countries on April 1, 2009 and there were 44 nuclear reactors under construction, another 108 being planned and 272 being proposed [11].

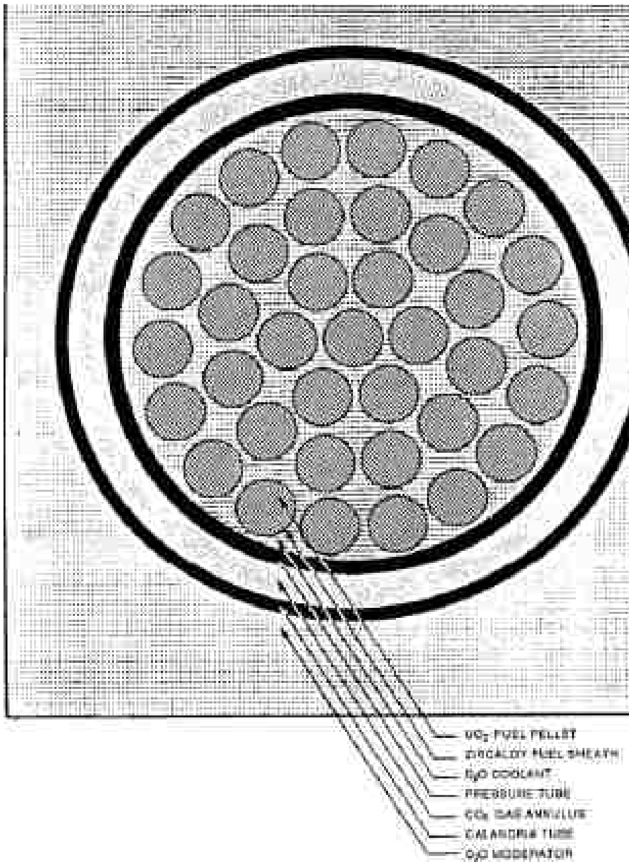

Fig. 2.1 CANDU basic lattice cell for 37-element fuel [12].

The CANDU type reactor was first designed and constructed in Canada. As shown in Fig. 2.1, a CANDU 6 fuel bundle consists of 37 elements, which are arranged in circular rings, and each element consists of sintered natural uranium dioxide (UO_2) cylindrical pellets, which are contained in a Zircaloy-4 sheath closed at each end by an end cap. The fuel elements in a bundle are held together by end plates at each end with spacers providing the necessary separation between the elements. Bearing pads on the outer elements of the fuel bundle provide the necessary separation between the outer elements and a pressure tube. Each pressure tube in a CANDU 6 (Fig 2.2) contains 12 fuel bundles (500 mm long) each and contains heavy water coolant, which is thermally insulated from a low-pressure cool moderator by a gas annulus formed between the pressure tube and the calandria tube surrounding it. The calandria tube contains D_2O moderator at 70°C, and is penetrated by 380 horizontal fuel channels each six meters long. Each channel consists of a pressure tube containing fuel and coolant D_2O at a temperature ranging from 250-270° C at the inlet to 290-310° C at the outlet. The inlet pressure is about 10.5MPa and the outlet pressure is about 9.9MPa, resulting in an initial axial stress in the pressure tube wall of about 65MPa and an initial hoop stress that varies from about 130MPa at the inlet to about 122MPa at the outlet. The coolant pH is maintained in the specified range 10.3 as a result of the addition of LiOH, and the recommended range for dissolved deuterium is 3 to 10 cm^3 D_2/kg deuterium oxide (D_2O). Two end-fittings at each end of the fuel channel incorporate a feeder connection through which pressurized heavy water coolant enters and leaves the fuel channel. The feeders are connected to the reactor inlet and outlet headers. A CANDU 6 has two independent loops, containing 190 fuel channels in each loop and four steam generators with two in each of the loops. The fission heat produced in the fuel is transferred to the light water in the secondary side of the steam generators to produce steam, which drives the turbine generators to produce electricity [13, 14].

The safety of the CANDU pressure tube is based on the “leak-before-break” criterion [15]; namely, the critical crack length is sufficiently large that coolant leakage will be detected before the crack grows to the critical unstable length.

Fig. 2.2 (a to c) are schematics of the CANDU-PHW reactor core, fuel channel and a transverse view of the fuel bundles, respectively.

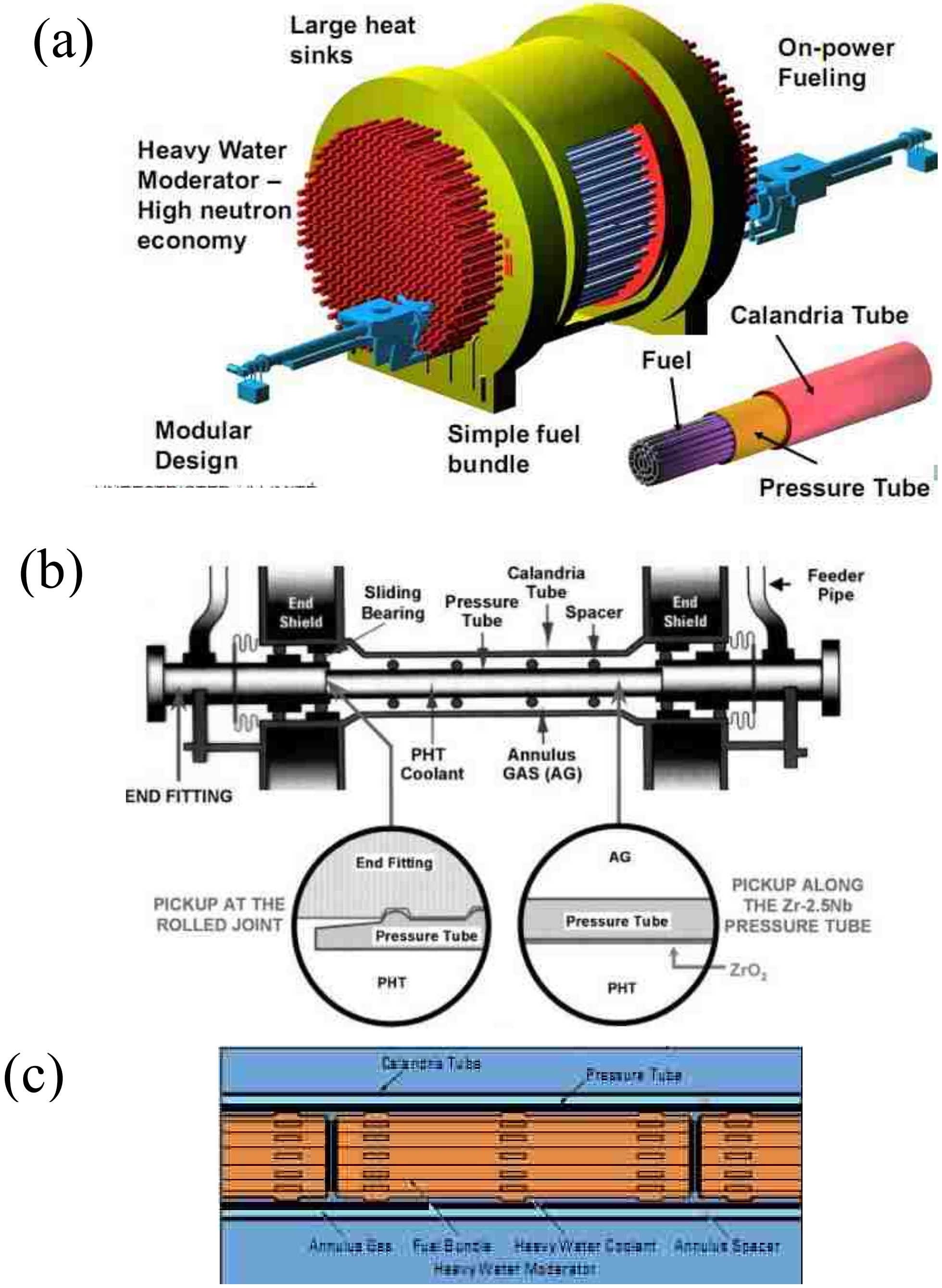

Fig. 2.2 CANDU-PHW reactor core, the fuel bundle and how a fuel bundle settled inside the pressure tube [16].

2.2 Development of pressure tubes in CANDU nuclear reactor

The pressure tube, which was first manufactured in 1957, is a major component of the CANDU reactor, which supports the nuclear fuel bundles and heavy water coolant. Early CANDU reactors—Nuclear Power Demonstration (NPD) Douglas Point, and Pickering 1 and 2—used Zircaloy-2. The Zr-2.5Nb alloy was selected for Pickering 3 and 4 because it had a better in-reactor creep resistance and its higher strength permitted the use of a thinner wall tube with a resultant advantage in neutron economy over Zircaloy-2. Zr-2.5Nb has been used in all subsequent CANDU reactors [17].

Zriconium-based alloys are commonly used to manufacture nuclear reactor components since they have a low neutron absorption cross section, high strength and high corrosion resistance under operating conditions [18]. It was initially thought that the poor corrosion resistance of some batches of unalloyed zirconium produced by the van Arkel process was a result of stray impurities. However, it was found that improving the purity did not eliminate these problems.

During the initial years of exposure to the reactor environment, the zirconium alloys exhibit a rather constant and low rate of corrosion and hydrogen uptake [1]. Fig. 2.3 (a) shows that Zircaloy-2 tubes start to corrode at a faster rate after a period of about five effective full power years, as evidenced by the rate of change of oxide thickness on the tubes and amount of deuterium in the tubes. Data measured in Wolsong-1—one of the CANDU type reactors, reactor shows that Zr-2.5Nb exhibits a much lower hydrogen/deuterium-pick-up rate than for Zircaloy-2 (Fig. 2.3 (b)).It has been proposed that when the oxide is thin, D_2 in the coolant can penetrate the oxide to suppress the oxidizing species formed in the oxide pores by radiolysis. This suppression cannot occur when the oxide reaches a critical thickness of 15-20μm (larger than the deuterium penetration range), resulting in an increase in the oxidizing power of the electrolyte in the pores and an increase in the rate of corrosion. One criticism of this explanation for increased corrosion rates with time is that after a certain oxide thickness is reached and a porous oxide layer (post-transition oxide) forms, deuterium is plentiful and present at the bottom of all pores, provided less than 100% of the deuterium evolved during the cathodic reaction is absorbed by the metal. Whatever the explanation of this acceleration in Zircaloys, Zr-2.5Nb tubes do not exhibit this phenomenon to the same extent. Also, the second phase particles present in Zircaloys, but not in Zr-2.5Nb, have been blamed for this acceleration of attack because they apparently act as preferred sites for deuterium evolution and pickup. As a result, the Zircaloy-2 pressure tubes in CANDU reactors have been replaced with Zr-2.5Nb [19].

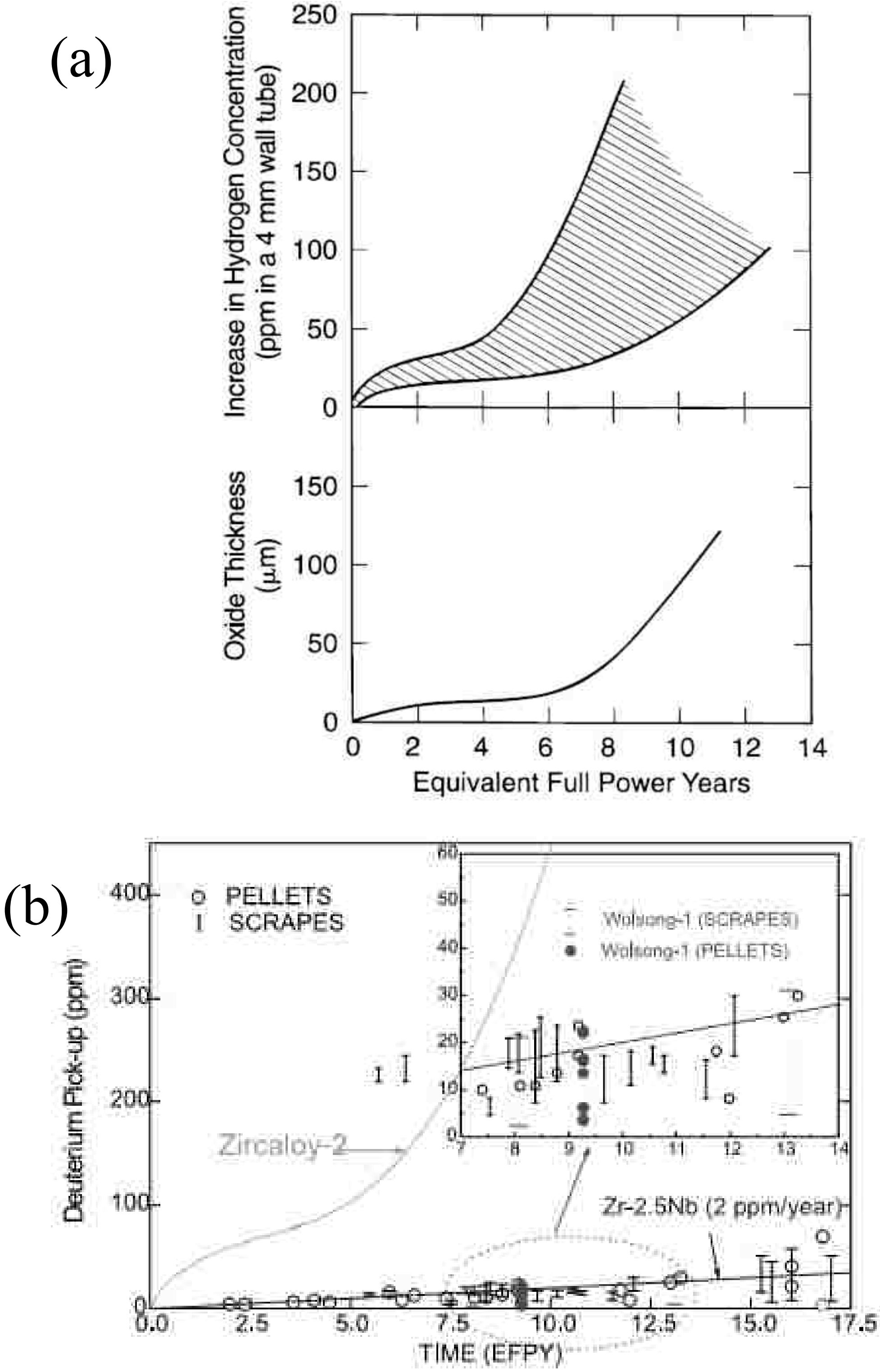

Fig. 2.3 (a) The corrosion and hydrogen increase in Zircaloy-2 pressure tubes after reactor service and (b) Deuterium concentration in Zircaloy-2 and Zr-2.5Nb pressure tubes including Wolsong-1 reactor [18].

It is very important to note, however, that the reason that the pressure tube concept was viable is the use of zirconium and its alloys. In the pressure-tube design, there is a large mass of metal inside the reactor, which could absorb a significant amount of neutrons. This would definitely be the case with steel pressure tubes–the fission chain reaction could not be made self-sustaining, on account of the large neutron absorption by the steel. Fortunately, zirconium, which is a "magic" nuclide with a very low neutron-absorption cross section, came on the scene in time for application in NPD. Incidentally, this "coming to the fore" of zirconium was as the result of materials research in Chalk River for the US nuclear program [12].

2.3 Fabrication of pressure tubes in the nuclear plant

The production route for Zr-2.5Nb pressure tube is a multi-step process involving forging of the ingot, machining of hollow billets, extrusion and cold drawing. Fig. 2.4 is an abridged flow diagram showing the main steps in the fabrication of Zr-2.5Nb pressure tubes. By autoclaving at 400° C for 24hr, a protective oxide layer is formed on the both inner and outer ring surfaces.

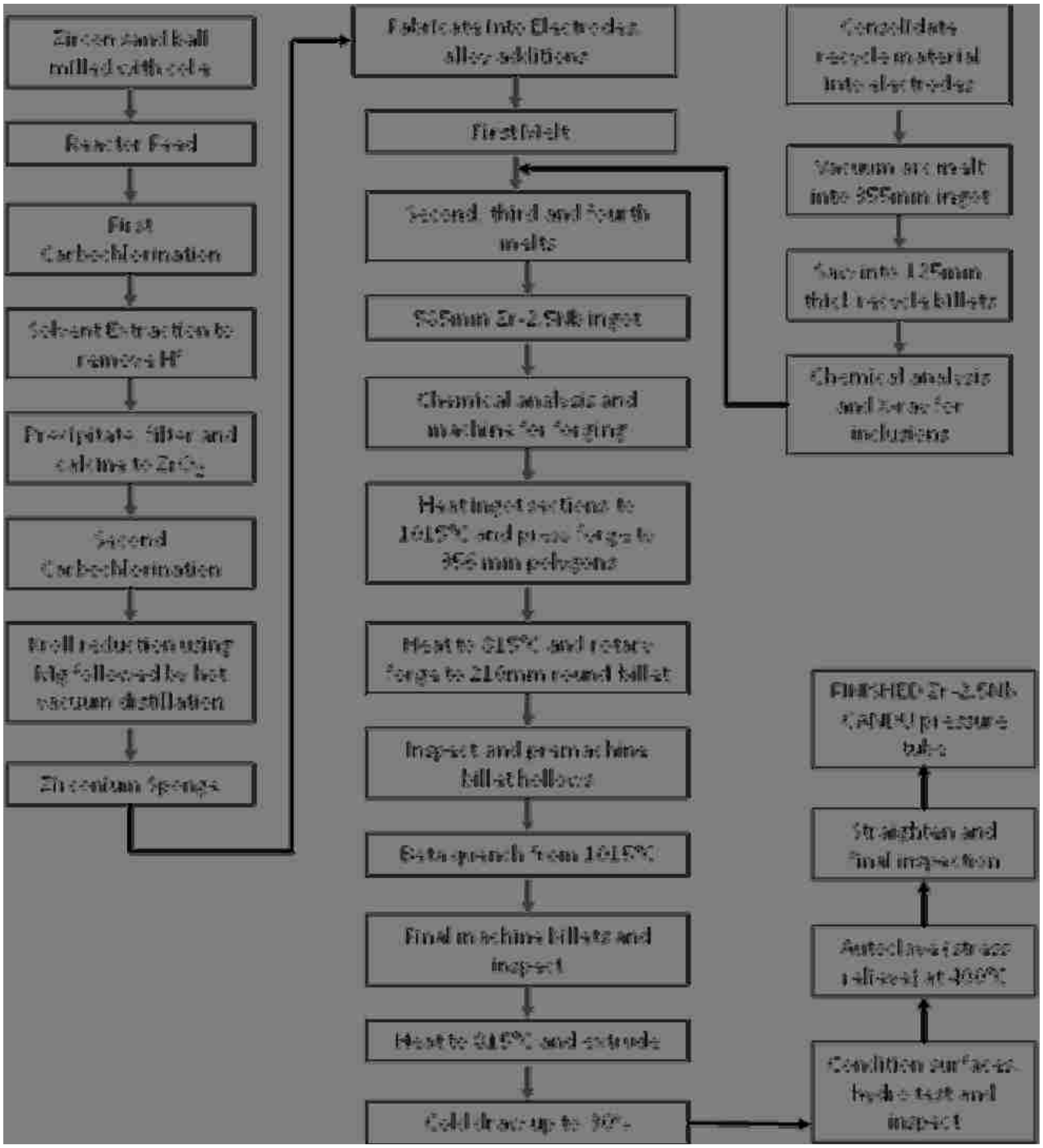

Fig. 2.4 Abridged flow chart for the fabrication of CANDU Zr-2.5Nb pressure tubes [20].

The tubes are fabricated by hot-working ingots in (α+β)-phase region. These ingots are machined to produce hollow billets that are approximately 560mm long × 195mm diameter suitable for extrusion. After water-quenching from the β-phase the hollow billets are extruded at 815°C, they are then cold-drawn about 27% to give a final tube length of

6.3 m with a final thickness of about 4.3mm and an inside diameter of about 104 mm. The tubes are stress-relieved at 400°C for 24hr prior to installation in a CANDU reactor [21]. The microstructure consists of elongated grains of hexagonal-close-packed (hcp) α-Zr, partially surrounded by a thin network of filaments of body-centered-cubic (bcc) β-Zr. The alpha-phase grains are platelets (containing about 0.6 to 1 wt% Nb in solution) with aspect ratios of about 1, 10, and 40 in the radial, transverse and longitudinal directions, respectively. A typical microstructure is illustrated in Fig. 2.5.

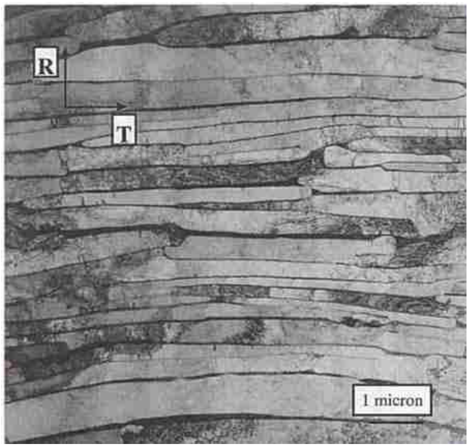

Fig. 2.5 Typical grain structure in Zr-2.5Nb pressure tubing looking down the axis of the tube. The light colored α-phase platelets are interspersed with dark-colored β-phase filaments [22].

From the Fig. 2.5, we can clearly see that the α-grains are stacked together and are separated by a non-equilibrium β-phase containing about 20 wt% Nb: see Fig.2.6 for the Zr-Nb binary phase diagram. As can be seen in Fig. 2.6, the solubility limit for Nb in α-Zr, has been given as low as 0.6wt%. At high temperatures (>~880°C), Zr-2.5Nb is single phase, having the bcc β-Zr structure with the Nb being in solution. On slow (equilibrium) cooling to room temperature, a two phase, α- Zr and β-Nb, structure is produced. The α-Zr phase is hcp with the Nb being in solution. The β-Nb phase is bcc structure containing ~85wt%Nb. The width of the β-phase in the radial direction is about one-tenth that of the α-phase. The width of the α-phase is typically about 0.3 μm. This microstructure greatly affects the growth of oxide on its surface.

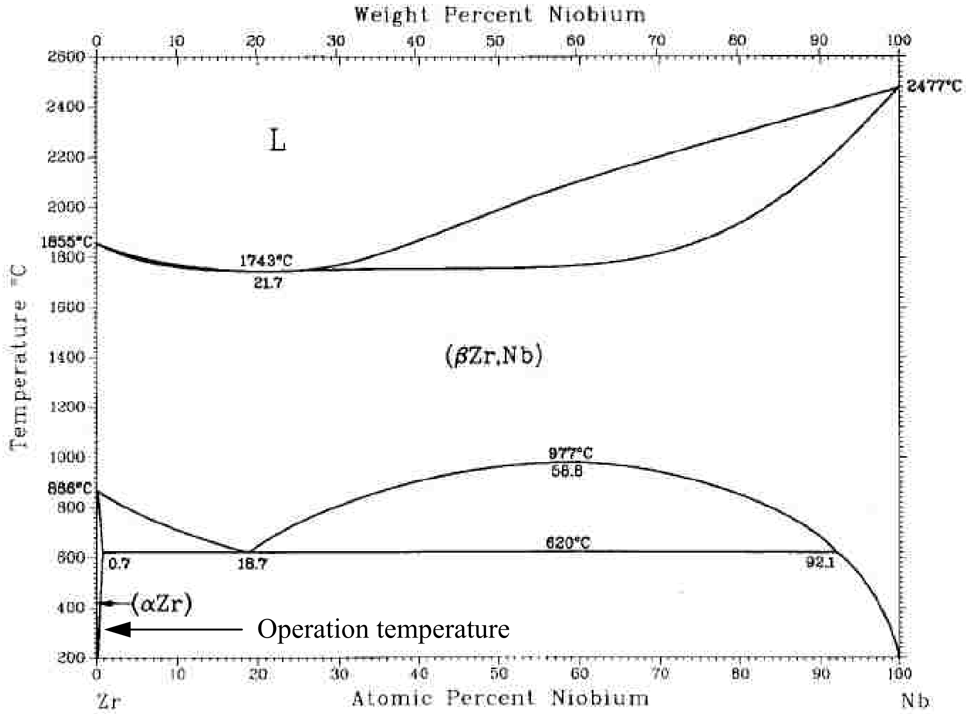

Fig. 2.6 Schematic Zr-Nb binary phase diagram [23].

The correlation between the microstructure of pressure tubes and the corrosion behavior has been studied in detail by many researchers [24-26]. It was believed that a full understanding of the corrosion mechanism of zirconium alloys requires an in-depth analysis of the reasons affecting the microstructural features of the oxide film. However, complex interactions of parameters in the process of the growth of oxide film make it difficult to predict corrosion behavior of zirconium alloys. The studies focusing on the microstructures of the oxide film and their relations to the corrosion often lead to results that seem to contradict each other [27-34].For example, it is generally accepted that high compressive stress near the oxide/metal interface may produce a high tetragonal phase fraction in the oxide film, but very recent studies show that there seems to be no obvious correlation between the compressive stress and the tetragonal phase fraction [27, 28]. Some authors observed that zirconium alloys with a high tetragonal oxide fraction near the interface exhibit a higher corrosion rate, whereas in other papers completely different results have been reported [27, 29-31]. Yilmazbayhan et al. [29], Bossis et al. [32] and Bechade et al. [33] found higher percentages of tetragonal oxide in Zircaloy-4 than in Zr–1% Nb, whereas Vrtilkova et al. reported a high value of the tetragonal phase fraction in Zr–1% Nb but very low value in Zircaloy-4 [34]. Despite numerous studies undertaken by different authors, many questions still remain open. To date, it has been difficult to predict the corrosion behavior of zirconium alloys as there is no unified or overall model that may clarify the intrinsic factors affecting the microstructural aspects of the ZrO_2 film.

2.4 In-reactor deformation of pressure tubes in CANDU reactor

2.4.1 Life-limiting factors for a pressure tube

The service life of a pressure tube is determined by the allowable dimensional changes, by its capability to accommodte dimensional changes, by its capability to resist crack initiation and, as defence in depth, by its ability to meet a leak before break criterion developed for the tubes. Four factors are important in the pressure tube's degradation (aging) during service [14, 21]:

(i) Dimensional changes,

(ii) Corrosion and hydrogen ingress,

(iii) Changes in mechanical properties,

(iv) Flaw development.

2.4.2 Methods to reduce the degradation during service

In this case, methods for improving the pressure tube performance can be divided into the following five categories [35]:

(v) minimizing the variation of the pressure tube's dimension (diameter, length),

(vi) decreasing the defects at which DHC(delayed hydride cracking) can be initiated,

(vii) increasing the fracture toughness of the pressure tube,

(viii) decreasing the corrosion rate and

(ix) minimizing hydrogen uptake.

Localized oxidation caused some small regions (most of which, are grain boundaries) exhibit a much higher corrosion rate. After a certain period of corrosion, especially in high temperature/pressure condition, the initiation of small cracks could be the origins of disastrous ‘break-away’ of the corrosion rate.

Whether serendipitously or not, this problem was solved by the addition of transition metals (Cr, Fe, Ni), that were largely insoluble in the zirconium matrix and appeared as small particles of intermetallic phases, and tin which was soluble in zirconium and which nullified the negative effects of the nitrogen impurity present in the Kroll process zirconium [36].

Dimensional changes are controlled by thermal and irradiation creep and by irradiation growth. These phenomena cause diametric and length increases in the tube and pressure tube sag. To reduce dimensional variation, to minimize the defect and to increase the fracture toughness, manufacturing processes should be modified. Corrosion leading to metal loss on the inside of the tubes is a result of contact of the metal with the hot, pressurized heavy water. Furthermore, the gradual build-up of deuterium in the tubes as a result of corrosion, combined with the possibility of the generation of flaws of sufficient depth, makes the tubes susceptible to the initiation of delayed hydride cracking (DHC). The hydrogen and deuterium uptakes and the concomitant DHC are the most important factors in the lifetime of a pressure tube. Fig.2.7 gives an example of a failed pressure tube during service.

Fig. 2.7 Though-wall crack in a CANDU Zr-2.5Nb pressure tube, showing oxidized crack growth bands. The crack initiated at the inside surface just inboard of the rolled joint [37].

To prevent DHC, hydride formation should be avoided. Since the solubility limit of hydrogen in zirconium is low, hydrogen concentration in the pressure tube must be lowered in order not to form hydride. Hydrogen is partially absorbed during pressure tube manufacturing process but most of it is picked up during operation （see Fig. 2.3）[1, 38, 39]. To prevent ingress of hydrogen into the pressure tube during operation, several methods have been studied such as forming a black oxide layer about 1 μ m thick by autoclaving for 24hr at 400° C before installation, changing the microstructure of the pressure tube surface using laser or shot peening, adding some elements such as Fe, V and Cr which are known to have beneficial effects in reducing hydrogen uptake, and coating a thin stress-free zirconium oxide layer on the pressure tube. Among these methods, the ZrO_2 coating technologies are preferred since an oxide layer grown by this method contains very few cracks.

These corrosion resistance properties are dependent on the microstructure of the pressure tubes and thus are a function of the manufacturing process and operating conditions (radiation damage). Northwood and Kosasih [40] summarized the problems of the pressure tube performance in reactor as follows: “Obviously any change in the mechanical processing route to enhance dimensional stability will also change the microstructure which will in turn affect other properties in addition to irradiation growth and irradiation creep. One property that would change is the corrosion resistance and the associated problem of hydriding. During reactor operations there is a corrosion reaction between the zirconium alloy pressure tube and the heavy water moderator/coolant. As a result of this corrosion reaction there is a release of hydrogen (deuterium) and this can be “taken up” by the pressure tube material. Hydrogen pick-up above a certain level will give rise to solid hydrides at reactor operating temperatures. These hydrides are subject to brittle fracture, particularly when the reactor is shut-down (cooled down).”

In the research study forming the basis of this thesis, the corrosion behavior is one of the key points of concern.

2.5 Corrosion characteristics of zirconium and its alloys

The elevated-temperature aqueous corrosion and associated deuterium uptake of Zirconium alloy nuclear reactor pressure tubes have been studied for over 50 years [11, 41]. Zircaloy tubes exhibited rapid deuterium ingress after a period of in-reactor exposure, and have been replaced with tubes fabricated from the more resistant Zr-2.5Nb alloy. Investigations of the behavior of Zr-2.5Nb in water and steam at high temperatures indicate that the material has quite good corrosion resistance.

During the initial period of oxidation, the surface of the metal is covered by a thin black protective film which adheres well. During this period, the rate of oxidation can be represented by a curve that approaches parabolic, cubic or logarithmic form. When the thickness of the oxide film reaches a certain limit, there is an abrupt change in the corrosion resistance. In a relatively short time, the oxide film changes its color to gray or white and becomes friable, and spalling occurs. The oxidation rate increases and conforms to an almost linear law.

Because of the shape of the curve, the change in corrosion resistance is often called “breakaway” or “transition” and the moment at which the change occurs is called the “breakaway point” or “transition point”.

The exact moment of transition during the corrosion of Zr-2.5Nb and other zirconium alloys depends on a number of different factors, which are often difficult to predict quantitatively. This phenomenon is characteristic of zirconium and its alloys, and limits the life of the metal. In the nuclear industry, the pressure tubes in CANDU reactors have been operating for times up to about 25 years.

The basic reaction of the zirconium alloy with the corrosive medium, H_2O (D_2O), can be represented by the following equation [40, 42]:

$$Zr + 2H_2O \rightarrow ZrO_2 + 2H_2 \tag{2.1}$$

However, the basic mechanisms are much more complex and three regions should be considered, that is, the metal, the oxide, and the corrosion medium. This is illustrated in

Fig.2.8:

H_2O

______________________ Interface II

Oxide (ZrO_2)

______________________ Interface I

Metal (Zr)

Fig. 2.8 Three regions separated by two interfaces in the corrosion area.

The growth of the oxide layer is considered to involve the diffusion of oxygen ions and anionic vacancies (oxygen ions missing from lattice which carry an effective charge of 2^+ and are represented by the symbol $\square^{2+}$). The reaction of note at the interface II, the interface between the corrosive medium and the oxide can be represented by the equation:

$$\square^{2+}+2e^-+H_2O \rightarrow O_2+2H^+ \tag{2.2}$$

This reaction leads to the formation of hydrogen ions (protons) and oxygen ions. The oxygen ions diffuse in and react with the metal (Zr) at interface I to form oxide, electrons, and anionic vacancies as shown by the following equation

$$Zr+2O^{2-} \rightarrow ZrO_2+2\square^{2+}+8e^- \tag{2.3}$$

These electrons and anionic vacancies diffuse out to continue the corrosion process. It is to be noted that for zirconium that the oxidation proceeds by the diffusion of oxygen ions into the oxide and not by diffusion of the metal out through the oxide. It is the electrons and anionic vacancies that are diffusing out through the metal. Having an aqueous solution such as LiOH rather than pure water changes the corrosion characteristics and reactions only through its effect on the nature of the oxide film. With Li ions being incorporated into the ZrO_2 film there is an increase in the number of anionic vacancies which gives rise to faster rates of diffusion for the oxygen ions and hence a higher rate of corrosion [40].

The ZrO_2 film formed on the pressure tube surface serves as a protective layer to limit further oxidation. While most of the 'corrosion-generated' deuterium combines to form D_2 and is released into the coolant, a small fraction (2-10%) is absorbed by the underlying metal substrate. Over time, the deuterium concentration increases, and high levels of deuterium in the pressure tube can have negative effects on its mechanical properties, e.g., reduced fracture toughness. If the deuterium concentration exceeds the terminal solid solubility in the zirconium alloy, brittle hydrides (deuterides) can precipitate and cause problems related to delayed hydride cracking (DHC) and hydrogen blister susceptibility.

2.5.1 The kinetics of the oxidation of corrosion of zirconium and its alloys

As mentioned in section 2.5, the growth of the zirconium oxide is controlled by inward oxygen diffusion through the oxide thin film, so that the thicker the oxide film, the more difficult the oxygen diffusion is. Therefore, the thickness of the oxide layer plays an important role in the control of the oxidation kinetics. Moreover, the existence of defects in the oxide is also related to the oxidation kinetics.

Pure zirconium has quite good corrosion resistance. The presence of impurities and alloying elements, the addition of which is necessary to increase the strength, leads to a reduction in the corrosion resistance. The kinetics of the reaction of zirconium with water or steam is generally characterized by two periods [43]: During the first period, an adhering protective oxide film is formed. This film is either black or an iridescent color. The weight gain of the specimen is governed by the laws applying to metals that form a protective layer of corrosion products. After a certain time, the second period begins. The corrosion rate sharply increases, and in place of the black protective film, the metal becomes covered with a white or light grey, friable, spalling oxide. During the second period, the corrosion rate of zirconium is usually very high, and rapid failure of the metal occurs. The characteristic change in the oxidation rate of zirconium and its alloys is often called ‘transition’ or ‘breakaway’. The duration of these two periods can change, depending on the conditions under which oxidation occurs (temperature, pressure, time, etc.).

The steady corrosion of zirconium during the first period may be represented by the equation:

$$\Delta m = kt^n \tag{2.4}$$

or in logarithmic coordinates

$$\lg\Delta m = k + n\lg t,, \tag{2.5}$$

where Δm is the weight gain of zirconium due to the formation of the oxide film, after a period of t.

2.5.1.1 Pretransition period

The oxidation curve of zirconium and its alloys in water or steam for the pretransition period can be divided into two stages.

For a relatively short time, the surface of the zirconium is actively oxidized and covered by a protective oxide film. As the thickness of the film and its protective property increase, the oxidation slows down and becomes a constant rate. The minimum thickness of the oxide film necessary to protect the metal, and at which the corrosion rate becomes stable, is dependent on a number of factors including: temperature, pressure, nature of the corrosive medium, and the chemical composition and structure of the alloy.

After an oxide film of a certain minimum thickness has formed, the corrosion process stabilizes, and, up to the transition point, it can be represented in logarithmic coordinates by a straight line. The exponent n then determines the oxidation rate and the growth of oxide film.

Values of the constants of the equation of the kinetics of oxidation, characterizing the behavior of zirconium and Zr-2.5Nb in water and steam at various temperatures are given in Table 2.1. An exponent $n=0.3$ characterizes a cubic oxidation rate law; $n=0.5$ characterizes a parabolic and $n=1$ a linear law [36, 43]. Table 2.1 shows that Zr-2.5Nb will corrode under a relative low rate—parabolic corrosion law when using pure water as the corrosion medium.

Table 2.1 Constants of the kinetics of the oxidation of zirconium and Zr-2.5Nb [43].

Alloy	Test conditions			Equation constants $\Delta m = kt^n$	
	medium	Temperature °C	Pressure, atm	k	n
Iodide zirconium	Water	350	168	0.5	0.3
	steam	400	300	0.7	0.38
Zr-2.5Nb	water	300	88	0.2	0.47
		350	168	0.22	0.62

2.5.1.2 The transition

In general it is not possible to grow oxide films on zirconium alloys that are thicker than 2 μm without a change in the kinetics to either an approximately linear or a cyclic kinetic stage (post-transition) that is considered to indicate the development of some sort of porosity in the previously protective oxide [36]. As already mentioned, the corrosion of zirconium and its alloys is characterized by high corrosion resistance during the first period of oxidation, followed by an increase in the corrosion rate, without change of the external factors. This phenomenon reduces the life of zirconium alloys, and introduces an element of uncertainty into choosing alloys for given applications. Since the zirconium alloys are widely used in industry, their corrosion resistance has been the subject of many investigations. The time at which transition takes place depends on the combined effect of different factors. The most important factors are temperature and alloying elements.

(i) Temperature. The higher the temperature, the earlier and clearer is the transition point on the oxidation curve.

(ii) Alloy elements. Alloying zirconium may modify its corrosion resistance considerably. The principal purpose of alloying is to increase the protective properties of the oxide film, and increase the time to transition. The results obtained from tests in steam at 650°C of several zirconium alloys are given in Table 2.2. From Table 2.2, we can find that Zr-2.5Nb has an insufficient corrosion resistance property at high temperature: However, we are not using Zr-2.5Nb at temperatures as high as 650°C

Table 2.2 Corrosion tests on zirconium alloys in steam at 650°C [43].

Alloy	Time to transition, hr	Weight gain mg/dm^2	Corrosion rate after transition, $mg/(dm^2 \cdot day)$
Zircaloy-2	4	100	30
Zr-1%Nb	20	200	17
Zr-2.5%Nb	5	110	18
Zr-2.5%Nb-0.5%Sn	2	100	40
Zr-1.0%Cu-1.5%Mo	360	400	20
Zr-0.5%Cu	300	400	16
Zr-0.5%Cu-0.5%Mo	700	700	/

During the transition period, an open network of pores that permits direct access O_2

or H_2O to the metal surface is formed. Some amount of the t-ZrO_2, which is still present in the dense layer before the transition occurs, transforms to m-ZrO_2. This was explained by Beie et al.[44] as being due to two reasons: first, the tetragonal phase within the dense layer may be stabilized by the large compressive stress that is relieved at the transition. The second reason may be the increased concentration of hydrogen that favors the m-ZrO_2.

Transition is a complex process, being dependent on the combined effect of many factors. To determine the suitability of a zirconium alloy for service, prolonged corrosion field tests must be carried out, since the extrapolation of short-time tests is unreliable and often unacceptable, because of the possibility of breakaway taking place. In order to study and simulate the long-term corrosion/hydriding behavior of the pressure tubes in reactor, there is a method which has been proven to be suitable and is accepted and used by many researchers in this field, that is the autoclave test [40]. In this test, pressure tube material is put in pressurized lithium hydroxide solution at 300°C. The purpose of this investigation is to study the effect of various thermo-mechanical processing schedules on the corrosion/hydriding behavior as exhibited in these accelerated corrosion tests in pressurized lithium hydroxide solution. In this thesis, this method is also used to study the corrosion behavior of PEO-coated Zr-2.5Nb samples and black oxide-coated samples under high temperature and pressure. A high concentration of lithium hydroxide was used to shorten the experimental time. However, due to the limitations of laboratory instrumentation and safety concerns, irradiation simulation is not included in our research.

2.5.1.3 Post-transition period

The post-transition period in the oxidation of zirconium commences when a white or grey spalling oxide is formed on the surface. This period is characterized by rapid oxidation and failure of material. The oxidation rate during this period is determined only by the rate of ingress of oxygen to the surface of the metal, and by the thermodynamic conditions applying to the reaction between zirconium and oxygen. For zirconium and most of its alloys, the oxidation rate during the post-transition period follows a linear or near-linear law. It was believed that the transition limits the service life of pressure tube, and that after transition has occurred the metal is unserviceable. The formation of a porous oxide film leads to rapid continuous corrosion, to failure of the metal part, and to contamination of reactor coolant with oxidation products and fuel.

After the transition point, the corrosion kinetics, the oxide morphology and oxide/metal interface topography of the corroded samples show great differences to those in the pre-transition period. Ding and Northwood [45] comprehensively compared by SEM oxide/metal interface of Zr-2.5Nb alloy formed in aqueous corrosion medium before and after transition. Groups of Zr-2.5Nb coupons were corroded in a pressurized solution of 4.8g LiOH per liter deionzied water at 300°C. After study of the weight gain vs. exposure time curve, the transition point was found to be taken place after about 80hr of exposure. Samples which made before and after that certain time were cut and etched to remove metal close to the oxide/metal interface and finally examined using SEM from different directions. Fig. 2.9 (a) and (b) show the SEM micrographs taken from the axial direction of a pressure tube.

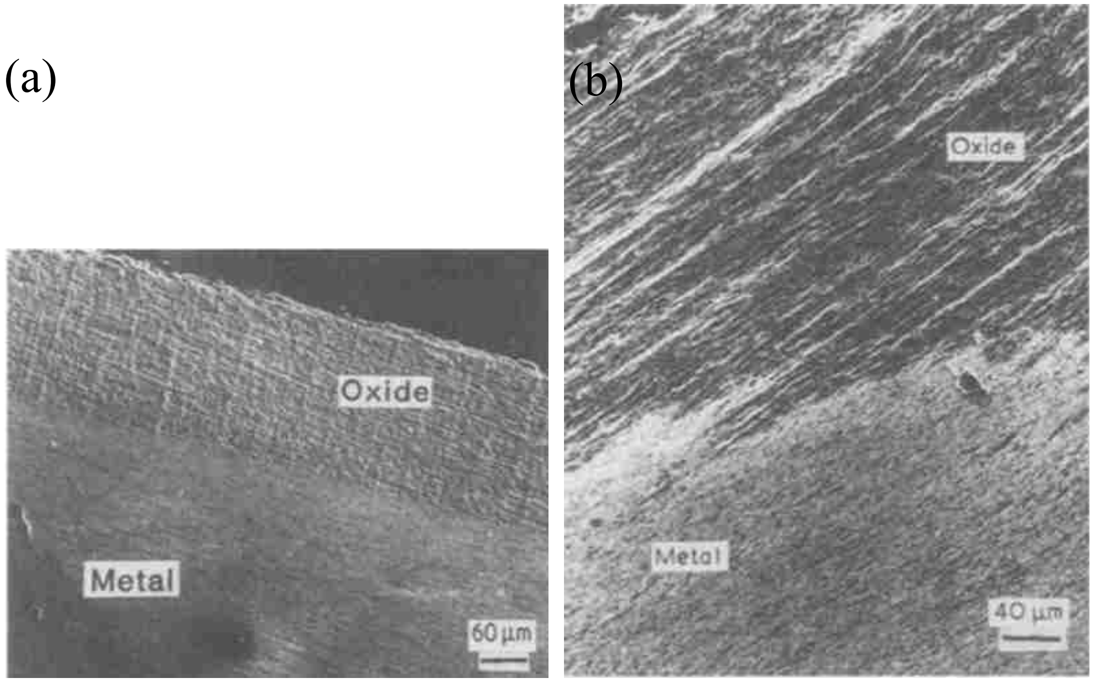

Fig. 2.9 (a) Micrograph of a pre-transition (40hr) sample showing uniform oxide layer and (b) Micrograph of a post-transition (480hr) sample showing a non-uniform oxide layer [45].

From Fig 2.9, it can be seen that a uniform thick of oxide layer was formed on the pre-transition sample and that the oxide layer which formed on the post-transition sample was not uniform. This was explained by the fact that there were different corrosion rates at different locations in the post-transition samples.

2.5.2 The Phase-Transformation theory and failure of oxide film

There are three different phase structures of zirconium dioxide which exist in different temperature ranges from room temperature to over 1300°C. They are the monoclinic phase, the tetragonal phase and the cubic phase [43].

Some research [24-26] have been carried out in order to gain an insight into the formation and growth of the oxide layer. These researchers emphasize the importance of the microstructure and composition of oxide film and attempt to relate corrosion resistance to the presence of the tetragonal zirconium oxide phase in the oxide layer.

On the basis of electron-diffraction analysis and kinetic investigations, Korobkov et al. [43] have developed a theory to describe the dependence of the corrosion resistance of zirconium on the phase transformations taking place in the oxide film. The authors investigated the oxidation of thin (300-400 Å) foils of zirconium and zirconium alloys, which had been prepared by evaporation and condensation in a high vacuum (approximately 10-7 mmHg). It was found that thin zirconium foils heated in air at temperatures in the range of 270-650°C were fully oxidized. The oxide had a cubic structure with a lattice constant a=5.09Å. Increasing the temperature from 650 to 750°C led to the formation of a tetragonal zirconium oxide, with the following lattice constants: a=5.07Å, c=5.16Å, c:a=1.02. An increase in the temperature of oxidation from 750 to 1,100°C led to the formation of a mixture of tetragonal an monoclinic forms, while at temperatures from 1,100 to 1,300°C, only monoclinic zirconium dioxide (ZrO_2) was formed. The lattice constants of the monoclinic ZrO_2 were: a=5.17Å, b=5.26Å, c=530Å and β=80°48′. They further found that the transformation from the tetragonal to monoclinic form was dependent on temperature and heating time, and that it took place at a certain thickness of the oxide film, which they called the critical thickness.

Investigations based on Raman spectroscopy and transmission electron microscopy (TEM) confirmed that there are two phases (monoclinic(m) and tetragonal (t) phase) in ZrO_2 film formed on zirconium alloys, and the distribution of tetragonal phases in ZrO_2 film is not uniform. The percentage of tetragonal phase is much higher near the oxide/metal interface than that in the outer oxide layer [18, 41, 46-49]. Electron diffraction patterns and kinetic data showed the conclusion that the acceleration of the oxidation of zirconium is caused by the transformation of tetragonal zirconium dioxide to a monoclinic structure. This view of the mechanism of failure of the oxide film has been confirmed by number of other investigations.

Ding and Northwood [45] have presented another model to explain the corrosion process on Zr-2.5Nb. In the early stages, the oxide is mainly formed from the grain boundary phases, i.e., β-Zr and its decomposition products. The oxide formed from grain boundary phases may be not dense enough to act as a barrier layer, especially the upper oxide layer. Oxidation of the α-Zr grains may form a dense protective oxide barrier—this oxide is predominantly t- ZrO_2. With the progress of corrosion, all the t- ZrO_2 transformed into monoclinic phase and formed a porous oxide outer layer and only the ‘freshly’ corroded tetragonal phase can be kept at the interface.

Fig. 2.10 is. schematic illustration of the process occurring during the oxidation of Zr-2.5Nb in an aqueous environment (left) corrosion on α-Zr; (right) boundary corrosion.

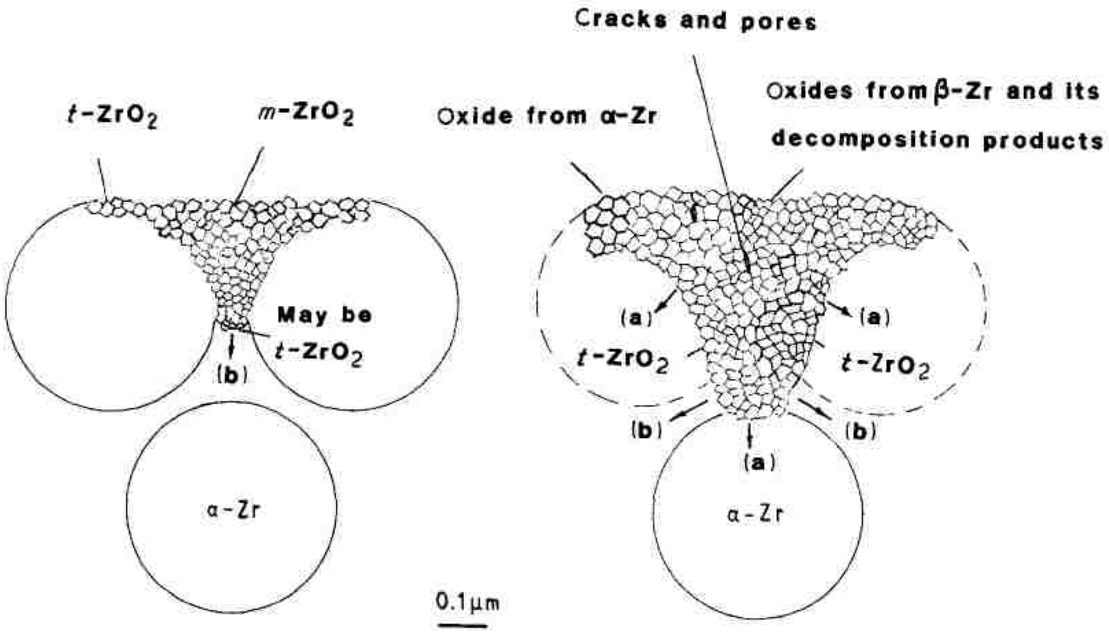

Fig. 2.10 Schematic illustration of the process occurring during the oxidation of Zr-2.5Nb in an aqueous environment. (a) corrosion on α–Zr; (b) boundary corrosion [45].

Cox [36] is also of the same opinion that the failure of the zirconium oxide film may be due to phase transformations. He thought that the cracking of zirconium oxide may be the result of a tetragonal or cubic to a monoclinic form of the oxide, this involving a volume change. The centers of this transformation may be inclusions in the metal, including particles which have been converted to hydrides.

Numerous X-ray investigations have shown that in the first stages of oxidation only, it is sometimes possible to identify an oxide with a cubic or tetragonal structure. During the pre-transition period of oxidation, mainly monoclinic ZrO_2 is formed. Direct investigation of samples has not shown any distinct dependence of the time to transition on the phase transformations taking place in the oxide film.

Beie et al. [44] studied the long-time corrosion test using Zircaloy samples. In the first step of corrosion, substoichiometic ZrO_2 was formed. This oxide (which may remain amorphous for a certain time) crystallized to small equiaxed tetragonal grains. When the size of these grains reaches some critical value, they transform to the monoclinic modification. Some amount of t- ZrO_2 will survive since it is stabilized for its small crystallite size by high compressive stress at the metal-oxide interface, or by dissolved alloying elements, or both. It was also mentioned that a high hydrogen concentration at the metal-oxide interface facilitates the transformation from the tetragonal to monoclinic phase. The further oxide formation at the metal-oxide interface leads to a preferential growth of the monoclinic crystals. If the corrosion is uniform, this process leads to a dense layer with a columnar structure consisting mainly of monoclinic zirconium dioxide. But in nodular oxides, equiaxed grains are formed at the metal-oxide interface and no, or probably only a thin compact layer, exists.

2.5.3 Properties of the oxide film

Zirconium dioxide is an insulator with a large bandgap at 5eV. This oxide has potential applications in various fields such as protective coatings, dielectric compounds in metal oxide semiconductor devices and as a high temperature O^{2-} conducting electrolyte. It is also important in sensors and fuel cell applications. Thick oxide films can be obtained by sputtering, pulsed laser deposition, chemical vapor deposition and atomic layer epitaxy and also by wet methods such as anodization [50, 51].

Analysis of the oxide film has shown that its chemical composition may differ from the stoichiometric properties. The black protective oxide film shows an oxygen deficiency, while the white friable oxide film has a chemical composition corresponding exactly to the formula ZrO_2. Bibb and Faschia. [52], who have investigated the deformation of the crystal lattice of the oxide film by considering the width of the deformation peaks at their halfheight, have found that in all cases the crystal lattice of the black oxide is more distorted than that of the white oxide. It is therefore assumed that the transition from the black oxide to the white, and, correspondingly, the breakaway point on the oxidation curve, are connected with the recrystallization of the oxide. Recrystallization and failure will occur if the stresses in the oxide film reach a high value, as a result of film growth, the presence of inclusions, grain boundaries, or other factors. This may also be brought about if the distorted oxide film is heated for a sufficiently long time at a high temperature.

2.6 Methodology for evaluation of of Zr-2.5Nb tubes and deuterium uptake

Many mechanistic, semi-empirical and empirical models for Zircaloy corrosion have been presented and critically compared in previous publications. There are few published models in the open literature on Zr-2.5 Nb corrosion [13, 53].

Fitness-for-service guidelines have been developed to provide a systematic procedure for the evaluation of pressure tubes. The rationale is that a low probability of pressure tube rupture must be assured. Procedures have been developed to determine whether tubes containing detected or postulated flaws are susceptible to crack initiation. As defence in depth, tubes with detected flaws that are not susceptible to crack initiation must also satisfy a leak-before-break (LBB) criterion [14].

For the evaluation of generic changes in fracture properties a flaw is postulated that corresponds to the smallest part-through crack just prior to through-wall penetration. This flaw is examined for the possibility of unstable propagation based on the material fracture properties and hydrogen plus deuterium concentration prevailing at the time. When hydrides and deuterides are present at nominal operating, ful-power conditions, the postulated flaw is also examined to determine whether it has adequate resistance to DHC.

To assure LBB in pressure tubes, the crack length when the leaking crack is detected must be less than the critical crack length (CCL) for unstable propagation and the reactor must be shut down before the crack length exceeds the CCL. The response time t, assuming that double-ended crack growth is one of the scenarios, is given by

$$\mathrm{t} = \frac{CCL - leakCL}{2 \times DHCV} \tag{2.6}$$

Where ‘leak CL’ is the crack length at first detected wall penetration and DHCV is the axial DHC velocity of the leaking crack. To demonstrate LBB, the postulated length of a through-wall flaw growing by DHC must be less than the CCL during the entire postulated sdquence of events from first wall penetration to safe shutdown. The assessment is performed by assuming a length for crack at breakthrough and detection and specifying the subsequent reactor shutdown sequence employed. This means taking account of the variation in DHC velocity and CCL as the coolant temperature and pressure in the tubes are reduced. It is evient that to assure LBB up to the design life of the pressure tube, the changes with time of the parameters in Eq. (2.6) need to be known.

Based on Cox's [35] model, the zirconium oxide layer is treated as a bilayer with an inner protective barrier and an outer porous nonprotective layer. It is assumed that the rate of corrosion depends solely on transport across the dense barrier layer. The point defect model of oxide film growth of Macdonald [54] has been used to describe this phenomenon. The transformation of the barrier layer into a nonprotective porous layer at the outer side of the barrier layer ultimately controls the reaction, because the thickness of the barrier layer is dependent on this transformation. Similar work has been reported by Macdonald on oxide films in which the steady-state growth and dissolution of the barrier layer was studied. Work done by Pensado-Rodriguez et al. [55] on Li oxides in alkaline solutions has clearly shown that at steady state, the cathodic reaction in the system, i.e. hydrogen evolution, is proportional to the porosity of the outer layer and that porosity is needed to maintain water transport to allow the cathodic process to occur. In Zr-2.5 Nb, the exact mechanism for the transformation of a dense barrier layer to a nonprotective porous layer is not understood but is critical to the entire corrosion reaction.

In this thesis, we assume that this transformation occurs as a result of chemical dissolution of the zirconium oxide. Zirconia will dissolve chemically to form zirconate if the pH is high enough.

The oxides at the oxide-metal interface formed in an aqueous environment are mainly extended along grain boundaries, and are characterized by long to short-circuit diffusion at the grain boundaries which is caused by the nature of the crystallite boundaries of the oxide, the flaws arising from the oxidation of the grain boundary phases (β-Zr, its decomposition products as well as impurities), and cracking of the oxide due to phase transformations in ZrO_2.

2.7 The effects of Lithium on the corrosion behavior of zirconium alloys

LiOH is added to the primary coolant of most PWR's to maintain an alkaline pH so as to control the transport of corrosion products from the structural materials of the reactor coolant system. Bulk concentrations of lithium in the coolant typically range from 0.2 to 2 ppm (3×10^{-5} to 3×10^{-4} molal LiOH). Lithium can adversely affect the corrosion of zirconium alloys and, in this regard, corrosion of Zr-2.5Nb is more sensitive than the Zircaloys to Li^+ ion content. The evidence for this so called "lithium effect" is from laboratory tests. With increase in lithium hydroxide concentration, >50 to 100 ppm Li, the corrosion rate is seen to increase.

Several hypotheses have been proposed to account for this phenomena: (1) An increase in anion vacancies in the oxide caused by the substitution of zirconium by lithium in the zirconia lattice [56]; (2) The generation of pores caused by preferential dissolution of t-ZrO_2 in zirconia films exposed in more than 0.1M LiOH aqueous solution [57]; (3) A modified crystal growth mechanism induced by the formation of surface OLi groups, which impedes the diametrical and columnar growth of the oxide crystallites [58].

A lot of research has been carried out on the crystallization and degradation of zirconium oxide in different pH alkaline solutions, most of which were done in lithium hydroxide solutions [59, 60]. Zirconium alloys generally show an accelerated corrosion rate in LiOH solutions, and the rate increased dramatically with increasing concentration of LiOH (pH value) and increase in temperature. When tested in very high pH solutions (>13.5), there would no longer be a pre-transition period and the thickness of oxide increased rapidly [56]. It is interesting to note that this accelerated corrosion rate of zirconium alloys always occurs in LiOH solutions, not in other metal hydroxide solutions such as KOH, NaOH and NH_4OH at the same molar content or in 1M lithium salt solutions such as $LiNO_3$, Li_2SO_4 and Li_2CO_3. In a KOH solution of pH 14, however, some acceleration of corrosion occurs. This suggests that not only the cations but the concentration of OH- ion, that is, pH, may govern the corrosion of zirconium alloys at the same time [61]. Thus far, it is not clearly understood why the corrosion of zirconium alloys depends on pH and higher accelerated corrosion occurs in LiOH solutions.

Garzarolli et al. [62] proposed that the amorphous oxide formed at the oxide/metal interface initially crystallizes to fine equiaxed tetragonal zirconia, which grows and transforms at a certain critical size to monoclinic grains. Further, the oxide film of columnar monoclinic zirconia and fine tetragonal zirconia was also observed in post-transition oxides in water. However, a TEM study showed the presence of only equiaxed monoclinic ZrO_2 grains without any tetragonal zirconia even near the oxide/metal interface in the post-transition with accelerated corrosion by LiOH [44]. These facts suggest that the crystallization behavior of zirconia grains may depend on the pH of the solution, leading the oxide film to have different structures at different pHs.

Once the tetragonal oxide crystallizes on zirconium alloys, it transforms into monoclinic zirconia, thus degrading the intact oxide. Since this tetragonal to monoclinic (t→m) transformation rate is a major controlling factor in the corrosion resistance of zirconium alloys, it is necessary to elucidate the causes for the t-m transformation of zirconia. Even though the cause for the t-m transformation is suggested to be related to stress relaxation, it is still not understood what triggers the stress relaxation. Garzarolli et al. [62] suggested that the t-m transformation of zirconia may be enhanced by the presence of hydrogen. However, it is to be noted that the tetragonal zirconia stabilized by 3 mol% Y_2O_3 is degraded at low temperature, which is enhanced in humid conditions such as water or steam rather than in air. These facts seem to indicate that OH^- ions in aqueous solution rather than hydrogen ions trigger t-m transformation even though their role in the t-m transformation needs a better understanding. If we assume that a similar degradation phenomenon occurs in the zirconia film on zirconium alloys, then the corrosion of zirconium alloys can be understood by correlating the degradation behavior of tetragonal zirconia in various solutions containing alkali metal hydroxides or salts.

Furthermore, enhanced corrosion of zirconium alloys in LiOH solutions may be attributed to the enhanced t-m transformation rate.

Oxides grown in concentrated solutions are fine grained and show a higher concentration of lithium when compared to those grown in dilute solutions [59, 60]. These observations when considered with the acidic nature of zirconium oxide indicate that lithium exists as a surface species on the oxide crystallite.

Beie et al. [44] using TEM metallography showed that a lithium-containing environment attacks the oxide grain boundaries and supports the hypothesis proposed by Cox et al. [63, 64] that LiOH causes a preferential dissolution of ZrO_2 at the grain boundaries. In addition, the dense oxide layer without a porous network at the metal-oxide interface is thinner in oxide scales formed in an environment containing LiOH compared to that formed without LiOH. This explains why the corrosion rate is increased under the influence of LiOH.

2.8 Wear concerns in the reactor core

As shown in Fig. 2.2, the fuel for CANDU nuclear power reactors is in the form of bundles of tubes containing pellets of uranium oxide. The bundles are loaded into a reactor by hand in its initial startup. Once the reactor is operating, bundles are loaded automatically by a fuelling machine. This is a unique aspect of the CANDU design: the reactor can be refueled while in operation. Fig. 2.11 shows the refueling process schematically.

The fuelling machine locks on to a pressure tube and inserts a new fuel bundle while a similar machine locks on to the other end of the same pressure tube to receive a spent bundle. Thus a CANDU is constantly being “topped up” with fuel, whereas the more widely-used light water reactors must be shut down in order to replace all of the fuel. For a CANDU 6 reactor, about 10 fuel channels per week are refueled. During the refueling process, wear takes place between the inner surface of pressure tubes and the Zircaloy bearing pads that are distributed on the outer ring of fuel elements which support the bundle within the pressure tube. The black oxide coating is relatively thin (about 1-2μm) and could be removed by the scratching action of the bearing pads, potentially leading to aggravated corrosion and hydrogen ingress.

At the reactor core in operating power plants, there is another type of wear called fretting damage, which has been reported between a nuclear fuel rod and its supporting pad of the fuel assemblies. This is due to a flow-introduced vibration, which results from the primary coolant that rapidly passes around the fuel rod to remove the excess heat generated by the nuclear reaction [65].

The pressure tube acts as the first barrier to the radiation source and the problem of diametric expansion and elongation due to irradiation deformation always take place which may limit the useful life of pressure tubes. Those geometric distortions can increase the wear problems, both friction wear and fretting wear [65].

The advantage of zirconium and its alloys over other structural materials consists of the combination of low density with high corrosion resistance in numerous corrosive media. However, the use of such alloys is often limited due to their low wear resistance, thus requiring the application of coatings of high hardness.

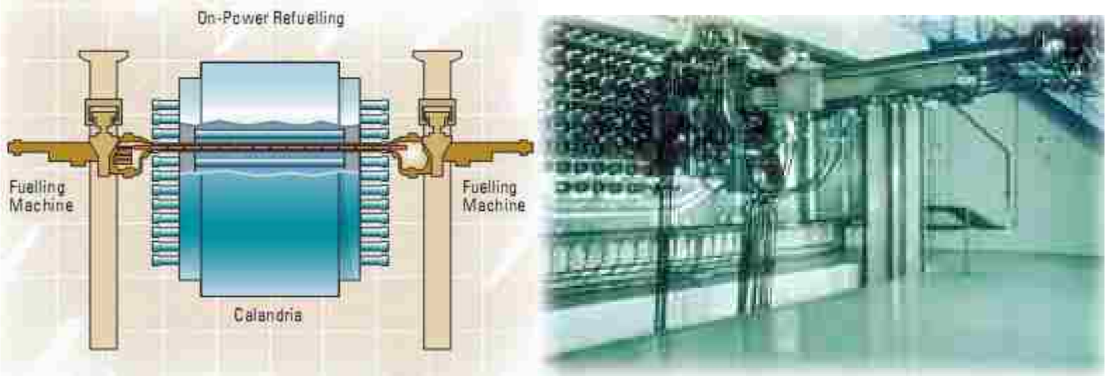

Fig. 2.11 Refueling on power [12].

2.9 Technical problems to be addressed

Zr-2.5Nb has good corrosion resistance properties in both aqueous or steam conditions. The “naturally grown” black oxide coating on its surface greatly enhanced the resistance to further oxidation and hydriding. However, the adhesion wear properties of this thin black oxide coating may not be satisfactory when the fuel bundles move along the pressure tubes during the refueling process. Any scratches on the tube inner surface may cause localized corrosion and thus accelerate the ingression of hydrogen and oxygen. If there is one area on the tube wall penetrated, the whole pressure tube is unserviceable.

To combat any potential corrosion and wear problems, a relatively new technique Plasma electrolytic oxidation (PEO), was used in this research study to provide the base material, Zr-2.5Nb, with better corrosion and wear resistance properties.

2.10 Development of PEO technique

Micro-arc oxidation (MAO) is a plasma-chemical and electrochemical process. The process combines electrochemical oxidation with a high voltage spark treatment in an alkaline electrolyte, resulting in the formation of a physically protective oxide film on the metal surface to enhance wear and corrosion resistance as well as prolonging component lifetime. It is especially suitable for the surface oxidation and pigmentation of aluminum, titanium, niobium, zirconium, magnesium and their alloys. The treated components are used in the building, mechanical, transportation and energy sectors. The technology is simple and energy saving and offers high throughput, low cost, high film quality, wide range of color pigmentation as well as environmental friendliness.

During the 1970s, Markov and Markova and their coworkers, developed an advanced anodizing technique on an aluminum anode [66, 67]. The wear resistance properties of the coatings on light metals were also investigated. Later this technique was improved and termed 'micro-arc oxidation'. In the 1980s, the possibilities of utilizing surface discharges in oxide deposition onto various metals were studied in more detail in Russia by Snezhko [68-73], Markov [74-76], Fyedorov [77], Gordienko [78-80] and their coworkers. At the same time in Germany, early industrial applications of MAO process were introduced. Researchers in the USA, UK and China have also contributed to the research in this field. Because of the insufficient information on the process phenomenology and mechanisms, different terminologies have been used for MAO in most of the above studies: ‘micro-plasma oxidation’, ‘anode spark electrolysis’, ‘plasma electrolytic anode treatment’, and ‘Anodischen Oxidation under Funkenentladung’ (anode oxidation under spark discharge), being typical examples of descriptions common to ‘Plasma Electrolytic Oxidation’ (PEO). In this thesis, the term PEO is used to describe the process.

2.11 PEO equipment

Plasma electrolytic oxidation (PEO) or micro-arc oxidation (MAO) evolved from the conventional anodizing process. Thus, the processing equipment for PEO is relatively similar to that for the anodizing process except for the need of a much higher voltage power source. Fig. 2.12 shows the typical treatment unit for PEO process [3]. The treatment unit consists of an electrolyser (Fig. 2.12(b)) and a high power electrical source. The electrolyser is usually a water-cooler bath placed on a dielectric base and confined in a grounded steel frame, which has an insulated current supply and a window to observe the process in operation. A stainless steel plate is immersed in the base which serves as the counter-electrode. In some cases, the electrolyser incorporates electrolyte mixing, recycling, and gas exhausting arrangements, as well as some safety interlocks.

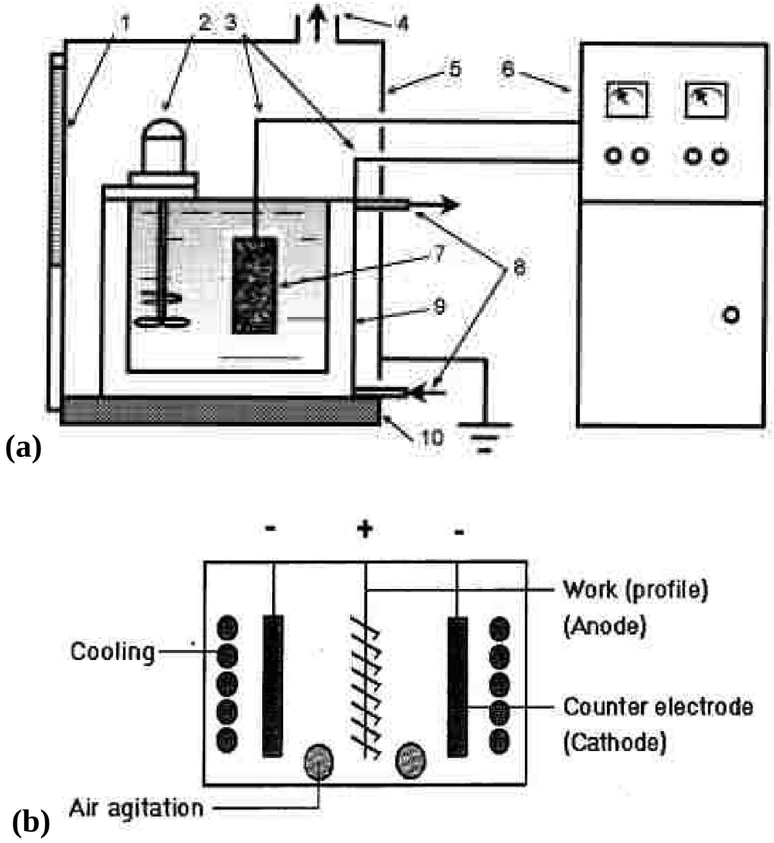

Fig. 2.12 (a) Typical treatment unit for PEO process (1. window, 2. mixer, 3. connecting wires, 4. exhaust/ventilation system, 5. grounded case, 6. power supply unit, 7. work piece, 8. cooling system, 9. bath, 10. insulating plant) and (b) Electrolyte bath [3].

Different types of power source can be used for the PEO process. Depending on the applied electrical regime, these are: DC sources, pulsed DC sources, unbalanced AC sources and heteropolar pulsed current sources. Due to the difficulties in regulating the surface discharge characteristics, a DC source is only used for simple-shape components and thin coatings. Based on the needs of the nuclear industry applications, thick coatings are detrimental for they will decrease the effective wall thickness of pressure tubes and shorten the service life. A DC power source was utilized in this study to produce thinner films.

2.12 Coating procedure

All samples are polished, cleaned and degreased before the PEO process. After this pretreatment, the sample is connected to the anode of the power source unit and immersed into the bath. The cathode of the power source unit is attached to the stainless steel counter-electrode. The PEO treatment is typically carried out for 0.85, 2 and 4min at current densities of 0.05, 0.1, 0.25Acm^{-2} and voltages of up to 400V.

2.13 Phenomena during the PEO process

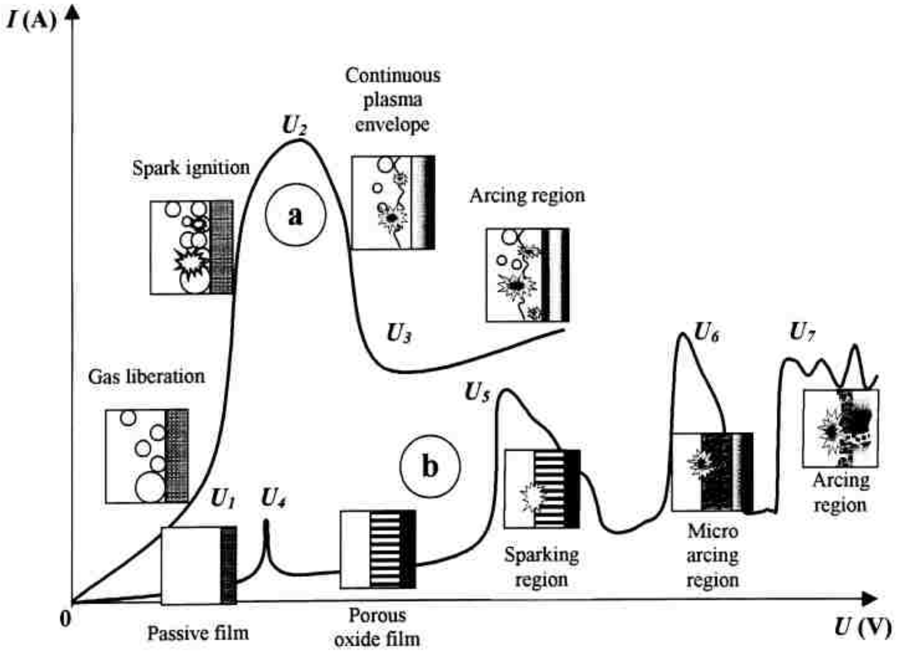

Fig. 2.13 Two types of current-voltage diagram for the processes of plasma electrolysis: discharge phenomena phenomena are developed (a) in the near-electrode area and (b) in the dielectric film on the electrode surface [3].

Yerokhin et al. [3] made an intensive study of plasma electrolysis for surface treatment and described the current-voltage characteristics during the PEO process—refer to Fig. 2.13. A 'type-a' current-voltage plot represents a metal/electrolyte system with underlying gas liberation on either the anode or cathode surface and 'type-b' represents the formation of an oxide film. In the region '0-U1' in the type-a system and '0-U4' in the type-b system, the increase of voltage leads to a proportional increase of current, which conforms to Ohm's law. However, beyond the critical voltage (U1 and U4), the behavior of current-voltage changes greatly.

For a type-a system, a potential rise in the region U_1-U_2 causes current oscillation, together with luminescence. The current rise is limited by a partial shielding action of gaseous reaction products (O_2 and H_2) on the electrode surface. With increasing current density, local boiling takes place in some areas of electrolyte/metal interface. When the voltage exceeds the second critical value U2, the electrode is completely covered by a continuous gaseous vapor envelope of low electrical conductivity. The electric field strength E within this region reaches a value between 10^6 and 10^8 V/m, which is sufficient to initiate the ionization processes in the vapor envelope. The ionization phenomena starts as a rapid sparking in scattered gaseous bubbles and then transform into a uniform low distributed throughout the vapor plasma envelope until the voltage reaches the value of U_3. After that, the glow discharge transforms into intensive arcing accompanied by a characteristic low-frequency acoustic emission.

The other system, type-b, is more complicated. At the beginning of the process, the passive film, which formed previously, begins to dissolve at point U_4 (corrosion potential of the material). Then a porous oxide film grows in the repassivation region of U_4-U_5 and the voltage drops greatly. At point of U_5, the electric field strength in the oxide film reaches a critical value beyond which the film fails due to impact or tunneling ionization. In this case, small luminescent sparks move rapidly across the oxide surface, which is favorable for its continued growth. At point U_6, the mechanism of impact ionization is supported by the start of thermal ionization and slower, larger arc-discharge arises. In the region U_6~U_7, thermal ionization is partially blocked by negative charge build-up in the bulk of the thickening oxide film, resulting in discharge-decay shorting of the substrate. Above the point U_7, the arc micro-discharges occurring throughout the film penetrate through to the substrate and (since negative charge blocking effects can no longer occur) transform into powerful arcs, which may cause destructive effects such as thermal cracking of the film.

2.14 General principles of PEO

The PEO process involves anode electro-chemical dissolution, the combination of metal ions with anions to form complex ceramic compounds, and sintering on the substrate under the action of discharges. Yerokhin et al. [81] described the PEO principles by giving a model of the process to describe the physic-chemical processes in the discharge channels This model is based on the general theory of the breakdown of a metal/dielectric/liquid system in a strong electric field.

Three main steps can be discerned in the breakdown process. In the first step, the discharge channel is formed in the oxide layer as a result of the loss of its dielectric stability in a region of elevated conductivity. This region is heated by generated electron avalanches up to temperatures of ~10^4 K. Due to the strong electric field (of the order of ~ 106Vm^{-1}), the anionic components of the electrolyte are drawn into the channel. Concurrently, owing to the high temperature, bulk material and alloying elements are melted out of the substrate and enter the channel. Thus, a plasma column (plasmoid) is formed as a result of these processes. In the second step, plasma chemical reactions take place in the channel. These lead to an increase in pressure inside the channel, so the plasmoid expands to balance it. Meanwhile, separation of oppositely charged ions occurs in the channel due to the presence of the electric field. The cations are ejected from the channel into the electrolyte by electrostatic forces. In the last step, the discharge channel is cooled and the reaction products are deposited on to its walls. The above process repeats itself at a number of discrete locations over the coating surface thus leading to an overall increase of the coating thickness. This PEO technology has been used, first of all, for the surface hardening and enhancement of the corrosion resistance of aluminum and, recently, magnesium and titanium alloys. The coatings produced in such a way, possess high hardness and wear resistance and adhere well with the matrix irrespective of their thickness. They can be used as both corrosion-resistant and dielectric materials. The advantage of zirconium alloys over other structural materials consists of the combination of low density with high corrosion resistance in numerous corrosive media. However, the use of such alloys in nuclear industry is limited due to their low wear resistance, which requires applying coatings of high hardness on them while not degrading the corrosion resistance. However, until recently, little information has been available on the PEO treatment of zirconium and its alloys [9, 10].

2.15 PEO coatings fabricated on zirconium alloys

Recently, the utilization of PEO technique in the improvement of the mechanical and corrosion properties of zirconium alloys has attracted more and more attention. Pauporte et al. [51] prepared a 3.2 μm thick coating on Zr by plasma electrolysis. Zhou et al. [82], Matykina et al. [10] and W. Xue et al. [9] used an AC power source to produce coatings on zirconium alloys in an Na_2SiO_3 electrolyte. Zhang et al. [83] fabricated PEO coatings on Zircaloy-4 using a DC supply in a NaOH electrolyte. According to these researchers, the functional properties of the coatings depend on the synthesis conditions, including the electrolyte composition, the cathode and anode current densities, and also the treatment time. The enhancement of corrosion and wear properties were key points of some of these investigations. Table 2.3 summarizes some of the research work on the PEO technique on zirconium alloys in recent years.

Table 2.3 Studies of PEO technique on zirconium alloys.

Researcher [Reference]	Zirconium alloy	PEO condition		Thickness of coating	
		electrolyte	power		
Pauporte et al. [51]	99.8% zirconium	0.1M $(NH_4)_2B_4O_7$	AC	3.2μm	
Zhou et al. [82]	Zircaloy-4	Na_2SiO_3	AC	28μm	
Matykina et al. [10]	Zirlo™	Na_2SiO_3 +KOH	AC 10A dm^{-2} 50Hz	42±5μm	
W. Xue et al. [9]	Zr-2.5Nb	Na_2SiO_3 +KOH	AC +540V -200V	10min	25μm
				25min	70μm
				90min	240μm
Zhang et al. [83]	Zircaloy-4	NaOH	DC	60μm	
Klapkiv et al. [84]	Zr-2.5Nb	Na_2SiO_3 +KOH	anodic-cathodic mode	100-120μm	

Klapkiv et al. [84] examined the prospects of creating 30-40μm thick oxide-ceramic coatings on Zr-2.5Nb based on studying specific features of the formation of electrolytic plasma and relationships between the plasma parameters and treatment conditions with the properties of the PEO coating. By means of spectrum analysis, the temperature of plasma was calculated to be 6×10^3~10^4 K during the traditional PEO process. At such temperatures, the electrolyte components dissociate and are ionized, obtaining a high chemical reactivity and providing a higher rate of the reaction of oxide formation as compared with the classical electro-chemical methods.

Furthermore, there appear high-temperature oxide phases possessing higher functional parameters (e.g., chemical durability, density, etc.)

2.16 PEO coating structure on Zirconium alloys

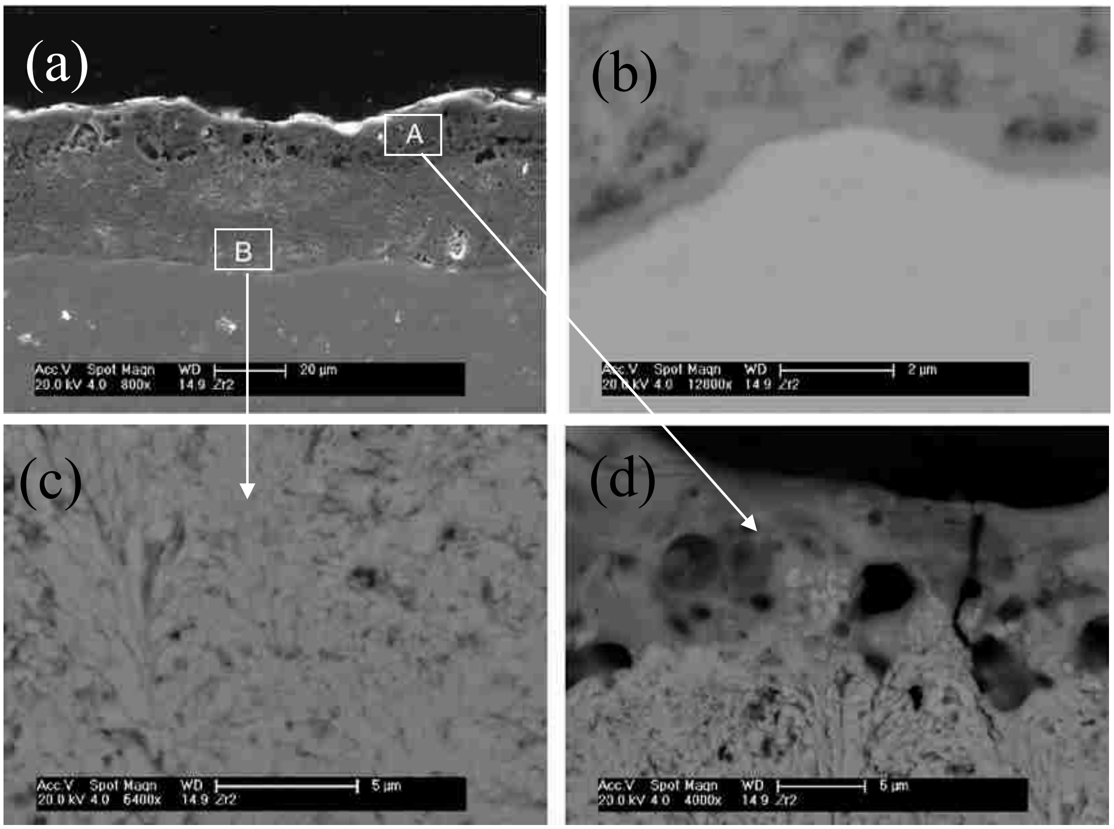

Fig. 2.14 SEM of the coating formed on Zirlo for 1800s at 10Adm-2. (a) secondary electron image of the cross-section; (b) backscattered electron image of the barrier layer region and (c, d) backscattered electron image at increased magnification of the intermediate and outer layers respectively [10].

Fig. 2.14 illustrates the typical microstructure of PEO coated sample on a zirconium alloy produced using an AC power source [10]. The SEM micrograhs show a three-layered coating formed after 30 minutes PEO treatment. The cross-section shows an area where ‘soft’ sparking had been established. The ~42±5μm-thick coating comprises a ~400 to ~500 nm thick barrier layer, an intermediate layer, with fine porosity, and an outer~12μm-thick layer with relatively coarse porosity. PEO coatings adhere well to the substrate for the irregular alloy/coating interface. Some large closed pores can be observed inside the coating area.

Based on XRD analysis, the coating is monoclinic ZrO_2 (m- ZrO_2) and tetragonal ZrO_2 (t- ZrO_2) phases, but the t- ZrO_2 content is much lower than the m- ZrO_2. Pauporte et al. [51] reported that the occurrence of the electrical discharge is accompanied by the crystallization of the PEO coating on zirconium and the temperature in the spark channel is very high leading to the formation of a plasma phase, but it is not high enough to stabilize the tetragonal phase (transition at ca. 1100° C). In fact, the temperature in the spark discharge zone can reach 8000° C, and the instantaneously local melting and following rapid solidification will take place around the discharge channel.

A previous paper [85] proposed a formation mechanism of α-Al_2O_3 and γ- Al_2O_3 phases in PEO coatings on an aluminum alloy: both the α-Al_2O_3 and the γ- Al_2O_3 phases mainly result from the rapid solidification of the melt at the discharge channel, and the change of cooling rate of the melt at the different depths of the coating results in the differences in α-Al_2O_3 and γ- Al_2O_3 contents in the outer and inner layer coatings. The formation of different zirconium oxides may be also explained by a similar mechanism of rapid solidification, followed by phase transformation of melt in the discharge zone. Zirconium dioxide has three equilibrium phases in different temperature ranges: cubic

ZrO_2 (c- ZrO_2), tetragonal ZrO_2 (t- ZrO_2) and monoclinic ZrO_2 (m- ZrO_2) phases. The m-ZrO_2 transforms into t- ZrO_2 phase by heating above 1170°C, then t- ZrO_2 transforms into c- ZrO_2 by heating above 2300°C. When one discharge spark quenches in the solution, the melt in the discharge zone rapidly solidifies to form c- ZrO_2 phase. When the temperature of c- ZrO_2 decreases below 2300°C, c- ZrO_2 transforms into t- ZrO_2 by solid phase transformation, and then the t-ZrO_2 continues transforming into m- ZrO_2 phase below 1170°C until the electrolyte temperature cools back down to room temperature. Thus, the m-ZrO_2 will be a main phase in PEO coating on zirconium alloys. On the other hand, the cooling rate on the coating surface contacted with aqueous solution is higher than that in the interior of coating. Therefore, some residual t-ZrO_2 phase remains in the coating during t-ZrO_2→m-ZrO_2 phase transformation, but the residual t-ZrO_2 phase in the outer layer coating is more than that in the interior of coating due to the difference of cooling rate at the different depths of the coating.

According to Ding and Northwood [45], the compressive stresses can only exist over a small distance from the oxide/metal interface. Once the compressive stresses has decreased below the critical value, t- ZrO_2 should transform to m- ZrO_2 if there are no other factors, such as small grain size or chemical stabilizers, which could also help retain the tetragonal structure. Such t- ZrO_2→m- ZrO_2 phase transformation can result in microcracking, which may increase the oxygen and hydrogen diffusion into the metal.

Internal stresses in PEO coatings are caused by: (a) formation and growth of oxide film on the metal surface, (b) thermal effects from surface microdischarges and (c) phase transformations in the oxide film. Stress caused by the formation and growth of oxide film (i.e., intrinsic stress) arises because the oxide usually has a larger volume than that of the metal from which it is formed. If the oxide maintains crystallographic coherency with the underlying metal, then the oxide is in compression, while the metal is placed in tension. It is generally recognized that compressive stresses in coatings are more favourable than tensile stresses, because they increase resistance to fatigue failure. However, extremely high compressive stresses may cause coating separation from the base metal, intra-coating spallation or formation of cracks in the coatings.

Xue et al. [9] also measured the nano-hardness by a nanoidentation test from the cross-section of PEO-coated Zr-2.5Nb alloy. The nanohardness (H) and elastic modulus (E) of the thick PEO ceramic coating on Zr-2.5Nb under the 50mN load is shown in Fig. 2.15. The zero point on x axis corresponds to the alloy/coating interface, where one array of triangle indentations are vertical to this interface.

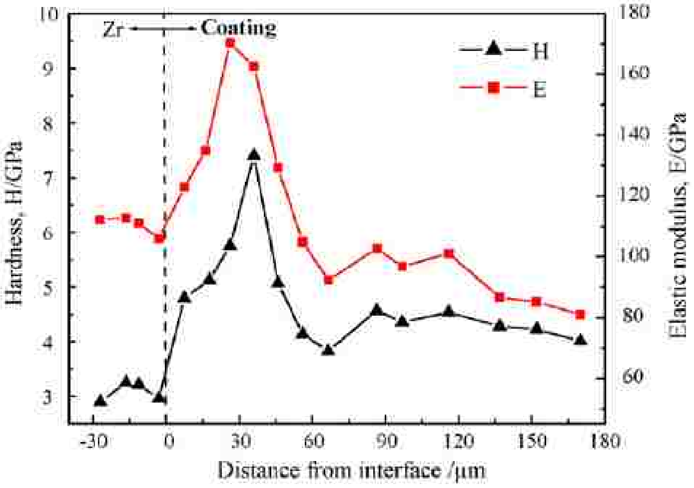

Fig. 2.15 Profiles of nanohardness (H) and elastic modulus (E) across the 240μm PEO coating on Zr-2.5Nb alloy.

From Fig. 2.15, it could be seen that the hardness and elastic modulus of PEO coating are much higher than the substrate over a certain thickness range. That is different from the results of nano-indentation test for PEO on an Al alloy [86], in which the H and E of PEO coating are always higher than the Al alloy substrate. The authors explained that it might result from the heterogeneous distribution of the m- and t- phase ZrO_2 in the PEO coatings, together with the existence of amorphous SiO_2 phase in the outer layer coating. However, there is no supporting experimentation to confirm the above interpretation.

2.17 Summary of the literature review

Over time, pressure-containing components used in nuclear reactors are subject to degradation due to exposure to high stresses, temperature and neutron flux. To ensure a safer and longer service time, greater requirements were asked to the core components which are made by zirconium alloys. Zr-2.5Nb, the material of pressure tube, has a satisfactory corrosion resistance when exposed to steam and high temperature water. However, the corrosion rate accelerated greatly in the high temperature and Li+ added aqueous conditions. On-power refueling in CANDU requires a relatively high wear resistance of any protective coating. The Plasma Electrolytic Oxidation (PEO) technique can make oxide-ceramic coatings on metals such as Al, Mg and Ti for surface hardening and enhancement of the corrosion and wear resistance. This process consists of plasma generation in spark discharge channels on the electrode of a metal-electrolyte system under the action of external electric field, chemical reactions between the metal and plasma components, and deposition of the reaction products on the electrode. The coatings produced in such a way possess high hardness and wear resistance and adhere well with the matrix irrespective of their thickness.

Four different stages of PEO process have been identified, characterized by various formation mechanisms:

(i) anodizing,
(ii) anodizing film melted and broken down,
(iii) micro-arc discharge and oxide coating formation, and
(iv) coating composition fused and re-crystallized.

The PEO coating made on zirconium alloys has a three layer structure: porous outer layer, dense medium layer and several-hundred-thick inner dense layer. The dense medium layer has the highest thickness and hardness/Young’s modulus compared to the other two layers.

The metal/oxide interface of PEO coating shows an undulation and the coatings are uneven in thickness. This may enhance the adhesion of the coatings. However, whether or not the PEO coatings have an advantage over the commercially used black oxide coating in wear and corrosion resistance properties in both ambient and high temperature/pressure conditions was a question that was left unanswered before the present work was conducted.

Chapter 3: EXPERIMENTAL PROCEDURES

In this chapter, the experimental procedures used for the deposition of the PEO coatings on Zr-2.5Nb substrate, and the investigation of their corrosion and wear resistant properties, are described. Potentiodynamic polarization measurements were utilized to determine the corrosion resistance of different types of coatings at room temperature. High temperature and pressure corrosion tests were carried out using a sealed stainless steel autoclave in the LiOH solution for up to 30 days. Pin-on-disc wear tests were conducted to evaluate the wear resistance of the coatings under dry or lubricated conditions. The roughness of the coatings and the mass loss after the wear test was measured by a surface profilometer. Scanning electron microscopy (SEM) with energy dispersive X-ray analysis (EDX) and X-ray diffraction (XRD) were employed to characterize the morphologies, chemical and phase composition of the coatings before and after testing.

3.1 Materials and chemicals

3.1.1 Substrate

In this study, the substrate material is commercial Zr-2.5wt%Nb alloy pressure tubing supplied by Ontario Hydro. The chemical analysis is given in Table 3.1 [40].

Table 3.1 Chemical analysis of Zr-2.5 wt.% Nb alloy [40].

<table>
<tr><th colspan="36">Weight percent</th></tr>
<tr><td colspan="12">Nb</td><td colspan="12">Fe</td><td colspan="12">O</td></tr>
<tr><td colspan="12">2.50</td><td colspan="12">0.055</td><td colspan="12">0.110</td></tr>
<tr><td colspan="36">Impurity analysis (ppm by weight)</td></tr>
<tr><td colspan="4">Al</td><td colspan="4">B</td><td colspan="4">C</td><td colspan="4">Cd</td><td colspan="4">Cr</td><td colspan="4">Co</td><td colspan="4">Cu</td><td colspan="4">H</td><td colspan="4">Hf</td></tr>
<tr><td colspan="4">35</td><td colspan="4"><0.2</td><td colspan="4">120</td><td colspan="4"><0.2</td><td colspan="4">74</td><td colspan="4"><10</td><td colspan="4">30</td><td colspan="4">10</td><td colspan="4">44</td></tr>
<tr><td colspan="36">Impurity analysis (ppm by weight)</td></tr>
<tr><td colspan="4">Mg</td><td colspan="4">Mn</td><td colspan="4">Mo</td><td colspan="4">N</td><td colspan="4">Ni</td><td colspan="4">Pb</td><td colspan="4">Si</td><td colspan="4">Sn</td><td colspan="4">Ta</td></tr>
<tr><td colspan="4"><10</td><td colspan="4"><25</td><td colspan="4"><25</td><td colspan="4">50</td><td colspan="4"><35</td><td colspan="4"><50</td><td colspan="4">59</td><td colspan="4">15</td><td colspan="4"><200</td></tr>
<tr><td colspan="36">Impurity analysis (ppm by weight)</td></tr>
<tr><td colspan="9">Ti</td><td colspan="9">U</td><td colspan="9">V</td><td colspan="9">W</td></tr>
<tr><td colspan="9"><50</td><td colspan="9"><0.5</td><td colspan="9"><25</td><td colspan="9">25</td></tr>
</table>

3.1.2 Chemicals

Table 3.2 shows the chemicals used for the electrolytes, corrosive solution used in potentiodynamic polarization test and autoclave test, polishing slurries, cleaning and etchant.

Table 3.2 Chemicals used in this study

Purpose	Name	Molecular formula	Purity or size	supplier
PEO Electrolytes	Sodium Metasilicate	$Na_2SiO_3 \cdot 5H_2O$	SiO_2 44-47%	Sigma-Aldrich Inc. USA
	Potassium hydroxide	KOH	Assay min. 85%	ACP Chemical Inc. Canada
Corrosion testing solution	Lithium hydroxide monohydrate	$LiOH \cdot H_2O$	Reagent grade ≥98%, powder	Sigma-Aldrich Inc. USA
Sample preparation	Gamma Alumina	Al_2O_3	5.0 micron	Buehler, USA
	Gamma Alumina	Al_2O_3	1.0 micron	Buehler, USA
	Ethanol	C_2H_5O	Assay min. 95%	Sigma-Aldrich Inc. USA
	Etchant		45vol%HNO_3: 45vol%H_2O: 10vol% HF	Sigma-Aldrich Inc. USA

3.2 Specimen preparation

Rectangular coupons with dimensions of 15×13×4mm were cut from commercial Zr-2.5Nb pressure tube with the black oxide coating on both surfaces. Fig. 3.1 illustrates the sectioning of the pressure tube: the three axial coordinates are A: Axial direction, R: Radial direction, T: Tangential direction.

.

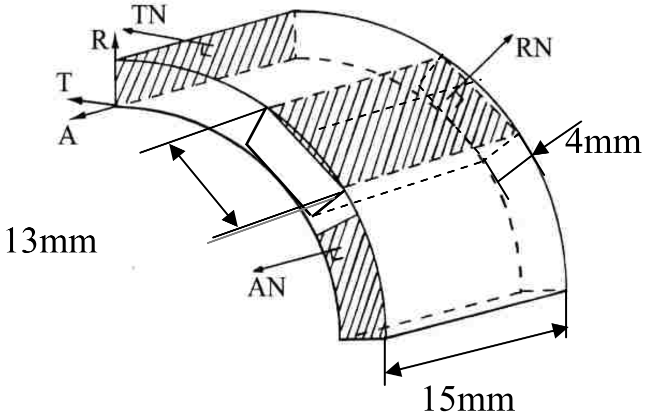

Fig. 3.1 Schematic diagram showing the sample coupon cutting method.

The samples were prepared following the conventional preparation procedure. First, the curved coupons were machined to be flat on both surfaces which had black oxide covering them. They were then ground using abrasive papers from grade 240 to 4000. After that, Al_2O_3 slurries were used to polish the samples on a rotating cloth until the surface roughness on both sides are about R_a=0.1±0.02μm. After polishing, the samples were first cleaned with distilled water and the 95% ethanol, and then dried for PEO treatment. Since, there were comparison studies made between the PEO coatings and the commercial black oxide coating, so some other coupons with the black oxide coating retained were cut to a similar geometric size for comparison.

To supply power current into the test coupons during the PEO process an titanium wire was inserted into a hole with a depth of 5mm, which was drilled from the top of the coupons.

3.3 Deposition process for PEO coatings

During the PEO process, a stainless steel hoop acts as the counter electrode. All the samples were polished, cleaned and degreased before the PEO process. After this pretreatment, the sample is connected to the anode of the power source unit and immersed into a bath containing the electrolyte to at a depth of 5mm to 10mm beneath the solution surface. The cathode of the power source unit is attached to the stainless steel counter-electrode. After activating the electrolyte cooling, mixing and gas exhaust systems, the working voltage can be applied to the electrolyser terminal. The PEO treatment is typically carried out for 0.85, 2 and 4min at current densities of 0.05, 0.1, 0.25Acm^{-2} and voltages of up to 400V. The temperature of electrolyte was kept below 60°C during the treatment. After the PEO process, the samples were taken out from the electrolyte, washed using distilled water and dried in air. All the samples were marked for further testing and analysis.

The frequency of DC power used in PEO process was 2000Hz. Two Na_2SiO_3+KOH solutions with concentration ratios of 8g/L: 0.8 g/L and 8g/L: 8 g/L were used as the electrolyte. The PEO treatment time and current density are listed in Table 3.3. Six sets of samples were divided into two groups (A and B) based on the two types of electrolyte.

Table 3.3 Treatment parameters for PEO coatings

Composition (Na_2SiO_3:KOH)	Sample No.	Current density(A/cm^2)	Treatment time (min)
Group A Electrolyte I (Ph=11-12) (8g/L: 0.8 g/L)	S1	0.05	4
	S2	0.1	2
	S3	0.25	0.8
Group B Electrolyte II (Ph=13-14) (8g/L: 8g/L)	S4	0.05	4
	S5	0.1	2
	S6	0.25	0.8

3.4 Evaluation of the properties of the coatings

3.4.1 Surface morphology and coating thickness

A JOEL Scanning Electron Microscope (SEM) (Fig. 3.2) at an operating voltage of 18keV was employed for the study of coating surface morphology. Electron Dispersive X-ray (EDX) analysis was used for chemical analysis of in the coatings and substrate. Before the SEM observation, a very thin layer of gold was deposited on the observation surfaces of the coated samples to provide electrical conductivity. The thicknesses of all six types of PEO coatings and black oxide were measured by SEM observation on cross-sections of the coatings. These samples were cut to be about 4-mm-thick sections normal to the Tangential-Radial surface and mounted with resin and polished to a mirror finish.

Fig. 3.2 JEOL Scanning Electron Microscope (SEM).

3.4.2 Phase identification of the coatings

The phase structures of the PEO coatings were investigated using a Siemens D5000 X-ray diffractometer (Cu K_a radiation) with a scan speed of 2 degree/min over a scan range of 10 to 150 degrees (in 2θ).

3.4.3 Surface roughness measurement

A Mitutoyo SJ-201P surface profiler (Fig. 3.3) with a data acquisition system was used to measure the surface roughness of all test samples. The black oxide coating can only be measured in the axial direction because of its curved surface.

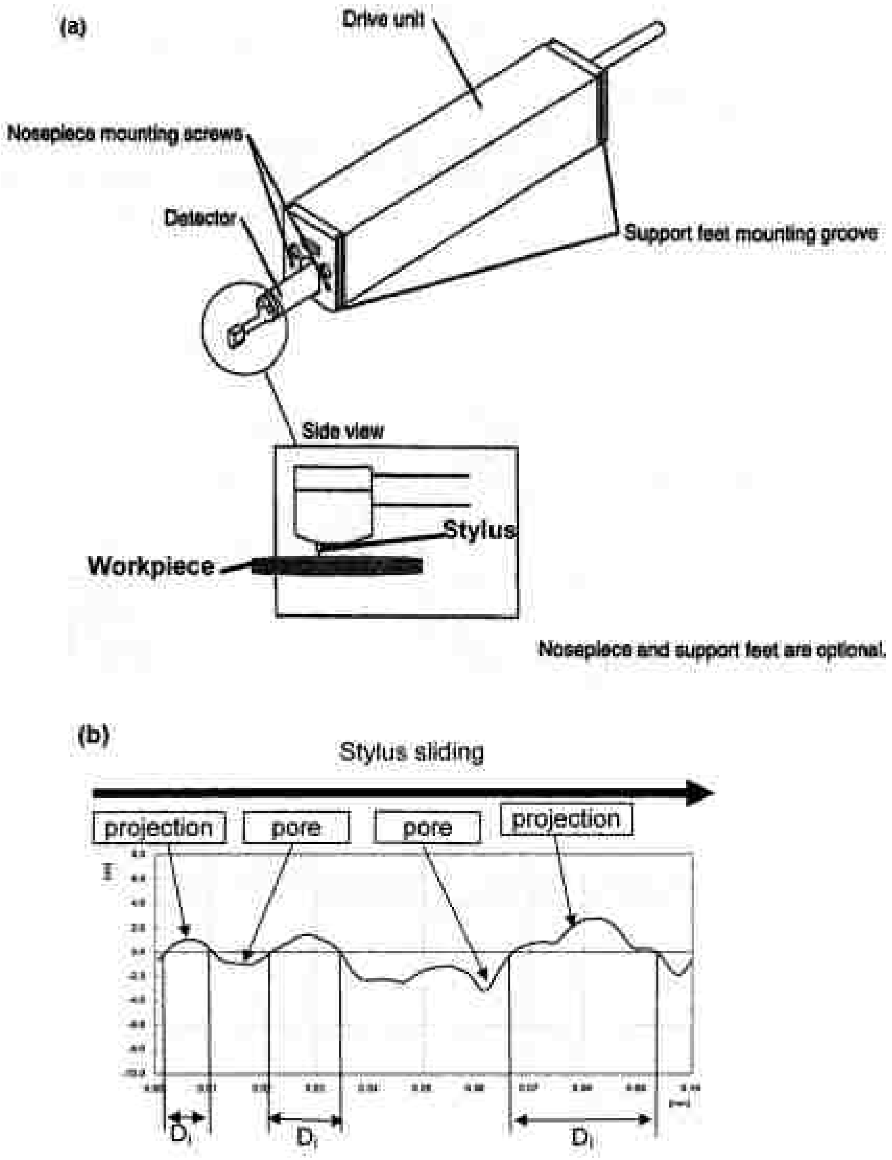

Fig. 3.3 Illustration of estimating the surface roughness of coating: (a) the detector unit of surface profilometer and (b) a typical surface profile plot.

3.4.4 Pin-on-disc tribology test

The wear tests were carried out on PEO coatings, Zr-2.5Nb substrate and black oxide coating by use of a Sciland Pin/Disc Tribometer PCD-300A (see Fig. 3.4) at room temperature. Two modes were used: rotating mode (sliding speed: 0.1 m/s) for flat samples (for substrate and PEO samples) and reciprocating mode (sliding speed: 0.08 m/s) for the curved samples (black oxide coating and PEO samples for comparison). The tribological behavior of the coatings under dry conditions were studied at a normal load of 2N against an Al_2O_3 pin. A 1000m sliding distance was used for all PEO coatings. The same test conditions were used for the black oxide coating but the test was stopped at coating failure. However, only a 50m sliding distance was used for the substrate under the same load, and its surface profile was measured across the wear track to study its width and depth.

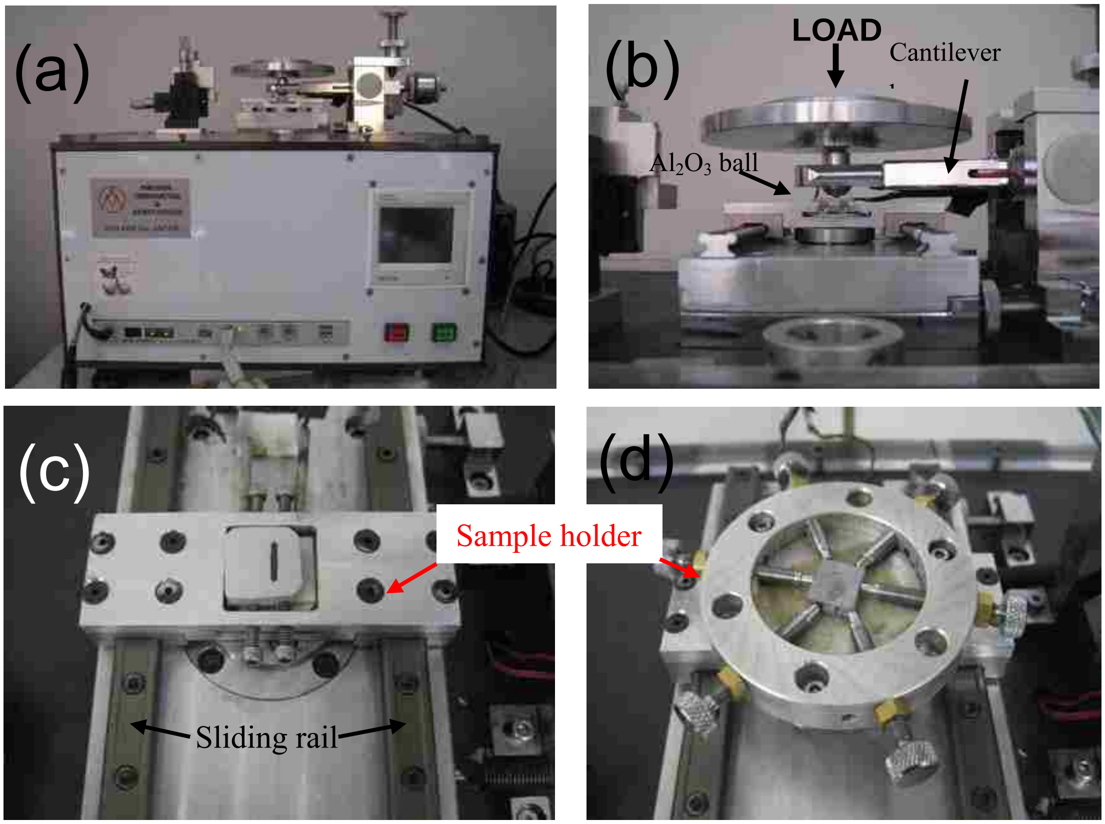

Fig. 3.4 Sliding tester attached on (a) Sciland Pin/Disc Tribometer PCD-300A (b) load cell and cantilever beam, (c) sample holder for reciprocating mode (d) sample holder for rotating mode.

3.4.5 Potentiodynamic polarization testing

3.4.5.1 Three-electrode cell

Potentiodynamic polarization tests were carried out using a Bio-Logic SP-150 potentiostat/galvanostat for uncoated, PEO-coated and inside surface of black oxide samples at room temperature (20 ºC) in a 4.8 wt.% (0.2mol/L or 1400ppm Li^+) LiOH solution which, as mentioned in Chapter 2, is very corrosive to Zr alloys [59, 60]. As seen in Fig. 3.5 (a and b), a three-electrode cell with the coated sample as the working electrode (WE), Ag/AgCl/sat KCl electrode as the reference electrode (RE), and a platinum rod as the counter electrode (CE) was used in the tests. The e exposure area of the samples exposed to the solution was 1 cm^2. The ratio of the volume of LiOH solution/sample area was 300ml/cm^2. After the electrochemical testing system became stable (20 to 30min), scans were conducted at a rate of 1mV/s from -0.5V versus open circuit potential in a more noble direction up to +2V versus the reference electrode.

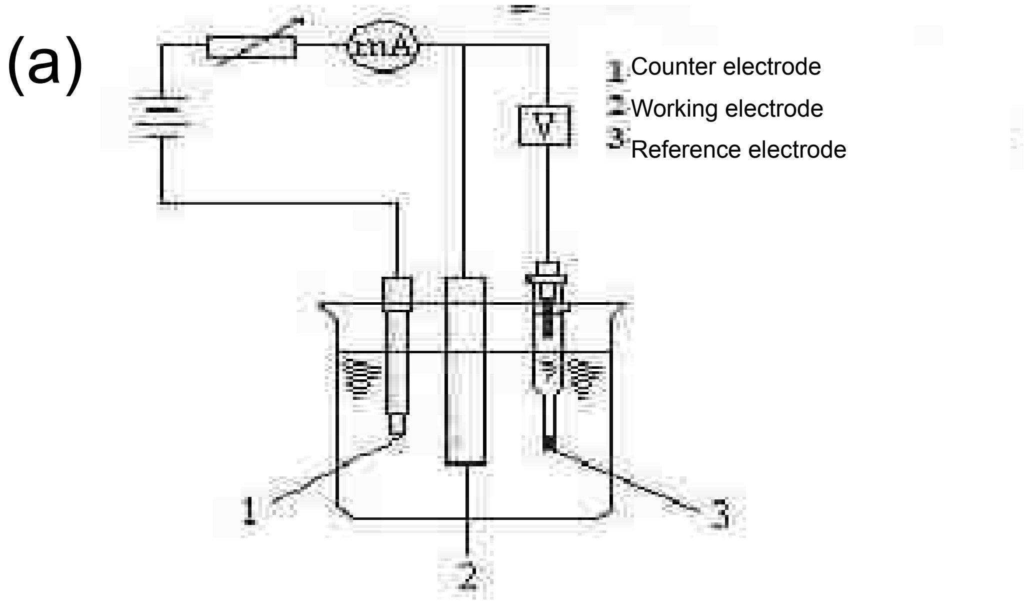

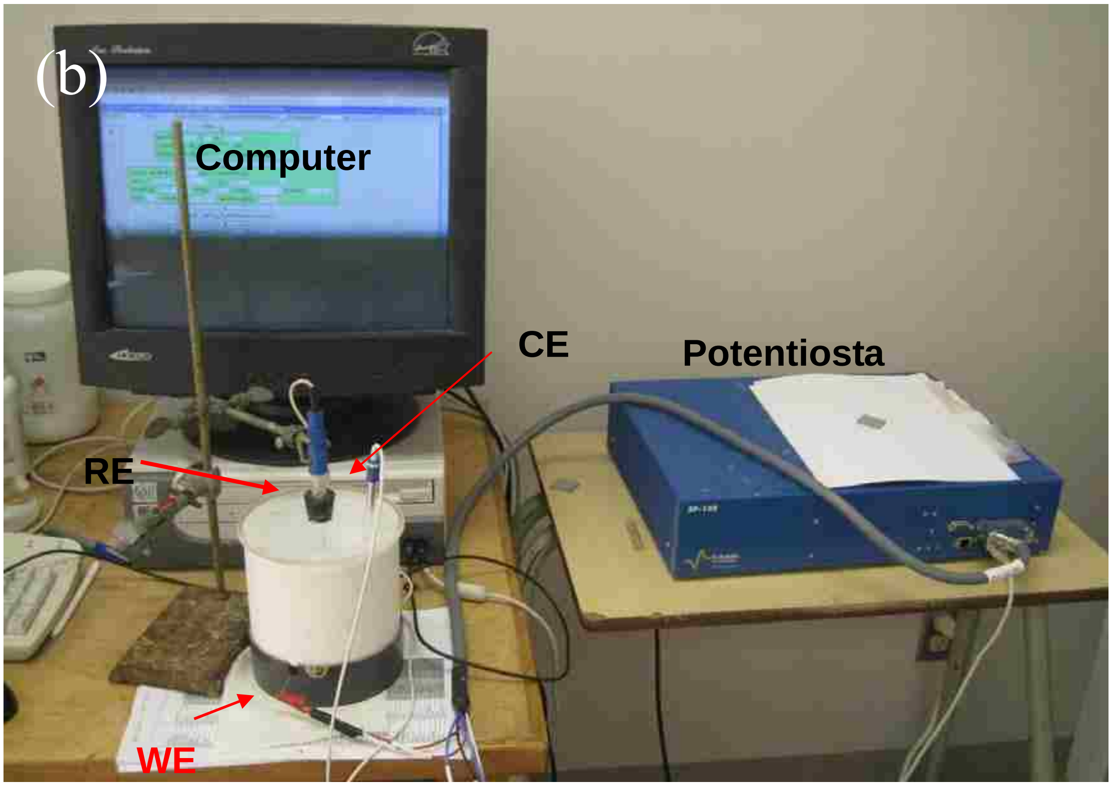

Fig. 3.5 (a) Schematic view of three-electrode cell and (b) Electrochemical corrosion polarization testing equipment.

3.4.5.2 The calculation of polarization resistance Ra

The determination of corrosion current density by extrapolation of linear parts of the polarization curves is illustrated in Fig. 3.6. The region of linearity is referred to as the Tafel region. The intersection point between the extrapolated Tafel regions gives the corrosion current density (i_{corr}).

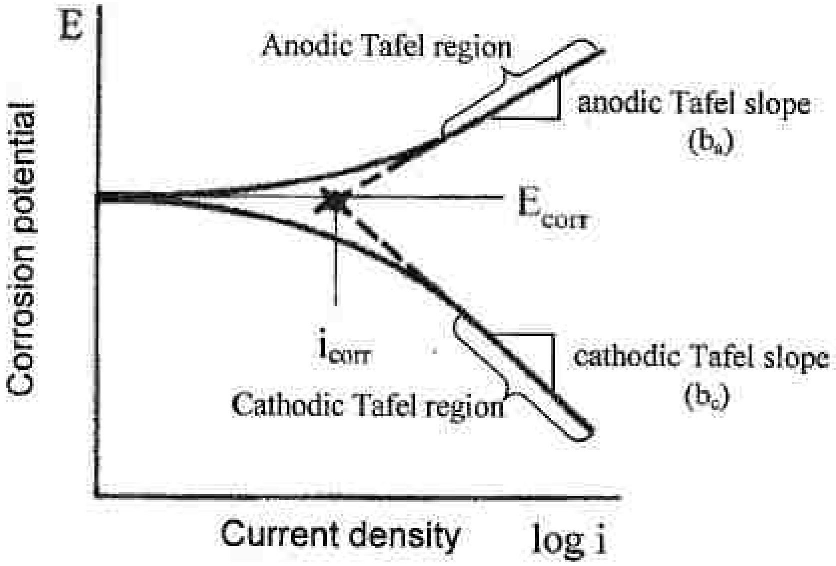

Fig. 3.6 Determination of corrosion current density by extrapolation of linear part of the polarization curve [88], i_{corr}—corrosion current density, E_{corr}—corrosion potential.

The potentiodynamic polarization tests were carried out on samples both before and after autoclave corrosion exposure for different times. All the samples, coated and uncoated, have their highest corrosion resistance before autoclave corrosion testing. However, the degradation of corrosion resistance is difficult to accurately estimate based only on the increase in sample weight because of spalling-off of the oxide. In these cases, the potentiodynamic polarization test was used to estimate the "residual" corrosion protection properties of all the samples: their polarization resistance was measured after each step of autoclave testing.

3.4.6 Autoclave experiment

An accelerated corrosion test involving 30-day autoclave exposure to high temperature (300°C), high pressure (10MPa) and 0.05mol/L LiOH solution was carried out to simulate the service conditions of pressure tubes. The autoclave tests were carried out in high temperature and pressure static autoclaves of 50cm^3 capacity. Fig. 3.7 shows the stainless steel autoclave together with copper gasket and sample holder .used in the test and Fig. 3.8 is a diagram showing the design of the autoclave. The copper gasket was used (between the autoclave and its lid) for better sealing. Samples were put on a steel sample holder and placed vertically in each autoclave. After that, the autoclave was filled with 40 mL freshly made LiOH solution (1.2g LiOH per liter deionized water/ 0.05M per liter) to accelerate the corrosion reaction. The autoclave was firmly sealed by six stainless steel bolts and placed in a furnace with a close temperature control (300±5°C). The test was interrupted at 2, 5, 10, 15, 30 days to refresh the LiOH solution and make measurements. In each period, the samples were removed from the autoclave, dried and weighed. Some samples of selected exposure times were then examined by potentiodynamic polarization tests and investigated by SEM and EDX. The others were then put back into the autoclave for another cycle. Because the potentiodynamic polarization tests caused the sample surface to corrode, and SEM examination required to sample surface to be gold-coated, those particular samples could no longer for used in further autoclave experiments. Thus, four coated samples which were made under the same PEO conditions were prepared at the beginning of the autoclave experiment. After the experiment, the weight gain of each type of coating was calculated from the average value of those samples. In addition, four uncoated substrate and four black oxide coated samples were also used during the experiment.

Fig. 3.7 Stainless steel (type 304) autoclaves with copper gasket on and steel sample holder.

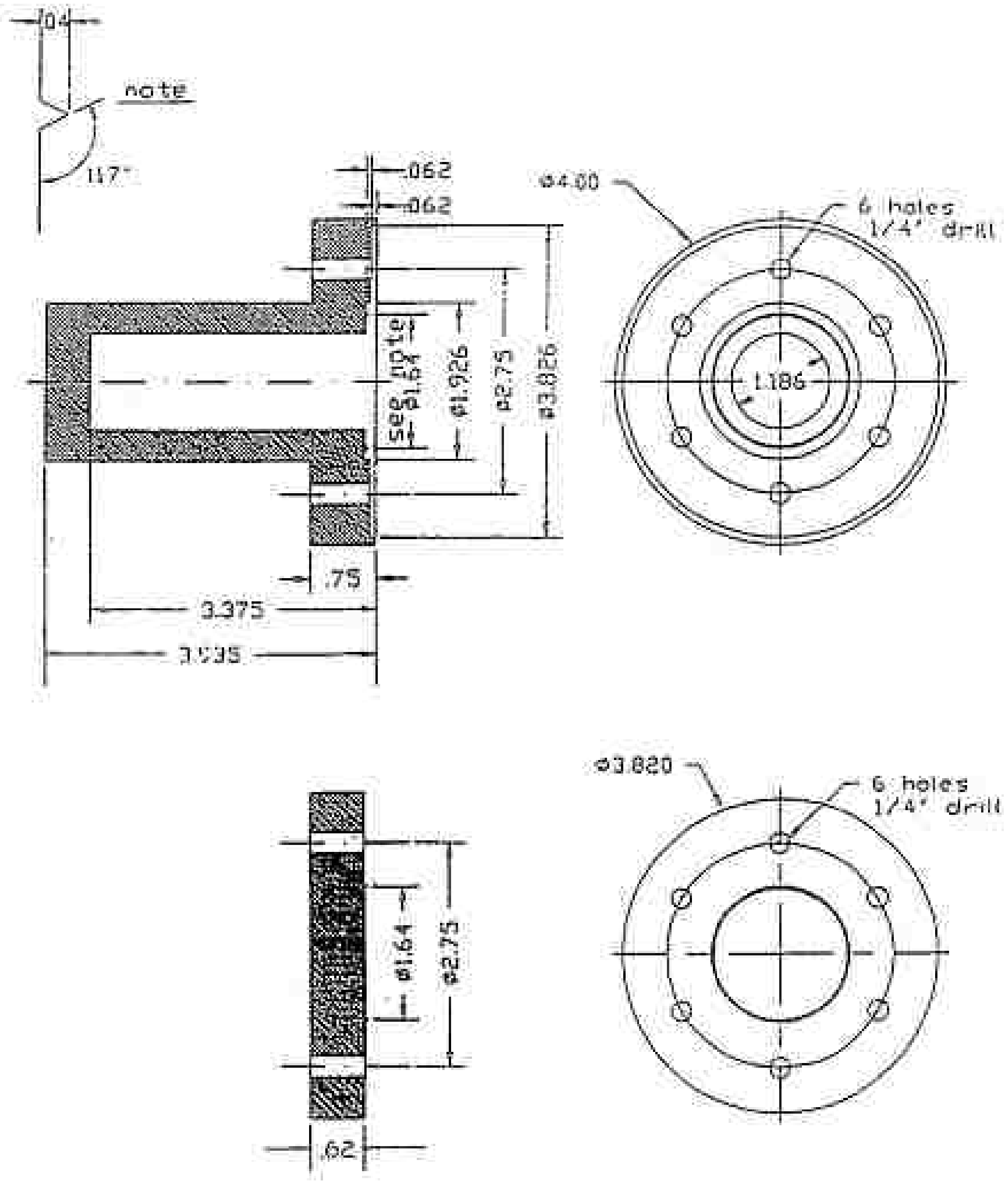

Fig. 3.8 Design of autoclave used for corrosion test.

3.4.7 Nano-hardness measurement

Given the small thickness of all samples in this study, nano-hardness measurements were made using a Ubi 1^{TM} nano-mechanical testing system. In this test, a Berkovich indentor (Fig. 3.9) was used with a linear load function. The peak load was 1000μN with segment time of 10 seconds. Fig. 3.10 (a) and (b) are typical Force-Displacement curves which used to calculate the Young's modulus and nano-hardness of PEO-coated sample S1 and uncoated substrate. At least six points on the sample surface were recorded and averaged to calculate the nano-hardness of the coatings.

Fig. 3.9 Ubi 1^{TM} nano-mechanical testing system and Berkovich tip used in hardness test.

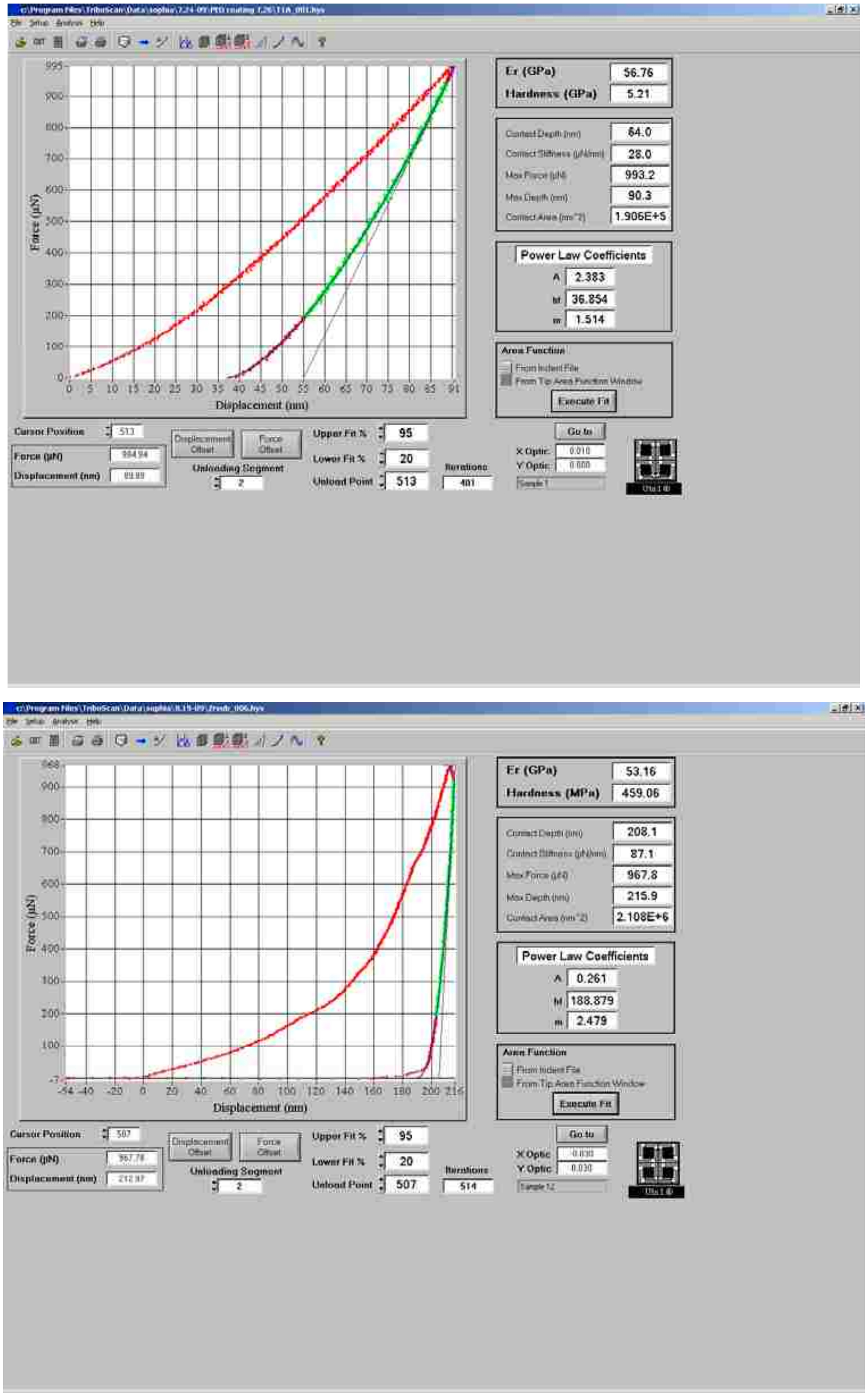

Er (GPa) 56.76
Hardness (GPa) 5.21
Contact Depth (nm) 64.0
Contact Stiffness (µN/nm) 28.0
Max Force (µN) 993.2
Max Depth (nm) 90.3
Contact Area (nm^2) 1.906E+5
A 2.383
hf 36.854
m 1.514
Cursor Position 513
Force (µN) 994.94
Displacement (nm) 89.89
Unloading Segment 2
Upper Fit % 95
Lower Fit % 20
Unload Point 513
Iterations 401
X Optic 0.010
Y Optic 0.000

Er (GPa) 53.16
Hardness (MPa) 459.06
Contact Depth (nm) 208.1
Contact Stiffness (µN/nm) 87.1
Max Force (µN) 967.8
Max Depth (nm) 215.9
Contact Area (nm^2) 2.108E+6
A 0.261
hf 188.879
m 2.479
Cursor Position 507
Force (µN) 967.78
Displacement (nm) 212.97
Unloading Segment 2
Upper Fit % 95
Lower Fit % 20
Unload Point 507
Iterations 514
X Optic 0.030
Y Optic 0.030

Fig. 3.10 Typical Force-Displacement curve in nano-hardness testing: (a) PEO coating S1 and (b) Zr-2.5Nb substrate.

Chapter 4: EXPERIMENTAL RESULTS AND DISCUSSION

4.1 Microstructure of Zr-2.5Nb alloy

Fig. 4.1 shows a SEM micrograph of an radial-tangential section of the Zr-2.5Nb substrate after etched by a solution of 45 parts HNO_3: 45 parts H_2O:10 parts HF. The distribution of the α-Zr (lighter phase) and β-Zr can readily be seen. There are also indications of some hydride (white phase).

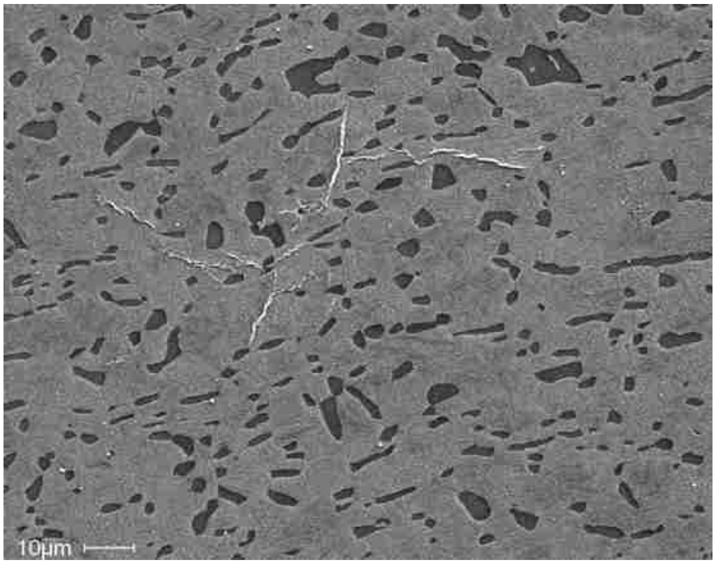

Fig. 4.1 SEM micrograph of etched radial-tangential section of Zr-2.5Nb substrate parallel to axial direction of pressure tubing.

4.2 Characterization of PEO coatings

4.2.1 The characteristics of the PEO process using DC power with a Zr-2.5Nb alloy

In order to study the characteristics of the PEO coating process with a DC power source for Zr-2.5Nb, a long processing time was employed at 0.1A/cm^2 current density with an Na_2SiO_3:KOH=8 g/L: 0.8 g/L electrolyte. The experiment was not paused until the terminal voltage promptly dropped and fluxed, i.e., some areas on the coating surface break down due to the high electric field gradient. During the PEO treatment, the voltage increased with time and it value was recorded every 6 seconds.

Fig. 4.2 shows that there are four stages in the voltage vs. processing time curve. The first three stages have near-linear slopes: at the beginning of the process (in the first 0.35min), the voltage increased sharply from 0 to around 150V (at a rate of 430V/min) then slowed down but was still increasing (at a rate of 48V/min). At the same time, the color on the coating surface kept changing from an iridescent color to dark grey and then became lighter and lighter. After a time t=3.7min, the voltage stabilized at a value of 310V for 3min and then increased again at t=6.7min. However, after that point, the increase of voltage with time is not linear but is wavy and the voltage finally attained a maximum value of 403V at t=8min. After the peak value point, the voltage undergoes considerable fluctuation with an overall trend to decrease. This indicates that the PEO coating was penetrated through to the substrate. When observed by the naked eye, there were bright and large discharges distributed on some areas of coating surface and these discharges kept moving slowly over a small area

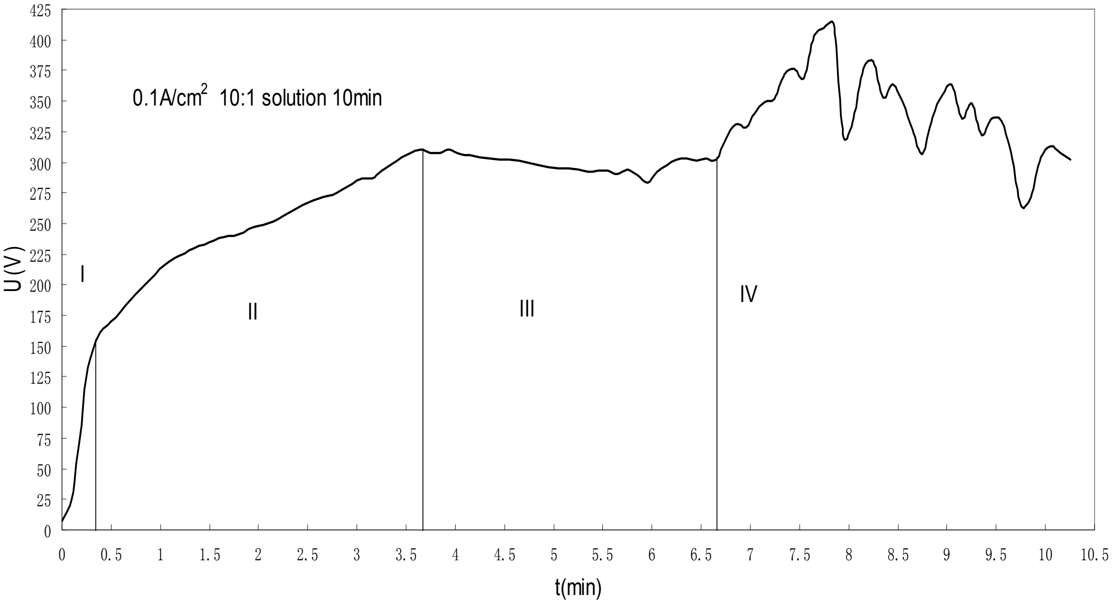

Fig. 4.2 Voltage vs. time for a 10min PEO treatment on Zr-2.5Nb.

After failure of the coating, the PEO treatment was stopped. The failed coating was washed, dried and studied by SEM. The morphology of the 10 min-treated PEO coating is shown in Fig. 4.3.

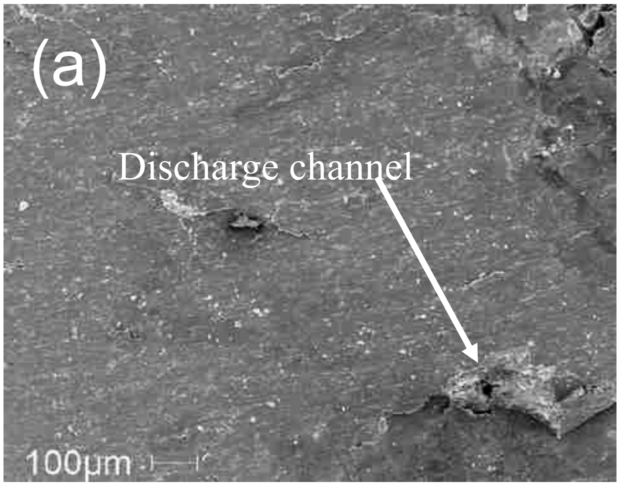

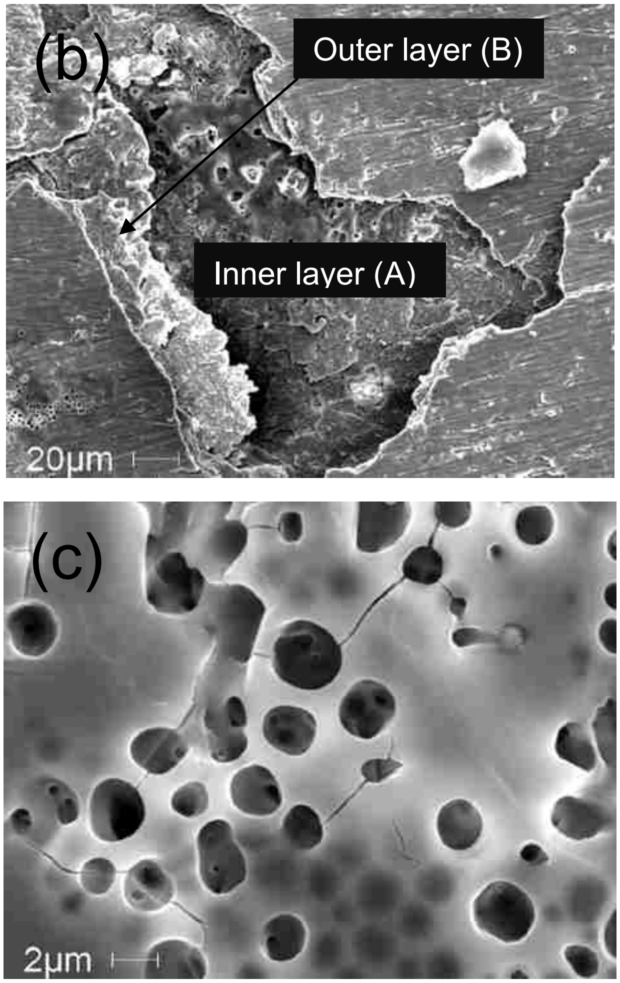

Fig. 4.3 Surface morphology on 10 min-treated PEO coating. (a and b) discharge channel and the breakaway of PEO coating and (c) melted areas.

Fig. 4.4 is the EDX spectra which show the chemical concentration in the melted area (A) and broken surface area (B) of Fig. 4.3(b), respectively. High silicon concentrations could be seen at the discharge channel areas (Fig. 4.4(b)). This could be explained by the formation of complex Zr-O-Si compounds around the discharge channel areas. According to Matykina et al.'s study [10], a much higher Si:Zr ratio was found in the porous outer layer than in the dense intermediate layer. However, for the 10min PEO coating in this study, although most of the outer layer was still intact, in some localized areas, the coating was totally broken down and the inner layer was exposed to the electrolyte. The sudden breakdown of the outer layer could cause a sudden rise of electrical current in that area which melted material over a small area (Fig.4.3 (c)) and there was an intense reaction with the electrolyte which generated large amounts of O and Si. This sudden breakdown of the oxide layer and the change of electrical field may also be the reason why voltage oscillated dramatically when exceeding a critical value (see Fig. 4.2).

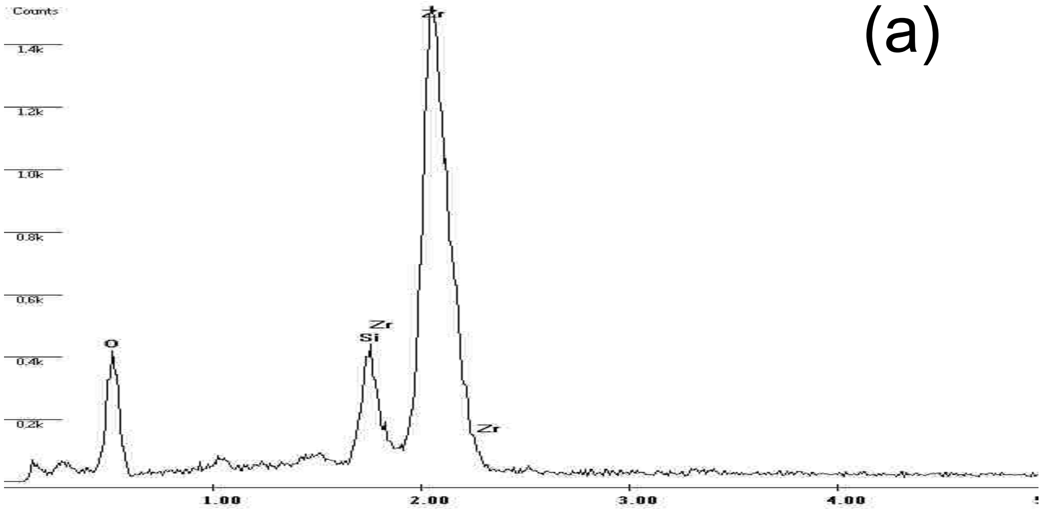

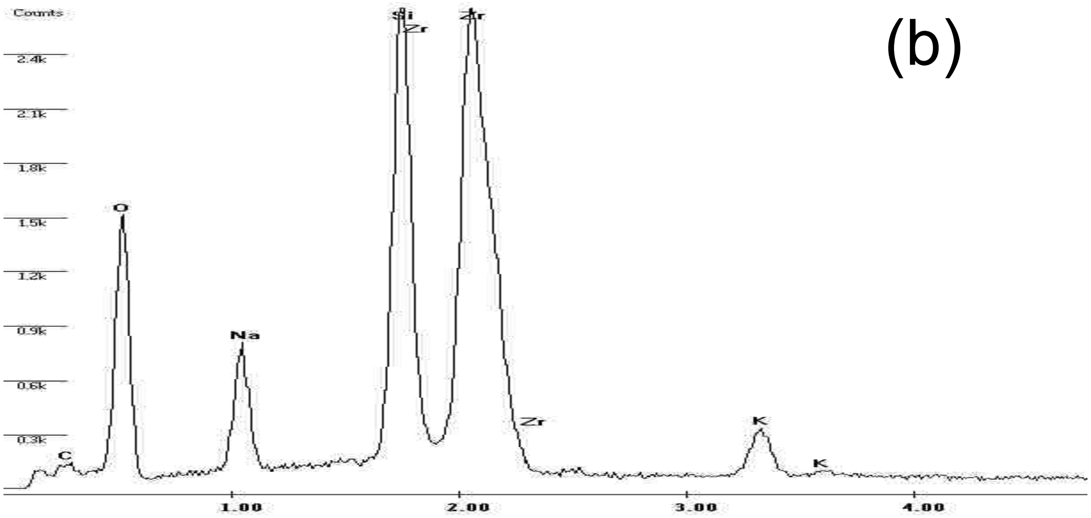

Fig. 4.4 EDX spectra on melted area (A) and broken surface area (B) of Fig. 4.3(b), respectively.

After the 10 minute treatment, the pearl white PEO coating surface became very rough. The surface profiles of Zr-2.5Nb polished substrate, samples made at 0.1A/cm^2 for 2min (S2) and 10min are shown in Fig. 4.5 (a to c), respectively. In Fig.4.5 (c), large “cracters” which have a depth of as much as 30 μm and a width of over 1mm were observed.

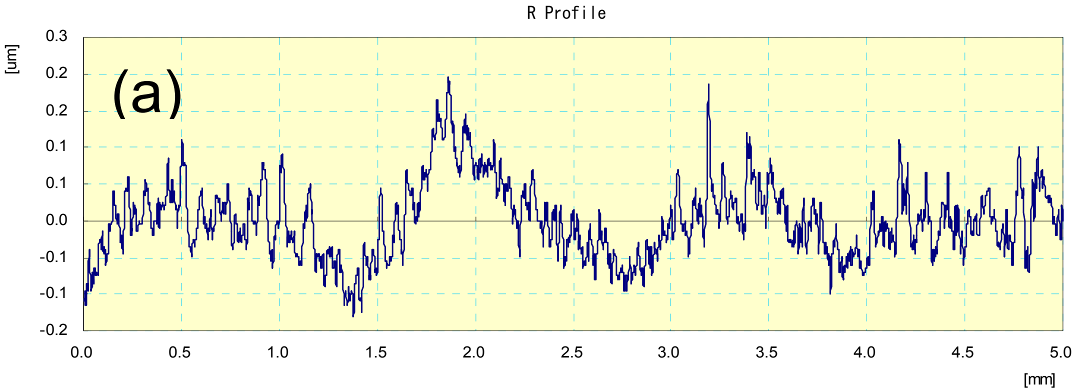

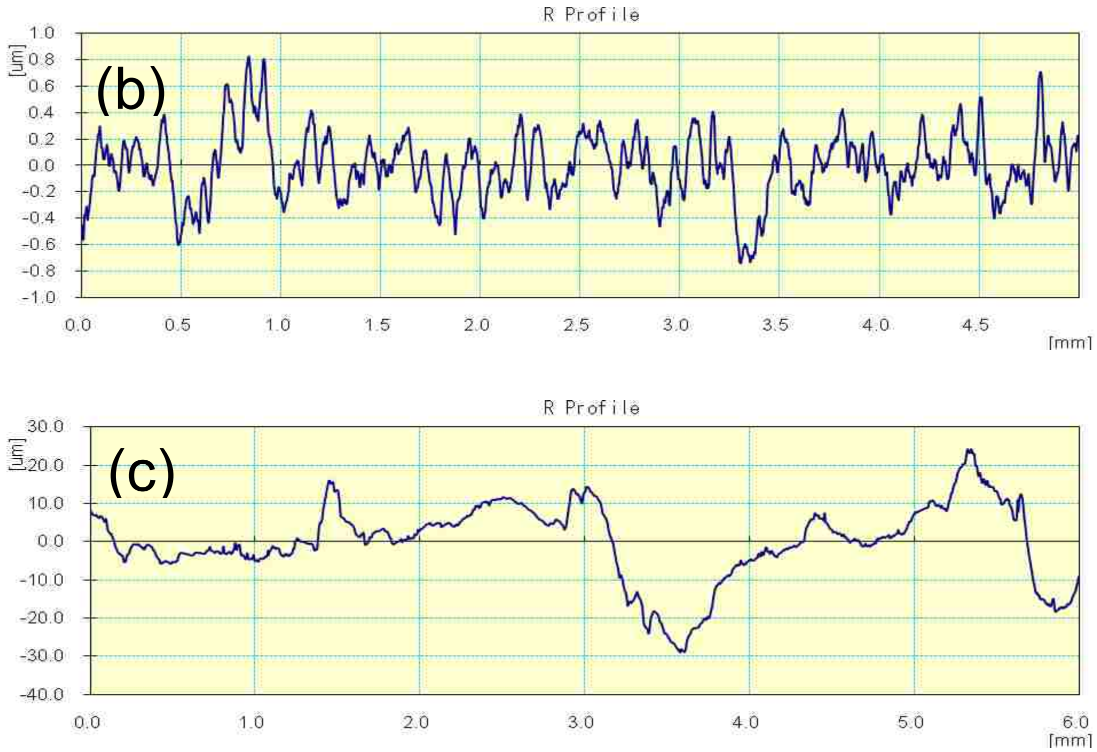

Fig. 4.5 Surface profiles for (a) fresh polished Zr-2.5Nb substrate and (b and c) PEO coatings made at 0.1A/cm^2 for 2min (S2) and 10min.

4.2.2 Voltage increment curve analysis during PEO process

Based on the results in the section **4.1.1**, a long PEO treatment time was not beneficial in making a uniform, adherent coating on the Zr-2.5Nb alloy. On the other hand, the use of a high current density in making a PEO coating had other disadvantages. During the PEO treatment, there will be some discharge lost from the connection point of sample and titanium wire. This loss became severe and could not be neglected when the current rose to a critical value. Furthermore, a high current density induces a rapid increase of temperature of the electrolyte close to the coating surface, which will decrease the efficiency of the reaction. On the other hand, for applications in nuclear reactors in electrical power generation, too thick a coating has adverse heat transfer effects in service and the energy cots for the PEO treatment are much increased. After several pre-tests, we decided that when the current density I times processing time t equals 0.2 (I×t=0.2) would make good PEO coatings. If I×t>0.2, the color of the PEO coating becomes light grey and exhibits an unsatisfactory performance in the later mechanical tests.

For this study, three sets of current density: treatment time were used (see Table 3.3 for details) together with two concentrations of electrolyte. Thus, six sets of PEO coatings were made. Figs. 4.6 (a) and (b) show the voltage vs. time plots of all six sets of PEO coatings. From a comparison of the plots, it can be seen that the voltage vs. time behavior was mainly affected by current density.

For a low current density (0.05A/cm^2), S1 and S4, there appears to be three stages in the PEO process:

Stage 1: Anodizing process with a rapid linear increase of voltage (<0.4min for S1 and <0.7min for S4);

Stage 2: Voltage still increasing, but not as rapidly as Stage 1 due to the low conductivity of zirconium oxide layer (0.4~2.5min for S1 and 0.7~2.4 for S4).

Stage 3: Voltage virtually remains constant at a value of about 220V but fluctuates in the range of ±3V due to the stability of the electrical field. No discharge was observed at any of the three stages.

For an intermediate current density (0.1A/ cm^2), S2 and S5, there appears to be only two stages, which are similar to the Stages 1 &2 for the low current density group. The process was terminated during the increasing of voltage in the on-going progress of Stage 2. PEO is a technique that operates at potentials above the breakdown voltage of an oxide film growing on the surface of a passivated metal anode. During Stage 2, with the increase of voltage, local discharge occurred due to a tip/corner effect of electrical field concentration. In these local discharge areas, the temperatures are instantaneously extremely high, however, the bulk substrate temperature is below 100° C [3].

The curves for S1 and S2 are very similar to their counterparts, S4 and S5 made in the different electrolyte. However, for the high current density (0.25A/ cm^2), S3 and S6, a different behavior was seen in the two electrolytes. The voltage for S6 rose slower than that for S3 and the final voltage value was only 300V, compared to 400V for S3. Intense gas and heat release and discharge production took place during almost all of the process time for both electrolytes.

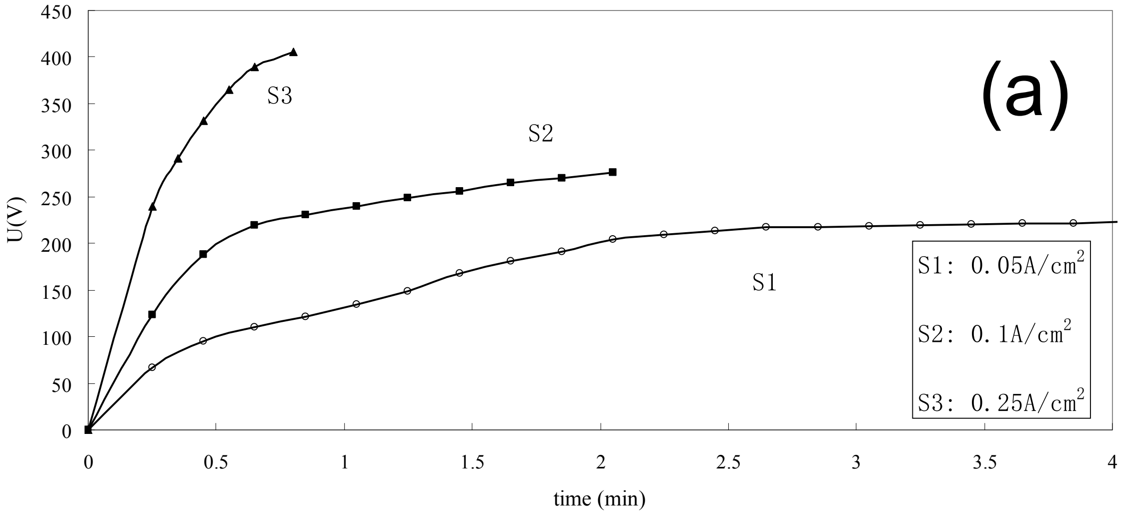

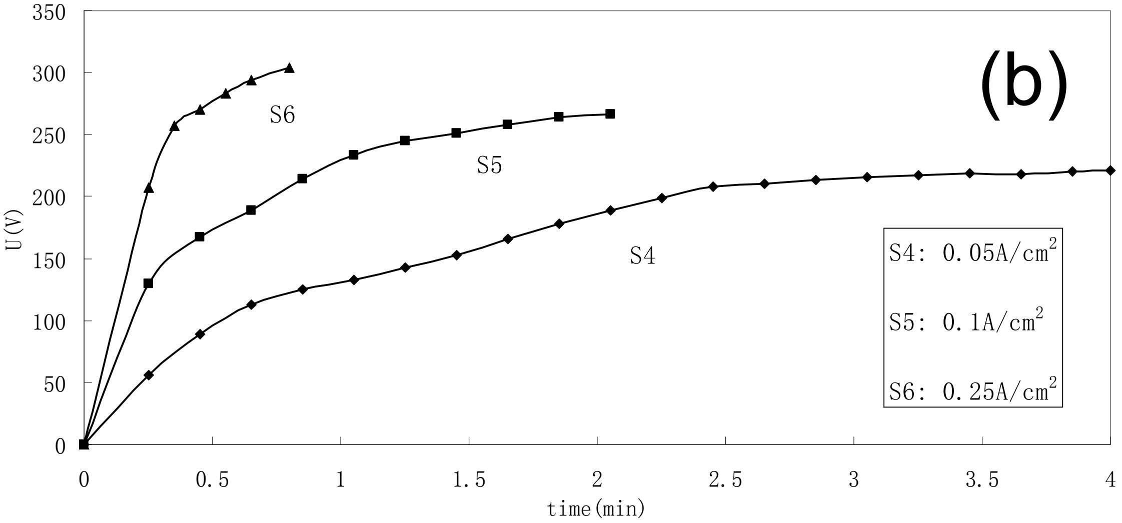

Fig. 4.6 Voltage U vs. treatment time t of all six sets of PEO coated samples: (a) samples of Group A and (b) samples of Group B.

4.3 SEM and EDX analysis

SEM examinations were made of both the coating surface and cross-sections through the sample thickness. SEM micrographs of all six sets of PEO coatings (S1 to S6) and the commercial black oxide coating are shown in Fig. 4.7 for the surface morphology and Fig. 4.8 for the cross-sections.

Fig. 4.7 reveals that there were a number of micro-pores and micro-cracks distributed on the surface of all PEO coatings. However, sample S1and S4, which were fabricated at a current density of 0.05A/cm^2, exhibited a relatively dense, continuous oxide film. Samples S2, S3 and S5, S6, which were fabricated at higher current densities (0.1A/cm^2 and 0.25A/cm^2) showed more porosity. At higher current densities, the plasma discharges are more intense in the metal matrix-coating-electrolyte system, and the discharge channels were formed inside the insulated oxide. Some of those discharge channels remained and formed micro-pores which penetrated the localized coating areas (Fig. 4.8 (b, c, e and f)). The black oxide coating had a much rougher surface (Fig. 4.7 (e)) compared to the PEO coatings, probably due to the different original substrate surface finish.

The thicknesses of the PEO coatings and the black oxide coating were measured using the cross-sectional micrographs, Fig. 4.7. The value of the thicknesses and their variations are summarized in Table 4.1. Brief comments are made on each sample. From Figs. 4.8 (a-f) and Table 4.1, we can see that a near constant thickness, 5 to 6 μm, coatings were produced on all PEO samples. However, due to the longer processing time (4 min), the coating thickness on samples S1 and S4 was slightly higher than that of the other two samples in the same Group (S2, S3 and S5, S6). Samples S3 and S6, which were made at the highest current density and shortest time, showed an irregular substrate-coating interface. Samples S1 and S4, on the contrary, exhibited a very constant thickness over the whole sample surface. Discharge channels could be observed in the cross-sections of all PEO coatings except for S1 and S4. Fig. 4.8 (g) shows a 1~1.5 μm thick, discontinuous black oxide coating which adhered well to the rougher pressure tube inner surface.

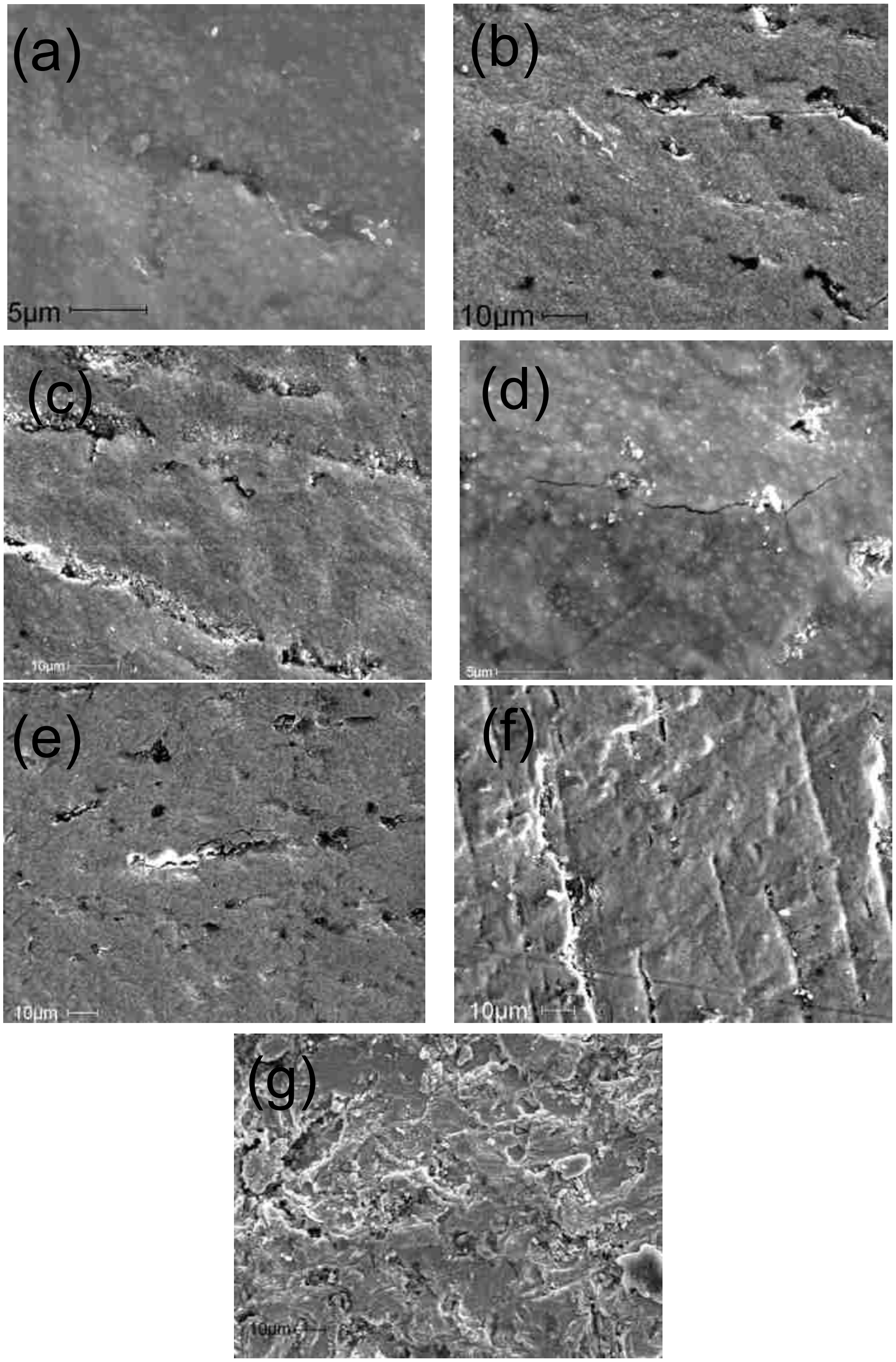

Fig. 4.7 SEM micrographs on the morphology of (a to f) PEO coatings S1 to S6 and (g) the black oxide coating.

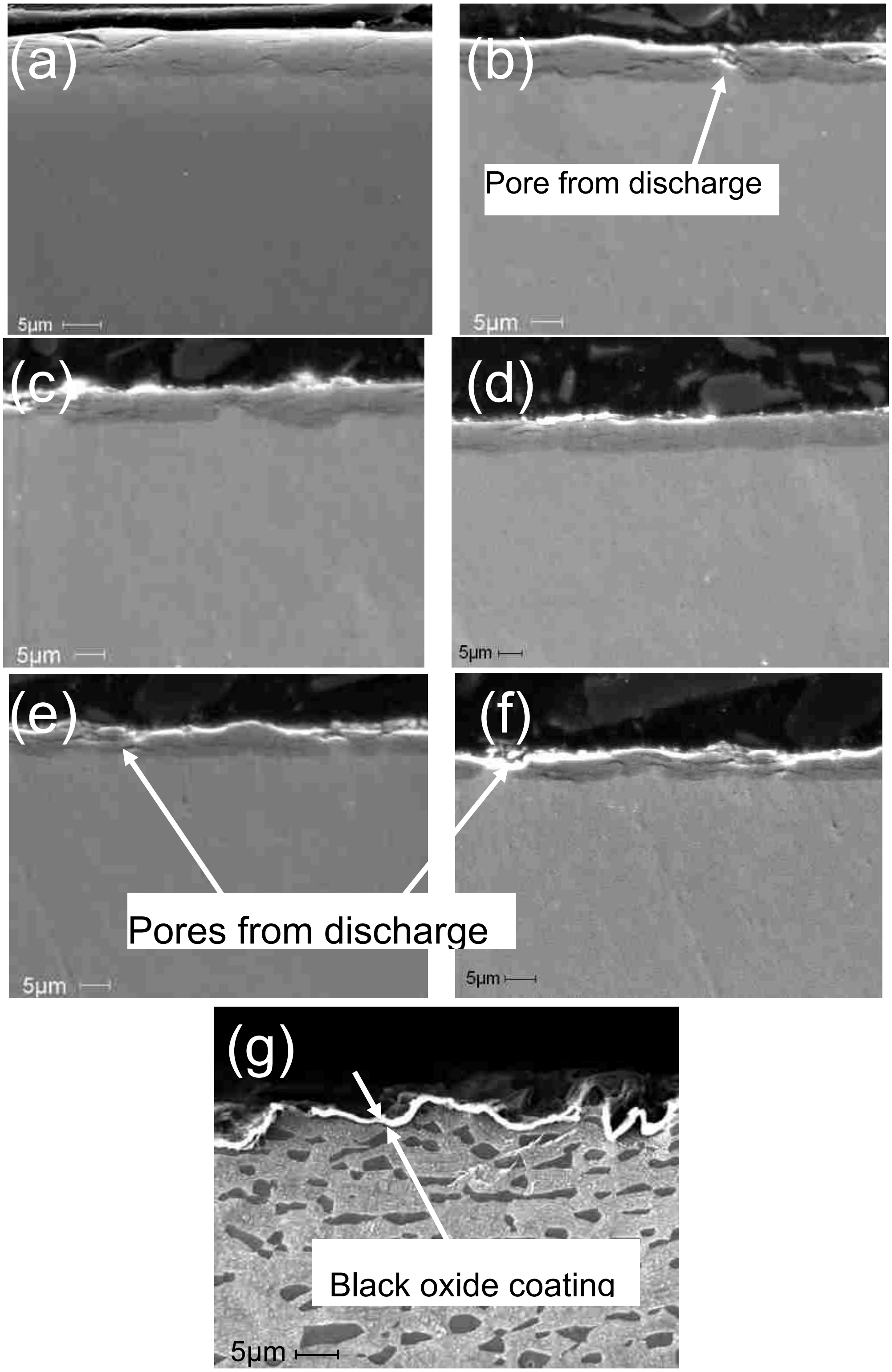

Fig. 4.8 Cross-sectional SEM micrographs at different magnifications of the PEO coatings. (a-f) PEO coatings from S1-S6 and (g) the black oxide coating.

Table 4.1 Average thickness of PEO coatings measured on cross-sectional SEM micrographs

Samples	Thickness of the PEO coating (μm)	Brief comments
S1	5.8±0.3	Smooth coating area; regular substrate-coating interface
S2	5.7±0.5	discharge channels; some cracks parallel to the substrate/oxide interface
S3	5.3±0.6	Irregular substrate-coating interface; discharge channels; some cracks parallel to the substrate/oxide interface
S4	5.8±0.2	Smooth coating area; regular substrate-coating interface
S5	5.7±0.4	discharge channels; some cracks parallel to the substrate/oxide interface
S6	5.1±0.5	Irregular substrate-coating interface; discharge channels; some cracks parallel to the substrate/oxide interface

The surface roughness of the PEO coatings is much less than the black oxide coating. All of PEO coatings have a similar surface profile according to the surface roughness tests. Fig. 4.9 shows the surface roughness data, R_a, measured from one of the PEO coatings (S1) and the inner surface of the black oxide coating.

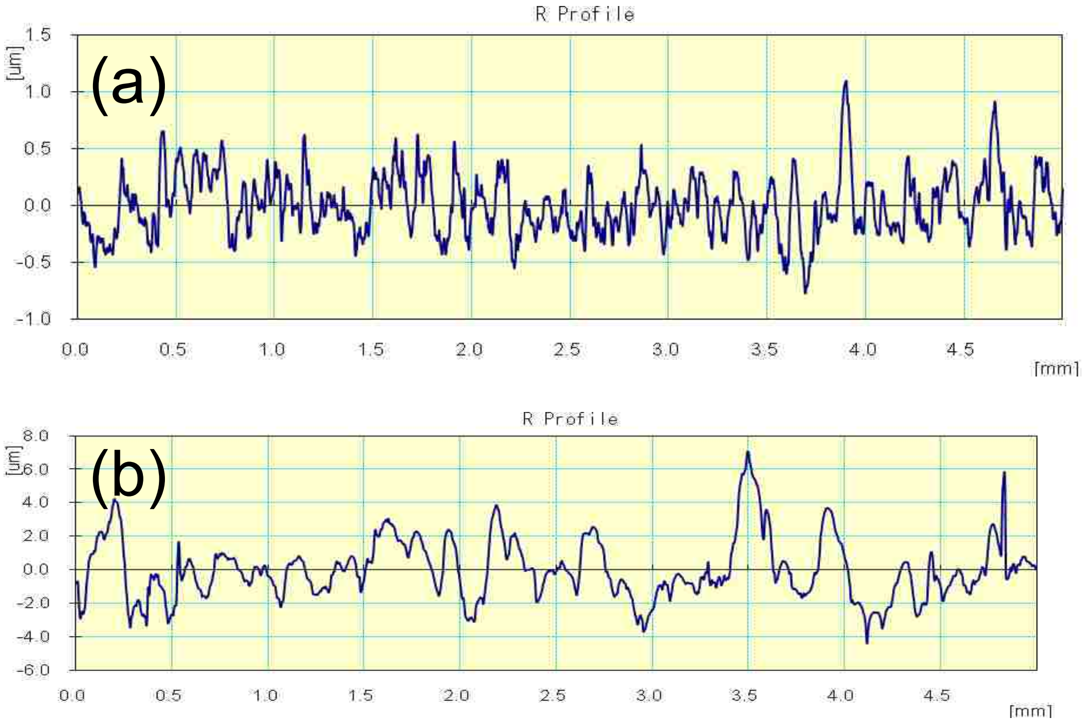

Fig. 4.9 Surface profiles of (a) PEO coating sample S1 and (b) inner surface of black oxide coating.

From Fig. 4.9, it is clear that the PEO coating, which was about 5 to 6 μm thick, has a much smoother surface (Ra is in the range of 0.2-0.4 μm) compared to the black oxide coating where has Ra≈1.5 μm. Fig. 4.10 shows the surface roughness Ra data for all coated samples. It is known that for the same current density, the surface roughness increases with the treatment time. However, for short periods of treatment (before Stage 3 in PEO process), a small current density produces a smoother coating surface because a larger current density produces intense discharges.

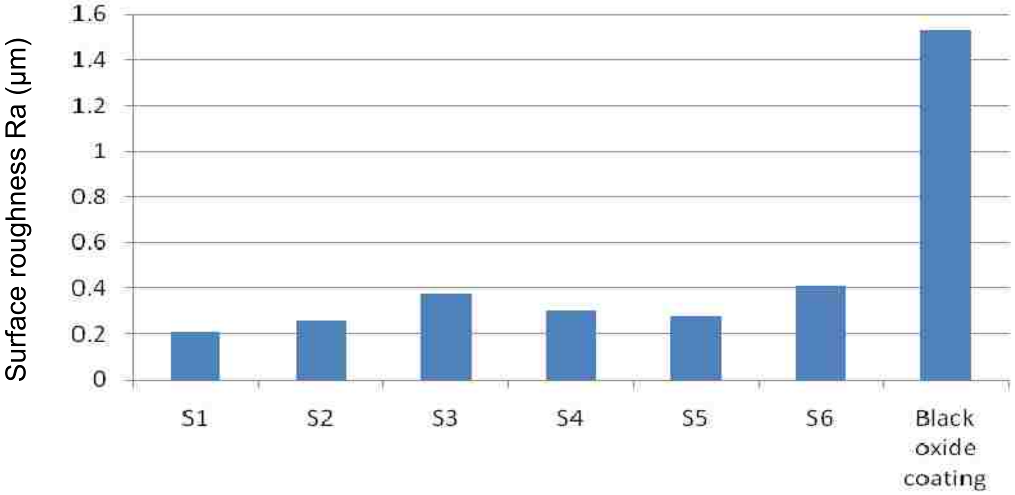

Fig. 4.10 Surface roughness Ra for thePEO coatings and the black oxide coating.

4.4 Chemical analysis of the coatings

4.4.1 EDX spectra for coated and uncoated samples

Fig. 4.11 shows typical EDX spectra for Zr-2.5Nb substrate, PEO coating S1 and black oxide coating. All six sets of PEO coatings had an almost same EDX spectra which had a much higher oxygen concentration than the black oxide coating. As seen in Fig. 4.11, only Zr and O could be found in EDX spectra, the alloying elements (Nb, Fe, etc.) could not be observed, possibly due to their low concentration.

During the PEO process, complex compounds can be synthesized inside the high voltage breakthrough channels formed across the growing oxide layer. These compounds are composed of oxides of both the substrate material (zirconium) and electrolyte-borne modifying elements (silicon). Thus, theoretically, complex Zr-O-Si compounds should exist inside coating area. However, the PEO processing times were too short to produce very intense discharges on the coating surfaces. Si might help to accelerate the formation of the coating and does exist in the coating but could not be observed due to its extremely low concentration. For longer PEO treatment, Si has been found (Fig.4.4).

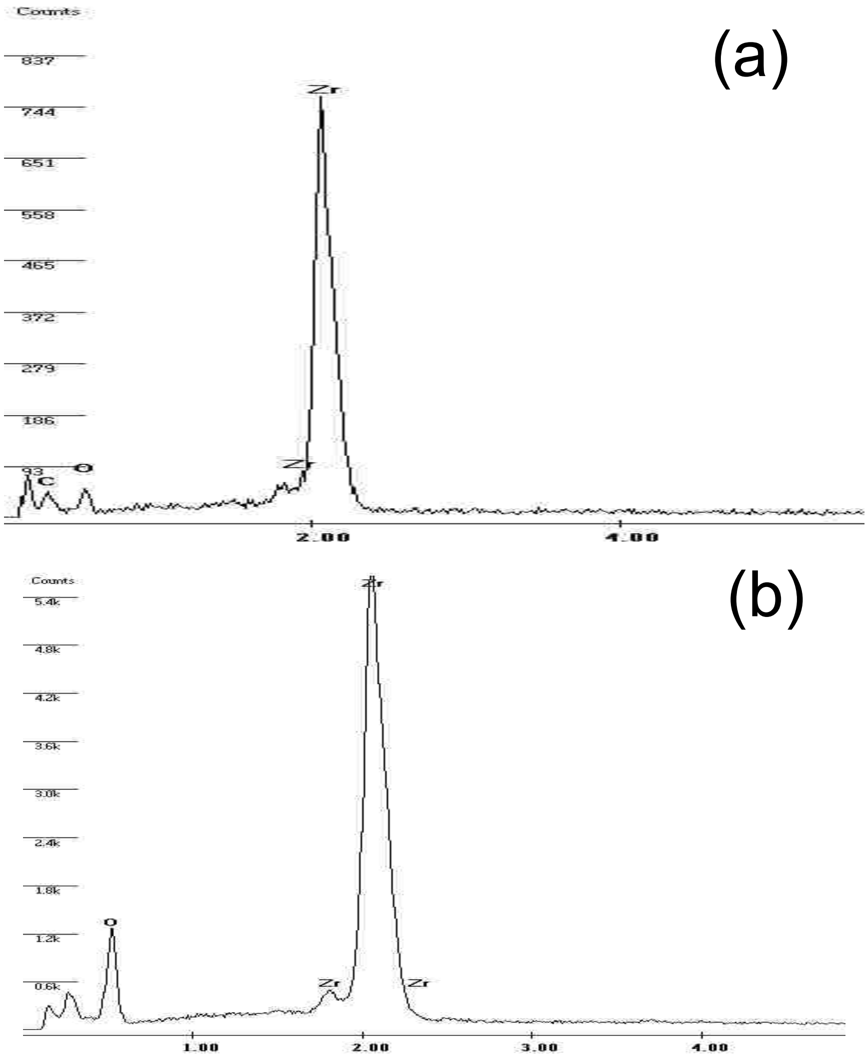

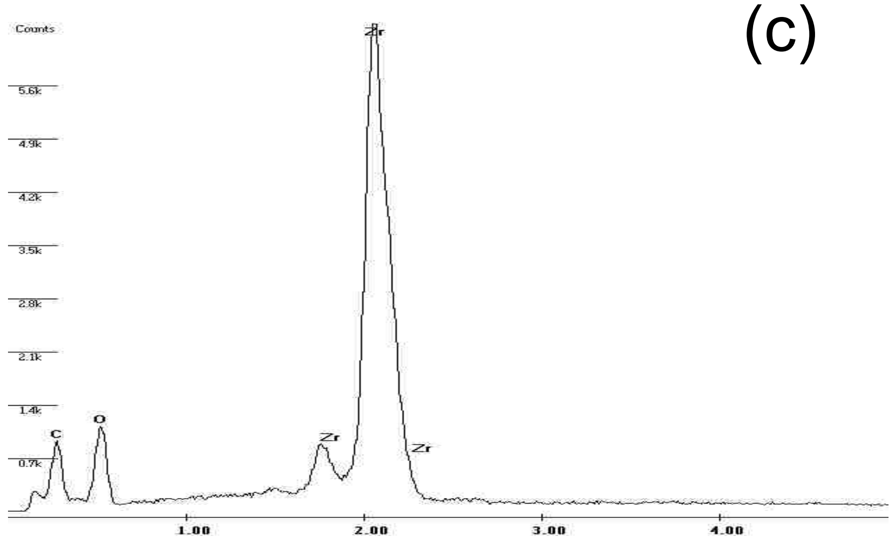

Fig. 4.11 EDX spectra for the surface of (a) Zr-2.5Nb substrate, (b) PEO-coated sample S1 and (c) The black oxide coating.

4.4.2 XRD patterns for coated and uncoated samples

Fig. 4.12 shows the XRD patterns of Zr-2.5Nb substrate, the black oxide coating and PEO coating S1. MDI jade 5.0 software was used to fit the XRD pattern peaks and identify the phases present. Only peaks from the Zr-2.5Nb substrate and zirconium oxide could be identified. For the black oxide coating, a suboxide Zr_3O could be identified (Fig. 4.12 (b)). This type of zirconium oxide is probably metastable inside the coating since some studies have shown that α-zirconium can dissolve up to 29% oxygen, without forming any chemical compound [43]. The PEO coating S1 was mainly composed of the monoclinic ZrO_2 (m- ZrO_2) and the tetragonal ZrO_2 (t-ZrO_2) phases, but the t-ZrO_2 content was much lower than the m- ZrO_2 (Fig. 4.12 (c)).

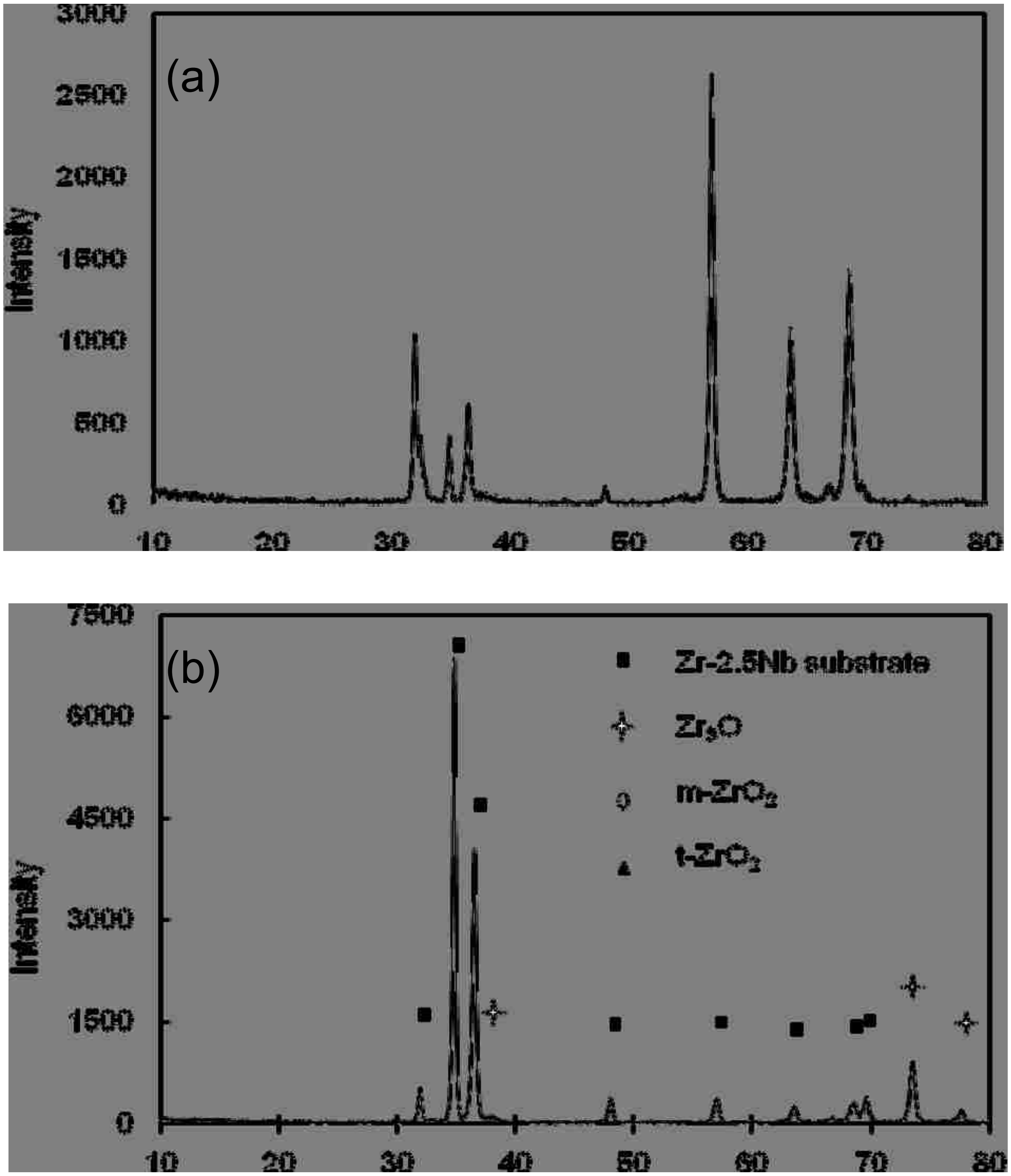
(a)
Intensity
3000
2500
2000
1500
1000
500
0
10
20
30
40
50
60
70
80
(b)
Intensity
7500
6000
4500
3000
1500
0
10
20
30
40
50
60
70
80
■ Zr-2.5Nb substrate
Zr$_3$O
m-ZrO$_2$
t-ZrO$_2$

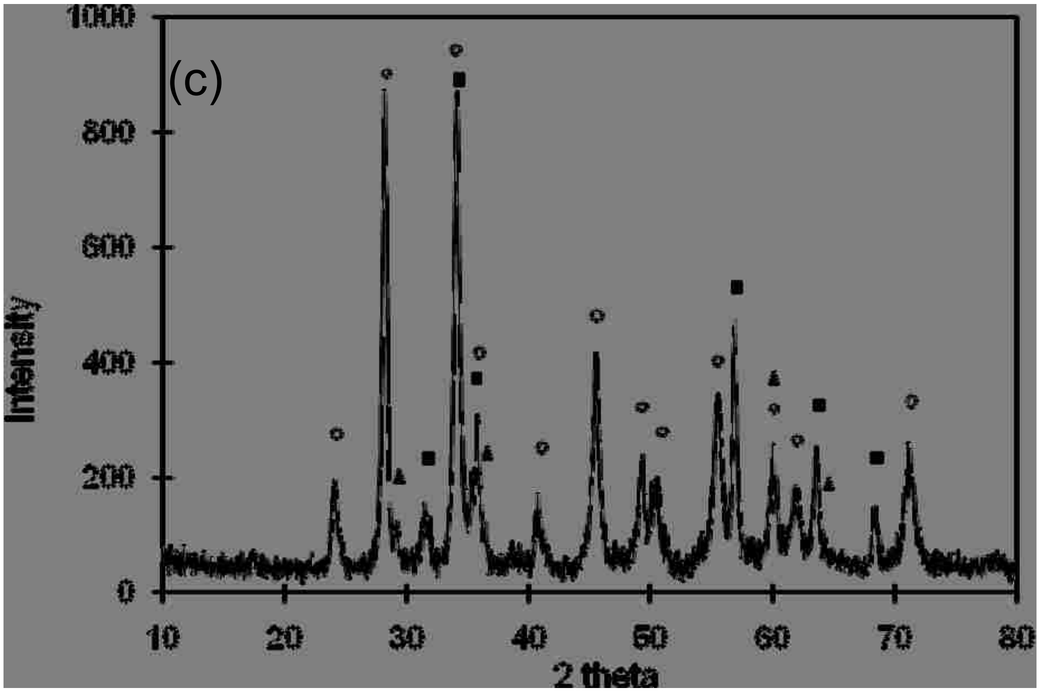

Fig. 4.12 XRD spectrum of (a) Zr-2.5Nb substrate (b) black oxide coating and (c) PEO sample S1.

4.5 Corrosion protection properties of PEO coatings

4.5.1 Potentiodynamic polarization tests

Fig 4.13 shows the polarization curves for the Zr-2.5Nb substrate, a black oxide coated sample, and PEO coated sample S1 which was made using a low current density. Coating S1, prepared using a Na_2SiO_3: KOH=10:1 solution, and the black oxide coating had almost the same corrosion potential which was more positive than the substrate, i.e. both coatings gave some level of corrosion protection. The noise in the polarization curve of the substrate was possibly due to the repeated formation and dissolution of an unstable passive film on its surface: the Zr-2.5Nb shows a passive region that extends from approximately -0.1V to +0.8V. The corrosion current for the coating S1 (6.31×10^{-5} mA/cm^2) was only 1/16th that of the substrate (1.02×10^{-3} mA/cm^2) but 5 times higher than the black oxide coating (1.12×10^{-5} mA/cm^2).

Furthermore, large corrosion craters could be observed by naked eye on the uncoated substrate surface after corrosion testing (see insert in Fig. 4.13). These craters resulted from the fact that the corrosion resistance of Zr-2.5Nb alloy was greatly reduced after the thin, naturally-formed passive film which was dissolved during the corrosion testing. And it can also be observed from Fig. 4.13—at the point E=0.78V, the i_{corr} of the Zr-2.5Nb substrate increased significantly (loss of passivity).

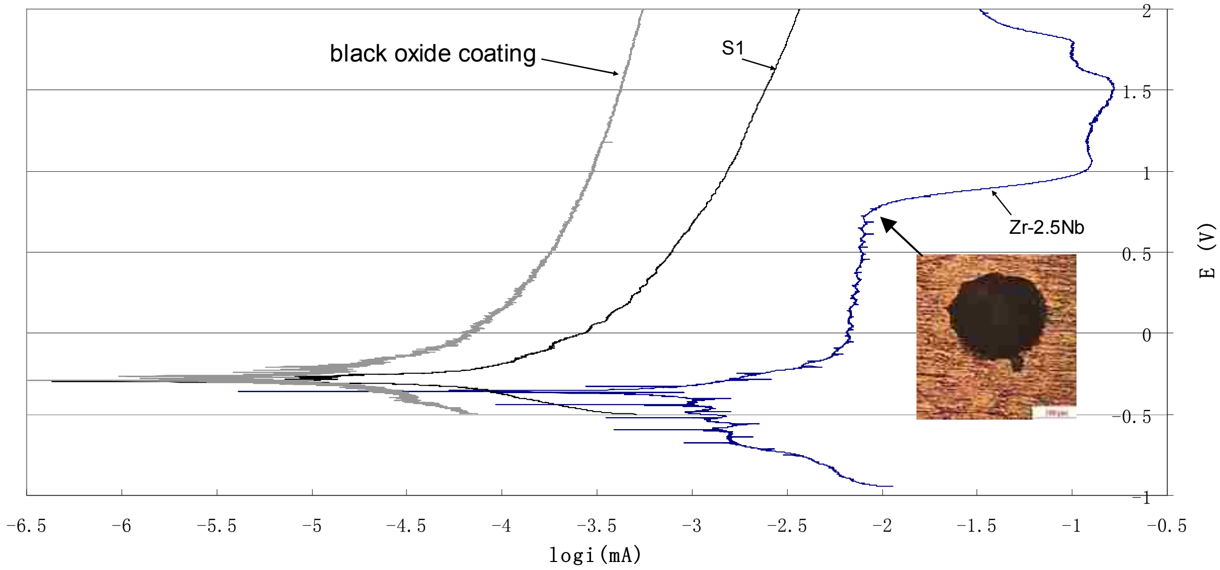

Fig. 4.13 Potentiodynamic polarization curves of the uncoated Zr-2.5Nb, PEO coated sample S1 and black oxide coating.

A summary of the results of all potentiodynamic polarization tests is given in Table 4.2.

The corrosion potentials (E_{corr}), corrosion current density (i_{corr}), and anodic/cathodic Tafel slopes (b_a and b_c) were obtained from the polarization curves. Then, based on an approximately linear polarization at the corrosion potential, the polarization resistance(R_p) values were determined using the relationship[3, 8]:

$$R_p = \frac{b_a \times b_c}{2.303 \times i_{corr}(b_a + b_c)} \tag{4.1}$$

The data in Table 4.2 clearly show the enhanced corrosion protection afforded by the coatings. All PEO coatings, and the black oxide coating, had a much lower i_{corr} compared to Zr-2.5Nb substrate (as much as one to two orders of magnitude) and the E_{corr} values (-0.21V to -0.28V) are higher, i.e. more noble, than the substrate (-0.35V).

From Table 4.2, it can be seen that PEO coatings made in electrolyte I have a better corrosion resistance than those made in electrolyte II. This is in agreement with previous studies of the production of PEO coatings on Al, where alkaline electrolytes are widely used, but too high in pH value may have negative effect on the growth of passive films [2]. All PEO coatings, the black oxide coating, together with the Zr-2.5Nb substrate, are ranked and listed in Table 4.2 according to the corrosion current density (I_{corr}), corrosion potential (E_{corr}) and polarization resistance (R_p), respectively. From Table 4.2, we can make the following conclusions:

(i) The thin commercial black oxide coating showed good corrosion resistance properties in the potentiodynamic polarization tests.

(ii) S3 is the best of all PEO coatings from a corrosion standpoint.

(iii) S6 is the poorest of all PEO coatings from a corrosion standpoint.

(iv) All PEO samples showed improved corrosion resistance compared to the uncoated substrate with improvements in the range of 19 (S6) to 130 (S3) times. The black oxide coating has an R_p value 293 times higher than the substrate.

Table 4.2 Results of potentiodynamic polarization tests (ranking chart) in a 0.2mol/L LiOH solution

Rank	I_{corr} (as low as possible) mA/cm^2	E_{corr} (more positive) V	R_p(high as possible) Ω cm^2
1	Black oxide (1.12E-05)	S5(-0.21)	Black oxide(3.57E+06)
2	S3(1.58E-05)	S3(-0.22)	S3(1.58E+06)
3	S2(5.71E-05)	S1(-0.25)	S2(1.39E+06)
4	S1(6.31E-05)	S4(-0.25)	S1(1.22E+06)
5	S4(7.08E-05)	S2(-0.27)	S4(5.72E+05)
6	S5(1.58E-04)	Black oxide(-0.28)	S5(2.68E+05)
7	S6(2.09E-04)	S6(-0.28)	S6(2.06E+05)
8	Zr-2.5Nb(1.02E-03)	Zr-2.5Nb(-0.35)	Zr-2.5Nb(1.22E+04)

4.5.2 Autoclave experiments

The weight gains of samples versus exposure time in a pressurized 0.05M LiOH solution at 300°C is shown in Fig. 4.14. The weight gain of the PEO coated samples increased rapidly in the first two days and then slowed down. This may be explained by the dissolution of oxygen from solution into the outer layer of the PEO coating which is not very dense, thereby forming ZrO_2 together with other intermediate lower oxides. However, there was a very thin, inner dense layer close to the oxide/metal interface which worked as an excellent barrier to the oxygen ingress, so the corrosion rate after 2 days slowed down. However, after exposure beyond a certain point (transition point), all coated samples had an abrupt increase in corrosion rate. Comparing the two groups with different electrolyte concentrations, it can be seen that samples in Group A had a longer pre-transition period (in the range of 10 to 30 days) than those in Group B (in the range of 5 to 10 days). The weight gains of Group A were almost the same (0.76-0.87%) after 30 days exposure. Due to the spalling of oxide layers in Group B samples, it was difficult to measure the weight gain after 10 days in autoclave. Thus, the weight gain data after the 10-day point in Group B shows a decrease compared to shorter exposure times.

The uncoated Zr-2.5Nb substrate and black oxide coated samples were also tested up to 30 days. As with the PEO-coated samples, the weight of the substrate first increased rapidly because of the formation of a oxide film. This dark color, thin film was a protective to some extent but was not as dense as the PEO coatings. Unlike the PEO coatings in Group B, where coatings were spalled off entirely, the coating formed on the uncoated substrate consists of several thin layers formed parallel to the oxide/metal interface [43]. When a certain thickness of oxide is attained, the outer layer of oxide will crack into small pieces, separate from the sample surface and sink to the bottom of the autoclave. In this case, the weight gain data recorded in the Fig 4.14 (a) for the substrate is much lower than its real value. However, the final weight gain (about 1.18%) is still higher than the PEO coatings. The black oxide coating shows excellent corrosion prevention properties in the first 10 days (better than any of the PEO coated samples). But, for longer exposure times, it exhibited a similar weight gain to the PEO coated samples (0.92% at 30 days exposure).

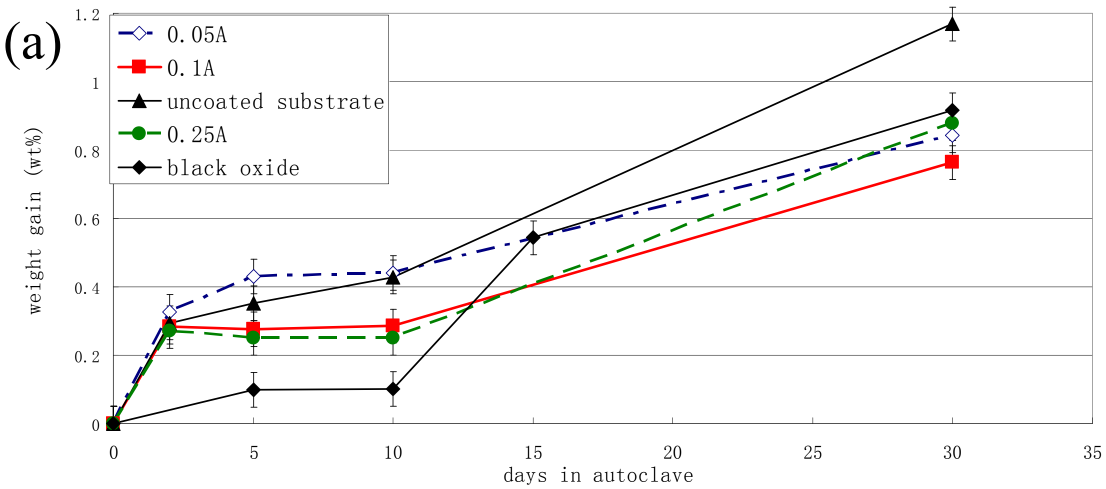

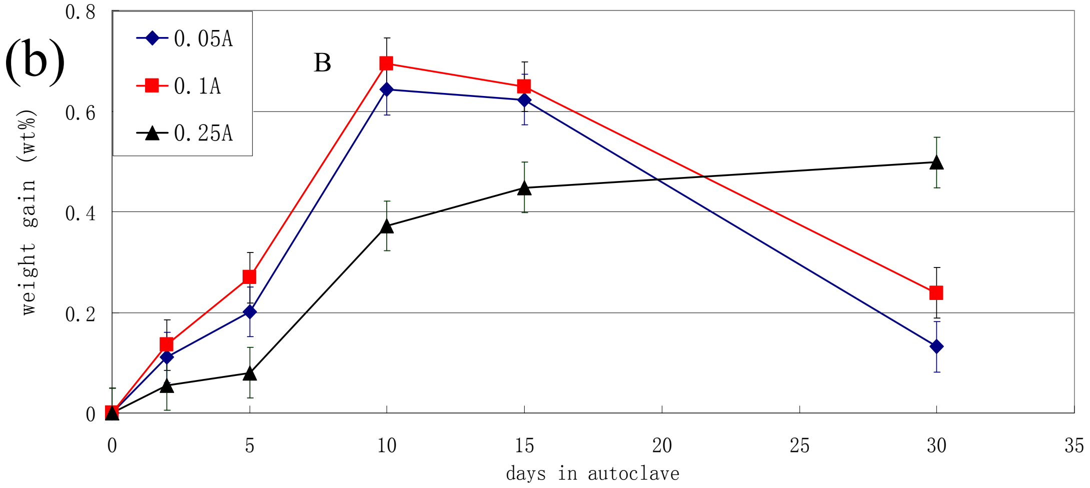

Fig. 4.14 Weight gain vs treatment time: (a) Group A, substrate & black oxide coating and (b) Group B.

4.5.3 SEM micrographs for samples at different exposure times during autoclave experiment.

The surface morphology of the Zr-2.5Nb substrate after 10 days exposure in the autoclave is shown in Fig. 4.15. There are many blister-like features distributed in rows of varying dimensions which are parallel to the axial direction of the pressure tube. This phenomenon might be explained by the elongated α-zirconium grains resulting from extrusion and cold work during fabrication of the pressure tubes. Without protection of the coatings, the thin networks of the β phase which are distributed between the α-phase (Fig. 2.5) were exposed directly to the corrosive medium and the corrosion rate is highest in those phase boundaries [45]. In this case, mainly axial direction strips could be observed in Fig. 4.16 (b). With an increase in oxide thickness, there was an accompanying increase in the compressive stresses which caused many micro-cracks to form inside the oxide. The areas of high corrosion rate protruded from the surface and formed blister-like features. These blisters were also distributed mainly in the extrusion direction (i.e. axial direction).

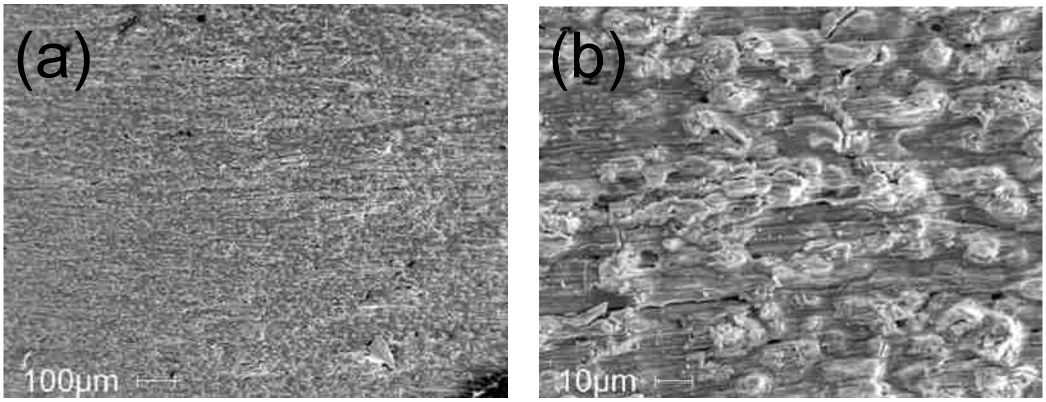

Fig. 4.15 SEM micrographs of surface morphology of Zr-2.5Nb substrate after 10-day exposure in autoclave at different magnifications. There are many blister-like features distributed in lines parallel to the axial direction.

Fig. 4.16 and Fig. 4.17 are SEM micrographs showing the surface morphologies of Group A and Group B PEO coatings, respectively, at different exposure times. The black oxide coating after autoclave experiment is shown in Fig. 4.18.

Fig 4.16 shows the surface morphology of samples in Group A after 5 and 30 days in the autoclave. After 30 days exposure, the coatings were still adherent and protective as shown by their R_p values which were still higher than the substrate. (see section 4.4.5 for full results)

Comparing Fig.4.6 (a) and Figs. 4.16 (a and b), which show the surface morphology of PEO-coated sample S1 at 0, 5 and 30 days exposure, it can be seen that after 5 days exposure, there were many pits on the sample surface, and the surface roughness was increasing because there were small areas of oxide that spalled-off from the coating surface. According to the ‘weight gain curve’ for the first 5 days in Fig. 4.14 (a), the mass loss of oxide was very small. However, after 30 days exposure, the small pits could no longer be seen, Fig. 4.16 (b). It is suggested that they were closed by the compressive stress, caused by the expansion of oxidation inside the coating area when the coating became thicker. At the same time, the outer layer of the coating lost adhesion to the inner layer of coating and “crinkled” in some areas. Microcracks could also be observed on S2 and S3 after 30 days exposure (see Fig. 4.16 (c and d)). It is interesting to see that there are blister-like features observed on the surface of S3 (see Fig. 4.16 (d and e)), the density of which is close to the density of blisters observed on the Zr-2.5Nb sample (see Fig. 4.15 (b)).

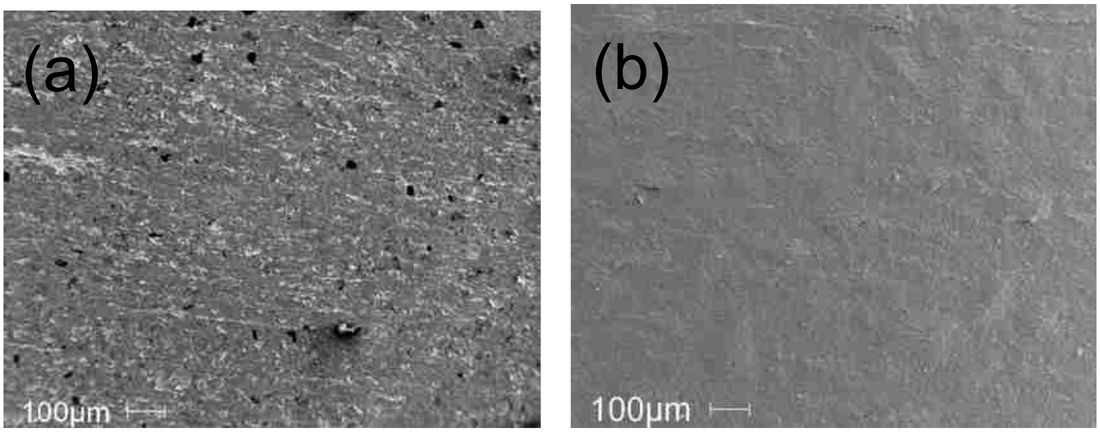

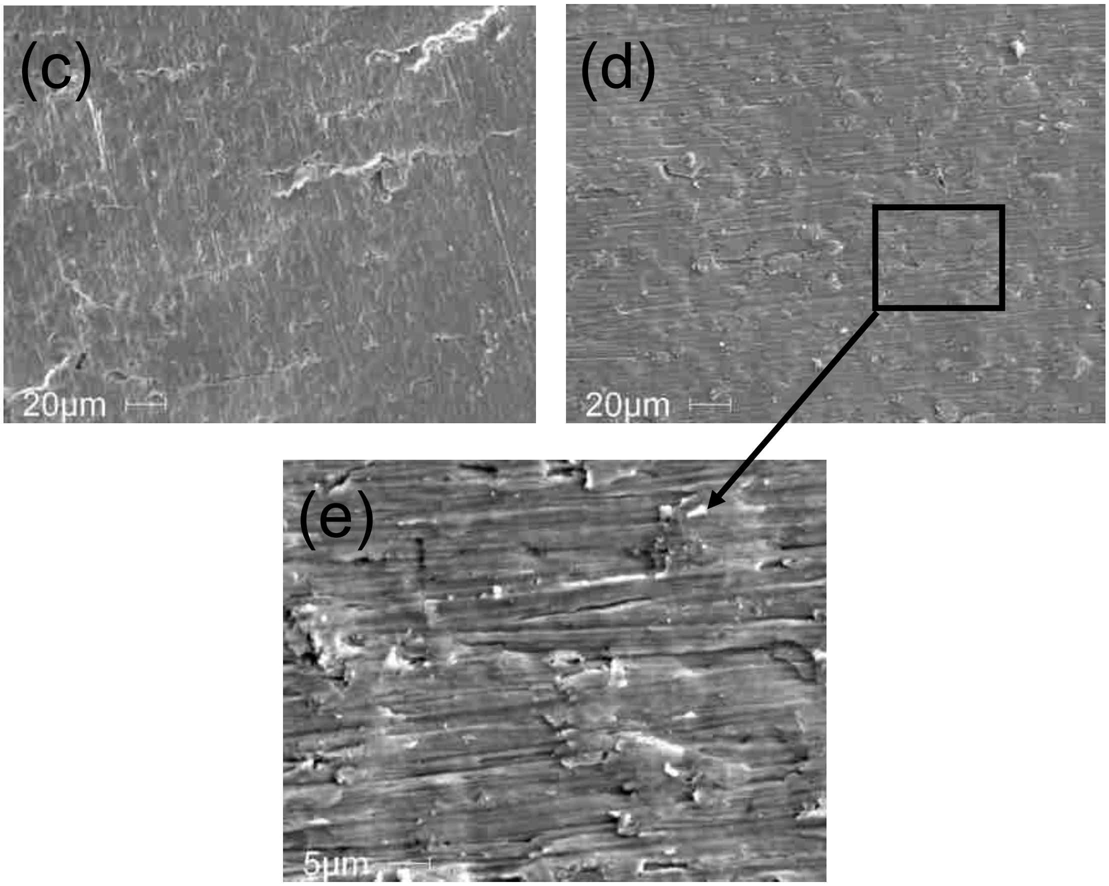

Fig. 4.16 Surface morphologies of Group A PEO coatings at different exposure times in autoclave experiment: (a, b) sample S1 at 5 and 30 days exposure; (c) sample S2 at 30 days exposure and (d and e) sample S3 at 30 days exposure at different magnifications.

Unlike the samples in Group A, Group B samples which were fabricated using a higher pH value electrolyte, showed a total different situation—all the PEO coatings on Group B samples degraded at an early stage during the experiment (around 10 days). Instead of the PEO oxide, a newly formed oxide (Fig. 4.17 (b, c)) quickly grew beneath the initial layer. This new oxide was white, soft and provided very little corrosion protection. The adhesion force between the PEO coating and new oxide was very poor and after 30 days exposure, the PEO coating had spalled-off entirely in large flakes or was ready to spall-off, and a ‘new’ oxide covered the whole surface.

The reasons for the difference in the corrosion behavior between the two Groups of PEO coatings are unclear and require a more detailed study which is beyond the scope of this M.A.Sc thesis. However, some general comments can be made with regard to Group B samples. Fig. 4.17 (a, b, d, e) show the surface morphologies on samples S4, S5 and S6 after 15 days exposure. At this time, both cracked PEO coatings and a soft, new oxide could be observed. For exposure times longer than 15 days, with the spalling-off of the PEO coatings, the weight of the PEO coated samples in Group B decreased dramatically (Fig. 4.14 (b)). The new oxide also grew very quickly after that point and was distributed unevenly on the sample surface (Fig. 4.17 (f)).

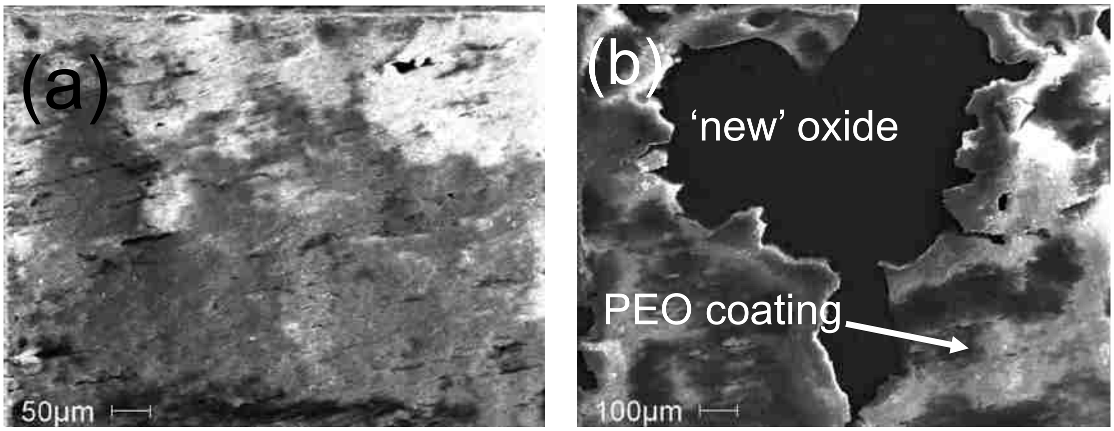

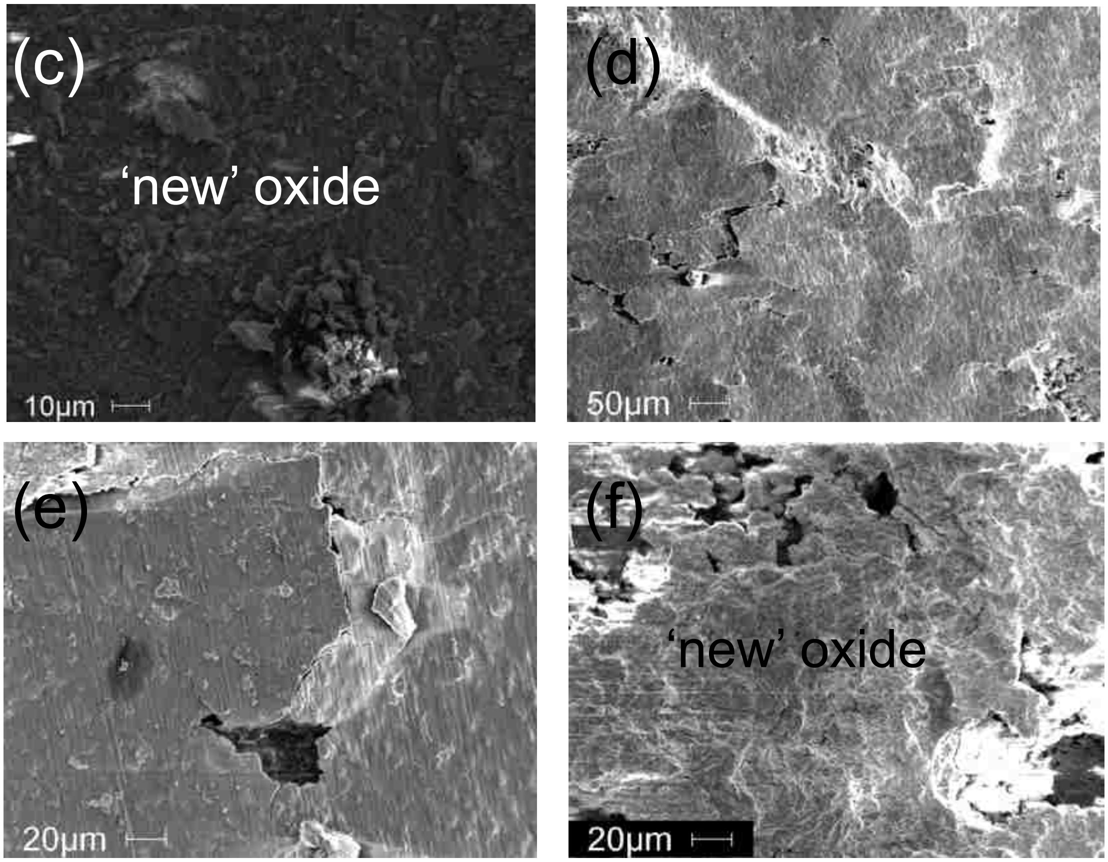

Fig. 4.17 Surface morphologies of Group A PEO coatings at different exposure time in autoclave experiment: (a to c) sample S4 at 15 exposure days under different magnification; (d) sample S5 at 15 exposure days and (e, f) sample S6 at 15 and 30 exposure days.

From Fig. 4.14, it can be seen that the rate of weight gain of the black oxide coated sample was slow for the first few days' exposure. However, after about 10 days exposure, the rate of weight gain increased greatly. From SEM examination, it was seen that a thick, white oxide grew on the top of the black oxide coating (Fig. 4.18), however, this oxide was different from the PEO coatings in its morphology. A flocculent structure with a large amount of pores was formed.

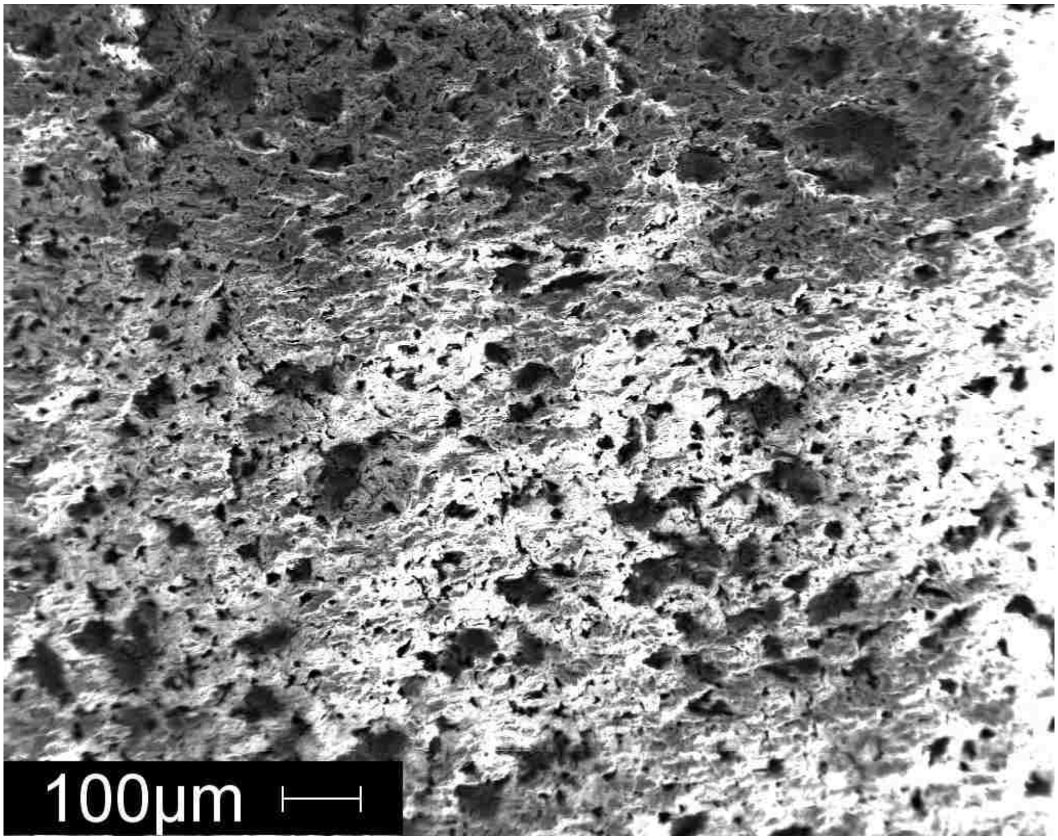

Fig. 4.18 Morphology of the black oxide coating after 30 exposure days in the autoclave corrosion test.

The thicknesses of the oxide film after autoclave exposure was measured using cross-sectional SEM micrographs which are shown in Figs. 4.19 (a) and (b). The thickness was difficult to measure because the ‘new’ oxide was not as dense and adhesive as the PEO coatings and was easily destroyed during polishing. However, some comparisons can still be made from these micrographs. Fig. 4.19 (a) and (b) are the samples S1 and S4 after 30 days exposure. The average coating thickness of S1 was 17.5 µm (PEO coating included) compared to S4 which had a thickness of over 35 µm, without any PEO coating remaining. There was a network of cracks distributed through the oxide layer, especially in the outer layers..

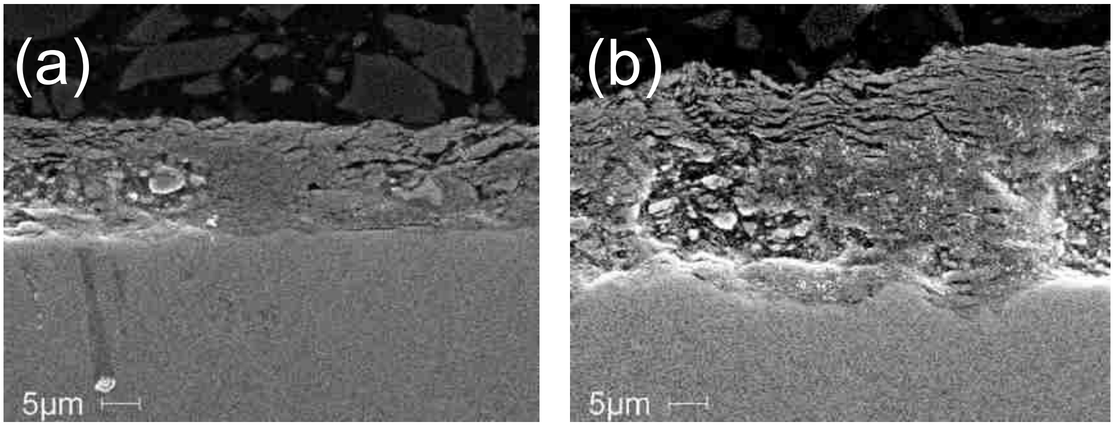

Fig. 4.19 Cross-sectional SEM micrographs distribute the thickness of oxide on PEO-coated samples after 30 days exposure: (a) sample S1 with PEO coating remained and (b) sample S4 without PEO coating remained.

From Figs. 4.19 (a) and (b), it could be suggested that the PEO coating on sample S1 was still blocking the ingress of oxygen and thus slowing down the corrosion rate, although its overall corrosion resistance was decreasing with the increase of exposure time. After 30 days exposure, the oxide thickness on S1 was only half of that on S4. The sudden increase of weight gain was also observed in Group A but the transition point was postponed and the acceleration was smaller compared to Group B and the black oxide coating after the transition point.

Fig. 4.20 shows some photographs of PEO coated samples after 30-exposure day in the autoclave experiment. From Fig. 4.20 we can clearly see that, white and crisp PEO coatings on some samples were separated from the substrate and easily to be spalled off from each surface of the square sample couple. Samples S1 and S2 remained intact whereas S4 and S5, which made using the same current densities, showed a flaking off of the oxide.

Fig. 4.20 Photos showing the spalled-off oxide from PEO coated samples of Group B after 30-day autoclave treatment.

4.5.4 XRD analysis after autoclave tests.

After the autoclave tests, all the sample surfaces were covered by a thick, pearl-white oxide. A small amount of oxide powder spalled off from all samples and sank to the bottom of autoclave. These oxide powders were collected, dried and examined using XRD. Fig. 4.21 shows the XRD patterns of PEO coating S1 and the spalled-off oxide powder after 30 days exposure. Only m-ZrO_2 was detected from the spalled-off powder. This is understandable because the tetragonal phase is not stable at room temperature or 300° C. After the coating spalled off, any internal stresses were released and any t-ZrO_2 would have transformed into m-ZrO_2. According to previous studies [44, 89-91], the existence of t-ZrO_2 inside the coating has a significant effect on the enhancement of the corrosion resistance of coatings on zirconium alloys. From Fig. 4.21 (a), t-ZrO_2 was identified as remaining in the PEO coating S1 after 30 days in the autoclave.

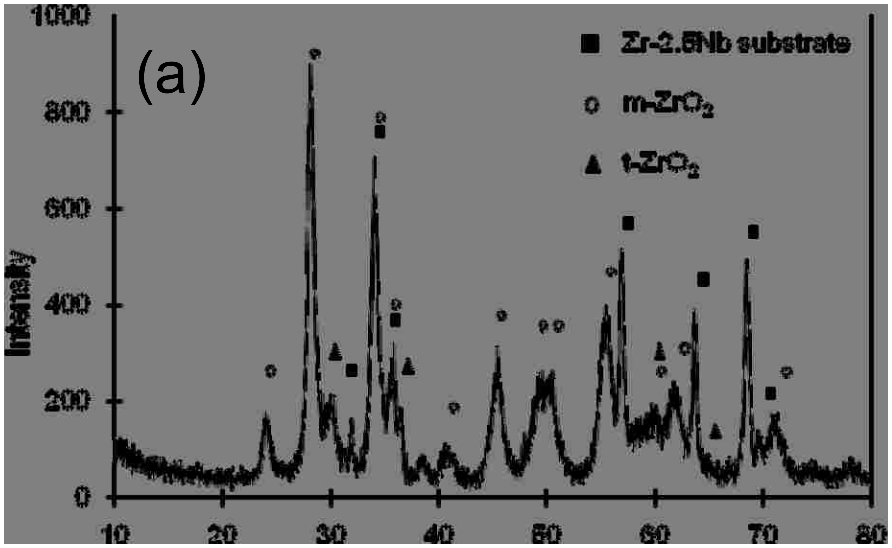

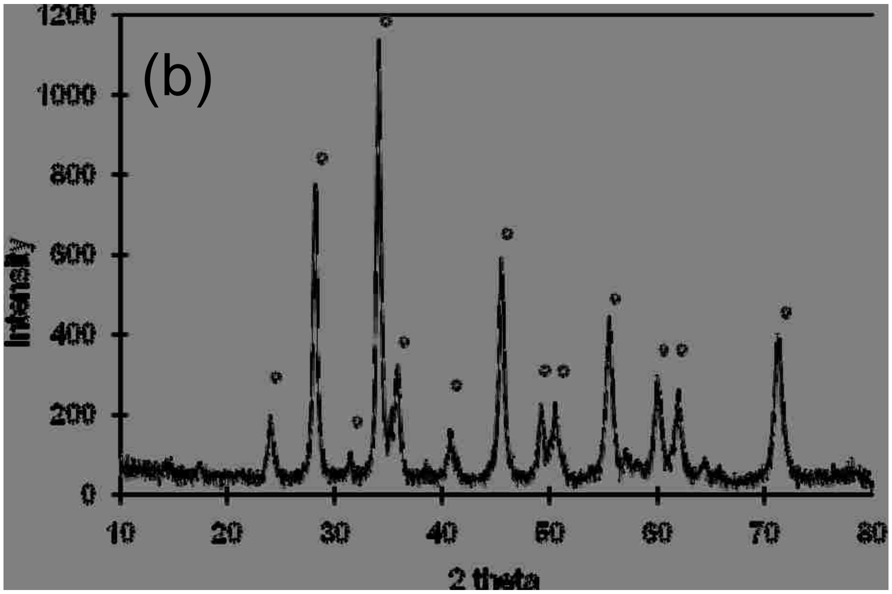

Fig. 4.21 XRD patterns on (a) PEO coating S1 and (b) spalled-off powder after 30 days in autoclave.

4.5.5 Potentiodynamic polarization testing of autoclaved specimens to determine changes in corrosion resistance.

Table 4.3 shows the potentiodynamic polarization results for specimens retested after autoclave testing for predetermined time periods. From Table 4.3, it can be seen that the thin oxide formed in first 5 days exposure in 300°C aqueous environment acts as an excellent oxidation barrier but the overall corrosion resistance of the coated samples decreases with exposure time after some critical exposure time. It can be seen that with the increase of the exposure time, the value of i_{corr} increases greatly and the R_p for both coated and uncoated samples decreased by more than an order of magnitude. The R_p value of coatings of Group B decreased more rapidly than that in Group A. However, it is interesting to note that all PEO coatings had a better corrosion resistance than the 'newly-made' PEO ones after 5 days in autoclave (see Table 4.2 and 4.3). It is suggested that the small pores in 'newly made' PEO coatings were closed by heating in the autoclave for a short period of time.

Table 4.3 Results of the potentiodynamic polarization tests on samples removed from autoclave corrosion tests at fixed time intervals.

Days in autoclave	Samples	i_{corr}(μA/cm^2)	E_{corr}(mV)	R_p(Ωcm^2)
0 day	Zr-2.5Nb	1.02	-330.2	1.22E+04
5 days	Zr-2.5Nb	0.02	-195.5	1.08E+06
	S1	0.015	-205.3	1.23E+06
	S2	0.028	-190.9	1.12E+06
	S3	0.019	-264.2	1.91E+06
	S4	0.029	-202.5	1.77E+06
	S5	0.029	-329.5	1.05E+06
	S6	0.025	-184.2	1.28E+06
10 days	S1	0.122	-251.9	3.38E+05
	S2	0.18	-229.1	2.61E+05
	S3	0.123	-245.4	4.4E+05
15 days	S4	0.206	-186.74	2.38E+05
	S5	0.3	-260.1	1.53E+05

	S6	0.128	-281.7	9.04E+04
30 days	Zr-2.5Nb	0.374	-265.3	9.21E+04
	S1	0.231	-251.9	1.22E+05
	S2	0.313	-127.2	9.31E+04
	S3	0.282	-171.6	1.0E+05
	S4	0.39	-221.8	5.3E+04
	S5	0.273	-193.6	4.98E+04
	S6	0.313	+30.4	6.0E+04

4.5.6 Surface roughness of autoclave exposed samples

As noted previously, the PEO coatings of Group A samples were retained after 30 days in autoclave. With the ingress of oxygen and hydrogen during the autoclave test, the oxide layer became thicker and thicker which also changing the properties of the intial PEO coating—e.g., the wear and corrosion resistance properties decreased and the surface of coating became rougher. Some microcracks which may caused by phase transformation of zirconium dioxide and repeated heating and cooling in the autoclave. Fig. 4.22 shows the suface roughness profile of sample S2 which was measured at different exosure times during the autoclave experiment.

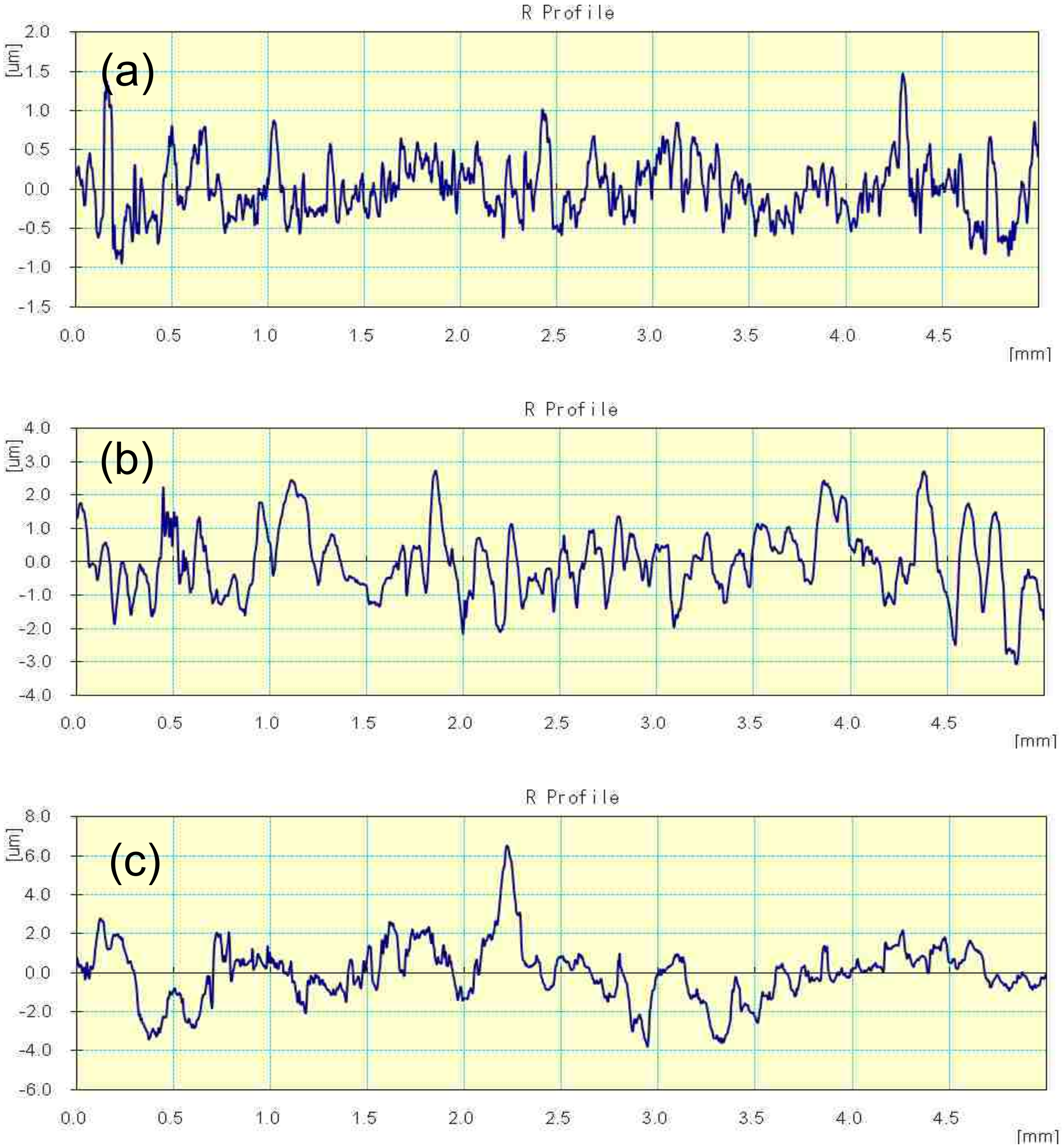

Fig. 4.22 Surface roughness of S2 measured at (a) 5days (b) 10days and (c) 30days exposure in the autoclave experiment.

4.5.7 Nano-hardness testing of autoclave exposed samples

The nano-hardness (H) and elastic modulus (E) were calculated from typical Force-Displacement curves in nano-hardness testing and are listed in Table 4.4.

Table 4.4 Nano-hardness (H) and elastic modulus (E) of PEO coatings and substrate before and after autoclave testing.

PEO coating	Days in autoclave	Zr-2.5Nb substrate	S1	S2	S3	S4	S5	S6
E (GPa)	0	56.25	49.33	48.08	46.35	43.06	65.95	51.71
Hardness (GPa)		0.37	3.18	2.45	2.25	2.62	2.61	3.5
	5	0.95	5.14	4.97	5.22	4.11	4.54	4.82
	10	1.14	3.63	3.08	3.41	X	X	X
	15	X	X	X	X	0.84	0.62	0.77
	30	0.34	2.43	2.03	1.98	0.31	0.34	0.32

From Table 4.4, all the samples, both coated and uncoated ones, showed an increase in the nano-hardness in the first five days in autoclave. This might be explained by the fact that the high temperature and pressure in the autoclave helps to fill in the micro cracks and pores which were caused by discharges during the PEO treatment. For the substrate material, the peak value was found at around five days due to an oxide which was relatively dense and harder than the substrate. However, in the long time autoclave experiment (30 days), the hardness values measured in different groups showed a different trend. For Group A samples the nano-hardness after 30 days exposure was lightly lower than for the as-fabricated PEO coatings. For Group B samples, where the protective PEO coatings fractured and a new and soft oxide took the place of the PEO coating and rapidly thickened, the nano-hardness measured after 30 days exposure was low and was comparable to that found for the substrate at 30 days exposure. Thus, they had a very similar value at the end of autoclave experiment.

4.6 Pin-on-disc tests

4.6.1 Sliding tests under different conditions.

The wear test results are summarized in Table 4.5 for the rotating mode and Table 4.6 for the reciprocating mode tests. Tables 4.5 and 4.6 show that most of the PEO coatings had not failed after a 1000m sliding distance in both rotating and reciprocating modes of testing. The black oxide coating, both under dry and lubricated conditions, showed inferior wear resistance to the PEO-coated materials. After wear testing, roughness data was collected across the wear trace in order to compare the mass losses (Fig. 4.23). A 50m wear distance for the Zr-2.5Nb substrate produced a 10μm-deep wear trace, where is a 1000m wear distance under same load produced only a 1.5μm-deep trace for PEO-coated sample S4. As mentioned in section **4.2**, the PEO coating (5μm thick) was not penetrated.

Table 4.5 Wear/Failure distances of coated & uncoated samples under rotating mode.

Rotating mode	Zr-2.5Nb	S1	S2	S3	S4	S5	S6
dry/2N/ v=0.1m/s	50m	1000 m	970m (failed)	1000 m	1000 m	1000 m	910m (failed)

Table 4.6 Wear/Failure distances of coated & uncoated samples under reciprocating mode.

Reciprocating mode	Zr-2.5Nb	Black oxide coating	PEO S1
dry/2N	×	40m (failed)	1000m
lubricated/5N/v=0.08m/s	50m	75m (failed)	1000m

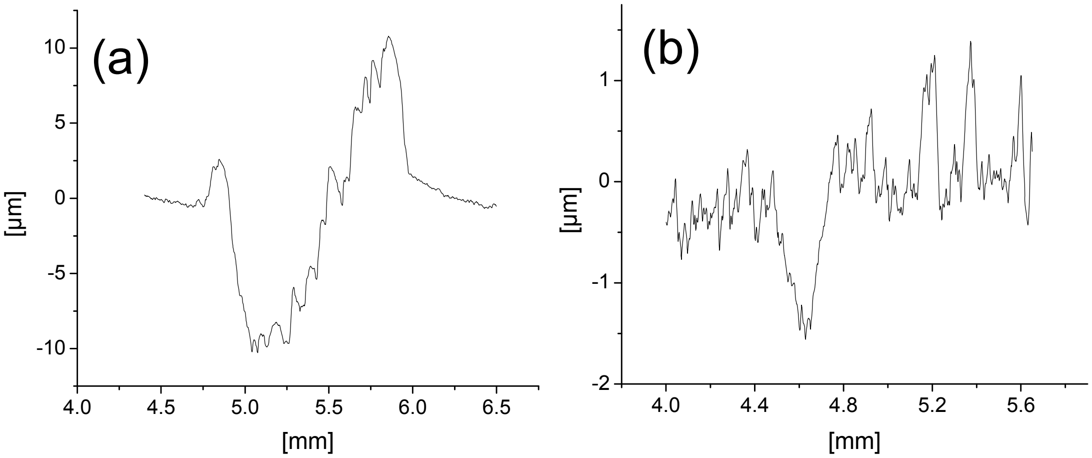

Fig. 4.23 Transverse roughness on the wear trace of (a) Zr-2.5Nb substrate and (b) PEO coated sample S4 under 2N load, dry air, rotating mode with 50m and 1000m sliding distances respectively.

4.6.2 SEM micrographs of wear traces

Fig. 4.24 shows the wear traces for selected samples tested in the dry and rotating mode. 1000m wear distance was used on sample S1 after PEO process and after 5 and 10 exposure days in autoclave (Fig. 4.24 (a-d)). Grinding polish was observed inside the wear trace of S1 (Fig. 4.24 (b)) due to the high hardness of the PEO coating. The coating material had been compacted by the normal load. This behavior was also seen in the 5-day autoclaved sample S1 but was more distinct. This was because the PEO layer had been hardened due to autoclaving for 5 days. The hardness values of that 5-exposure day are also higher than that of newly made PEO coatings (Table 4.3). However, after 10 days in the autoclave, the outer layer of PEO coating on sample S1 was softened (both by autoclave treatment and heat produced during wear tests) and was pushed away from the wear trace and became wear debris. However, the dense oxide underlayer was still intact. Fig. 4.24 (e, f) are the wear trace on sample S4 after 10-day autoclave treatment. The 1000m wear test caused the penetration of the PEO coating and the wear loss from the substrate. Inside the wear trace, deep scratches (grooves), caused by “three body” debris wear, were observed on the soft substrate material. After the total 30 exposure days in autoclave, the oxide on the surface of S4 turned to be a white, soft, uneven one, which is shown in Fig. 4.24 (g). Only a 50 meter wear distance was used with a 2N load removed the oxide layer and caused the deep and wide scratches. The uncoated sample with 5-day autoclave treatment showed evidence of plastic deformations in its wear trace (Fig. 4.24

(h, i)). Scaly debris was observed after 50m wear test which means the oxide formed in the autoclave was relatively soft.

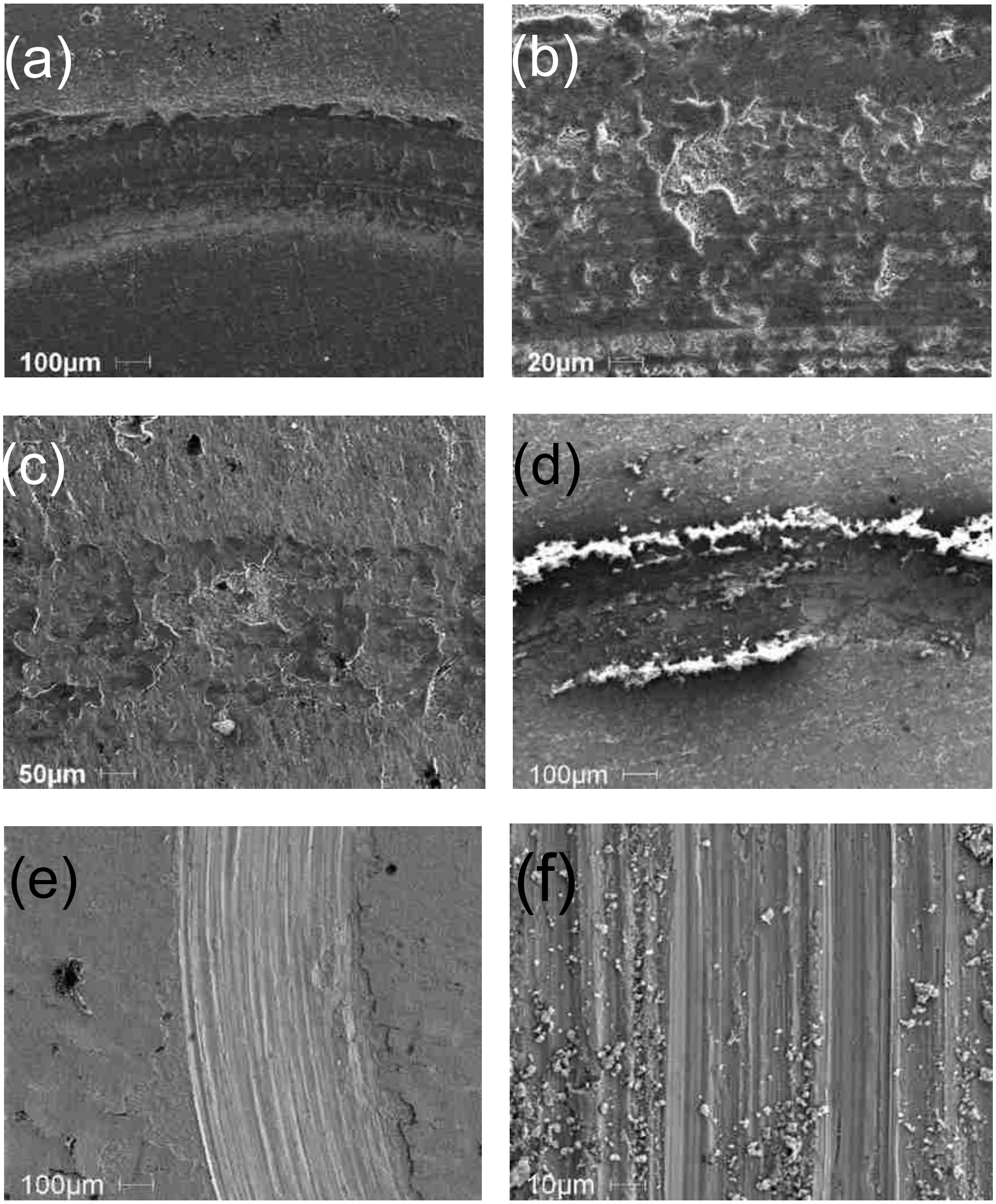

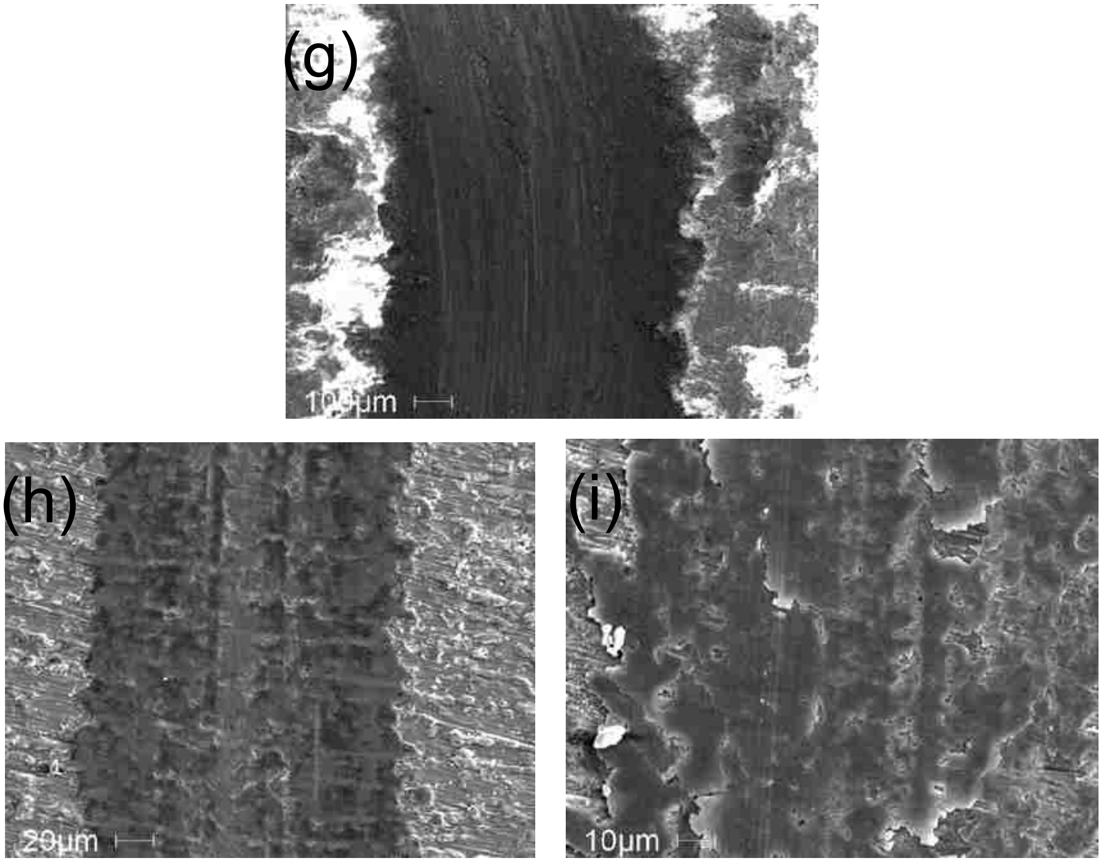

Fig. 4.24 Rotating wear trace on different PEO coatings and substrate: (a, b) S1, 1000m, before autoclaved; (c, d) S1 1000m, 5 and 10 days in autoclave; (e, f) S4, 1000m, 10 days in autoclave; (g) S4, 50m, 30 days in autoclave and (h, i) Zr-2.5Nb substrate 50m, 5 days in autoclave.

After the rotating mode wear tests, sample S1 was chosen for comparison with the black oxide coating because of its excellent wear resistance. Because of the curved surface of black oxide coating sample, a reciprocating mode was used. The wear traces are shown in Fig. 4.25. 1000m and 75m wear distances were used on S1 and black oxide coating (failure distance), respectively, under the same 5N load and lubricated condition. The wear trace on black oxide coating was much wider and deeper than that on sample

S1 and it is clearly seen that all coating material was removed from the substrate. Abrasive wear is clearly observed on black oxide coating with wear debris presents in the wear track. Much debris piled up at the two edges of wear track (Fig. 4.25 (c)). For PEO coating S1, no obvious abrasive wear and material removal was observed. Thus the PEO coating had much better wear resistance than the black oxide coating and less wear debris was produced which could lead to contamination of the service environment.

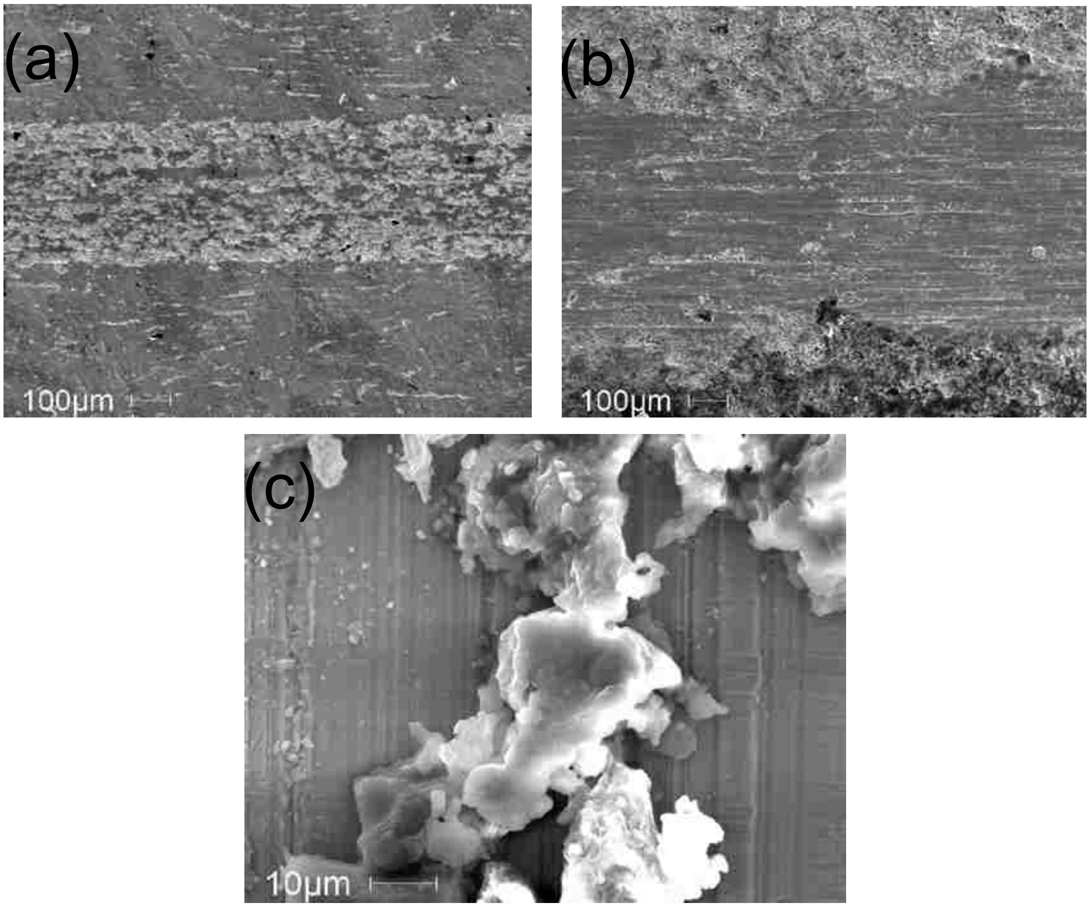

Fig. 4.25 SEM showing wear traces of (a) PEO sample S1, (b) the black oxide coating. (c) piling up of debris at the edge of wear track

4.7 Summary

Given the ‘two-stage’ corrosion kinetics of zirconium and its alloys, coating with a higher thickness coating can shorten the transition time when exposed to high temperature/pressure water/Li+-added water, and thereby, shorten the service life of a nuclear reactor. A DC power source was used in this study to make thin coating by the PEO treatment on a Zr-2.5Nb alloy, which is widely used in the manufacture of pressure tubes. Three levels of current density: 0.05A/cm^2, 0.1 A/cm^2 and 0.25 A/cm^2 were used in two types of electrolytes. The process time, which depends on the current density, is relatively short (<4min) to prevent any strong and intense micro-discharges in Stage III for all six sets of PEO coatings. SEM micrographs showed that the thickness of coatings S1 and S4, which were produced at a lower current density, was much more even. Fewer cracks could be seen in the coating areas when compared with the specimens produced at higher current densities (S2, S3 and S5, S6). Higher current density also made a much more porous coating and an irregular substrate-oxide interface, which can enhance the adhesion property of coating [9].

Potentiodynamic polarization tests showed the commercial-used black oxide coating has an excellent corrosion resistance in diluted LiOH solution. The PEO coatings made using the Na_2SiO_3: KOH=10:1 electrolyte had higher corrosion resistance compared to these made in a 1:1 solution. PEO coatings S3 and S6 showed the best and worst corrosion resistance, respectively. However, all PEO coatings showed a much better corrosion resistance compared to the uncoated substrate with improvements in the range of 19 (S6) to 130 (S3) times. The black oxide coating has an R_p value as much as 293 times higher than the substrate.

According to the XRD examination, the PEO coatings were mainly composed of m-ZrO_2 and t-ZrO_2 phases, but the content of t-ZrO_2 was much lower than the m-ZrO_2. This t-ZrO_2 was remained in the PEO coatings after 30 days in autoclave and was beneficial in the enhancement of the corrosion resistance. A low concentration of oxygen was found in the ~1 µm thick black oxide coating which formed a metastable Zr_3O.

The PEO coatings made in a dilute silicate electrolyte were proven to have much better corrosion resistance and lower weight gains than the Zr-2.5Nb substrate after 30 days exposure in the autoclave. The black oxide coating had a very low weight gain value in the first 10 exposure days but at 30 days, the final weight gain was slightly higher than the PEO coatings. The original thin black oxide coating turned to a thick, flocculent structure. The PEO coatings on the samples of Group A were intact and were still protective after 30 days exposure. However, Group B samples showed poor corrosion resistance after 15 days exposure, when most of the PEO coatings spalled off. A new, soft and white oxide took the place of previous PEO coating, which grew quickly but had an inferior corrosion resistance.

During the autoclave tests, potentiodynamic polarization tests showed the corrosion resistance of both coated and uncoated samples decreased rapidly with increase of exposure time. Group B samples had the lowest polarization resistance.

5 μm thick PEO coatings had a much higher wear resistance than the commercial autoclaved black oxide coating under a 2N and 5N normal loads. Grinding polish was observed on the PEO coatings of which the wear resistance was enhanced by the hardness of the coating surface. The commercially-produced black oxide coating had a low wear resistance that was just slightly better than the substrate: this is attributed to the low thickness of such a layer and the rough inner substrate surface of the pressure tube.

Chapter 5 CONCLUSIONS AND FUTURE WORK

In this study, Plasma Electrolytic Oxidation (PEO) was utilized to produce 5 to 6μm thick coatings on a Zr-2.5Nb alloy using a DC power source in two types of Na_2SiO_3+ KOH electrolytes at different concentrations of 8 g/L: 0.8 g/L and 8 g/L: 8 g/L. Three levels of current density: 0.05A/cm^2, 0.1 A/cm^2 and 0.25 A/cm^2 were used in the two electrolytes. The process time, which depends on the current density, is relatively short (<4min) to prevent strong and intense micro-discharges in Stage III for all six sets of PEO coatings. All six sets of PEO coatings were produced and made comparisons with the commercial black oxide coating and the uncoated substrate in corrosion and wear resistance properties. The conclusions are shown as follows:

5.1 Effects of process parameters of PEO treatment on coating surface morphology

One or two Stages of PEO treatment were used to produce six sets of PEO coatings in this study. At low current density (0.05A/cm^2), no discharges were observed. Under such conditions, a smooth coating surface was made with an even thickness. At high current density (0.25A/cm^2), strong and intense micro-discharges were observed from the very early stages. A large amount of pores were present in the coatings and many micro-cracks, parallel to the substrate-oxide interface existed inside the coating. A more irregular substrate-oxide interface resulted from the strong discharges. Surface profiles showed that the surface of PEO coating became rougher with the increase of thickness. However, in short periods of treatment (before Stage 3 in the PEO process), a small current density produces a smoother coating surface because the larger current density brought intense discharges. These micro-pores and micro-cracks seems to have no obvious effect on the corrosion and tribological behaviors in further tests.

5.2 The comparisons with PEO coatings, black oxide coating and Zr-2.5Nb substrate

5.2.1 Potentiodynamic polarization tests

Potentiodynamic polarization tests showed the commercial-used black oxide coating has an excellent corrosion resistance in dilute LiOH solution. PEO coatings made in Na_2SiO_3: KOH=10:1 solution had higher corrosion resistance compared to those made in a 1:1 solution. PEO coatings S3 and S6 showed the best and the worst corrosion resistance, respectively. However, all PEO samples showed much better corrosion resistance compared to the uncoated substrate with improvements in the range of 19 (S6) to 130 (S3) times. The black oxide coating even has an R_p as much as 293 times higher than the substrate.

5.2.2 Autoclave tests

During the autoclave tests, potentiodynamic polarization tests showed the corrosion resistance of both coated and uncoated samples decreased rapidly with the increase of exposure time. Group B samples had the lowest polarization resistance.

The weight gain of the black oxide coating was low in the first 10 days, however, after 30 days exposure, its final weight gain was slightly higher than the PEO coatings in Group A. The corrosion behavior of Group B coatings showed a great difference to the Group A samples in the autoclave tests. Due to the spalling-off of PEO coatings at around 15 days exposure, the weight gain were impossible to be accurately measured. After the failure of protective PEO coatings, a new soft and less protective oxide was produced under the previous coating. This oxide grew rapidly and had a very high thickness after the autoclave tests. Potentiodynamic polarization tests showed that the new oxide had a very low corrosion resistance, even compared to the passive film on the surface of Zr-2.5Nb substrate.

5.2.3 Wear tests

Compared to the soft Zr-2.5Nb substrate, all coated samples showed higher wear resistance according to the pin-on-disc tribological tests. Grinding polish was observed on the PEO coatings of which the wear resistance was enhanced by the hardness of the coating surface. The commercially-produced black oxide coating had a low wear resistance that was just slightly better than the substrate: this is attributed to the low thickness of such a layer and the rough inner substrate surface of pressure tube.

5.3 Future work

It is necessary to conduct a more detailed insight study on the processing parameters for PEO treatment, including such parameters as, different types of current and electrolyte. In this way, we may be able to obtain a coating with better corrosion behavior when exposed to high temperature/pressure conditions. There is a need to better understand the growth fundamentals of PEO coatings on zirconium alloys improve the mechanical and corrosion properties.

Additionally, longer exposure time (up to several years) tests are required to determine the corrosion resistance properties of PEO coated samples. Different concentrations of LiOH solutions could, perhaps, be used to study the corrosion kinetics and hydrogen pick-up of PEO coatings.

REFERENCES

[1] Kee-Nam Choo, Young-Suk Kim, Hydrogen uptake and corrosion behavior of Zr-2.5Nb pressure tubes in Wolsong Unit 1, Journal of Nuclear Materials 297(2001)52-56

[2] L.O. Snizhko, & A.L. Yerokhin, Anodic processes in plasma electrolytic oxidation of aluminum in alkaline solutions. Electrochimical Acta. 49(2004)2085-2095,

[3] A. L. Yerokhin, X. Nie, A. Leyland, A Matthews, S.J. Dowey. Plasma electrolysis for surface engineering Surface and Coating Technology. 122(1999)73-93.

[4] R. C Barik, J. A. Wharton, R.J.K. Wood, K. Stokes R.& R. L. Jones Corrosion, erosion and erosion-corrosion performance of PEO deposited Al_2O_3 coatings. Surface & Coating Technology. 199(2005) 158-167.

[5] Y. J. Guang, , Y. Xia, & G. Li. Growth mechanism and corrosion behaviour of ceramic coatings on Al produced by autocontrol AC pulse PEO. Surface & Coatings Technology. 202 (2008) 4602-4612.

[6] A. L. Yerokhin, A. Shatrov, V. Samsonov, P. Shashkov, A. Pikington, A. Leyland & A. Matthew. Oxide ceramic coatings on aluminum alloys produced by a pulsed bipolar plasma electrolytic oxidation process Surface & Coatings Technology. 199(2005) 150-157.

[7] A. Ghasemi, V.S. Raja, C. Blawert, W. Dietzel and K.U.Kainer. Study of the structure and corrosion behaviour of PEO coatings on AM50 magnesium alloy by EIS Surface & Coatings Technology. 202(2008) 3513-3518.

[8] A.L. Yerokhin, X. Nie., A. Leyland. And A. Matthews. Characterisation of oxide films produced by PEO of a Ti-6Al-4V alloy. Surface and Coating Technology. 130(2000) 195-206.

[9]W. Xue, Q. Zhu, Q. Jin, M. Hua, Characterization of ceramic coatings fabricated on zirconium alloy by plasma electrolytic oxidation in silicate electrolyte Material Chemistry and Physics 120(2010) 656-660.

[10] E. Matykina, R. Arrabal, P. Skeldon, G.E. Thompson, P. Wang, P. Wood, Plasma electrolytic oxidation of a zirconium alloy under AC conditions. Surface & Coatings Technology 204 (2010) 2142–2151.

[11] Canadian Nuclear Association, "Innovating Today for a Brighter Future", Retrieved, Aug. 20, 2010, from www.cna.ca/english/pdf/nuclearfacts/2009/CNA_Booklet_09.pdf.

[12] B. Rouben, "Basic CANDU Design", Retrieved, Aug. 20, 2010, from www.unene.ca/un802-2004/session08/basic_candu_design.pdf

[13] R.A. Holt, In-reactor deformation of cold-worked Zr–2.5Nb pressure tubes. Journal of Nuclear Materials 372 (2008) 182–214.

[14] M.P. Puls, Assessment of aging of Zr-2.5Nb pressure tubes in CANDU^{TM} reactors, Nuclear Engineering and Design 171(1997) 137-148.

[15] G.D. Moan, C.E. Coleman, E.G. Price, D.K. Rodgers and S. Sagat, Leak-before-break in the pressure tubes of CANDU reactors International Journal of Pressure Vessels and Piping, 43(1990)1-21.

[16] "Candu Reactor Construction", CANDU Fundamentals, Retrieved, Aug. 20, 2010

from http://canteach.candu.org/library/20040711.pdf

[17] J.S. Foster, G.L. Brooks, An overview of the early CANDU program prepared from information provided by John S. Foster. CANDU Origins and Evolution-Part 1 of 5. Retrieved, Aug. 20, 2010 from http://canteach.candu.org/library/20010301.pdf

[18] J. Lin, H. Li, J.A. Szpunar, R. Bordoni, A.M. Olmedo, M. Villegas, A.J.G. Maroto, Analysis of zirconium oxide formed during oxidation at 623K on Zr-2.5Nb and Zircaloy-4, Materials Science and Engineering A 381(2004) 104-112.

[19] R. Krishnan, M.K. Asundi, Zirconium alloys in nuclear technology, Proc. Indian Acad. Sci. (Engg. Sci.) 4(1981) 41-56

[20] J.R. Theaker, R. Choubey, G.D. Moan, S.A. Aldridge, L. Davis, R.A. Graham, C.E. Coleman, Fabrication of Zr-2.5Nb pressure tubes to minimize the harmful effects of trace elements, Zirconium in the Nuclear Industry: Tenth International Symposium, ASTM STP 1245 (1994) 221-242.

[21] D.K. Rodgers, C.E. Coleman, M. Griffiths, G.A. Bickel, J.R. Theaker, I. Muir, A.A. Bahurmuz, S.St. Lawrence, M. Resta Levi. In-reactor performance of pressure tubes in CANDU reactors. Journal of Nuclear Materials 383(2008)22-27.

[22] D. Srivastava, G.K. Dey and S. Banerjee, Evolution of Microsturcture during fabrication of Zr-2.5wt pct Nb alloy pressure tubes, Metallurgical and Materials Transactions A, 26A(1995) 2707-2718.

[23] Y. Toda, H.Nakagawa1, T. Koyama and T. Miyazaki, An analysis of the phase decomposition in Nb–Zr alloy based on the system free energy theory, Materials Science

and Engineering A, 255 (1998)90-97.

[24] D.O. Northwood, X. Meng-Burany, B.D. Warr, Microstructure of Zr-2.5Nb alloy pressure tubing, Zirconium in the Nuclear Industry. ASTM STP 1132, American Society for Testing and Materials, Philadelphia, American Society for Testing and Materials, Philadelphia, pp. 1 56-172, 1991.

[25] P. Hovington, P.T. Pinard, M. Lagace, L. Rodrigue, R. Gauvin, M.L. Trudeau, Towards a more comprehensive microstructure analysis of Zr–2.5Nb pressure tubing using image analysis and electron backscattered diffraction (EBSD). Journal of Nuclear Materials 393 (2009) 162–174.

[26] Y.H. Jeong, K.O. Lee, H.G. Kim, Correlation between microstructure and corrosion behavior of Zr–Nb binary alloy, Journal of Nuclear Materials 302 (2002) 9–19.

[27] N Petigny, P. Barberis, C. Lemaignan, C. Valot, M. Lallemant. In situ XRD analysis of the oxide layers formed by oxidation at 743 K on Zircaloy 4 and Zr–1NbO. Journal of Nuclear Materials 280(2000) 318-330.

[28] M. Oskarsson, E. Ahlberg, U. Andersson, K. Pettersson. Characterisation of pre-transition oxides on Zircaloys. Journal of Nuclear Materials. 297(2001) 77-88.

[29] A. Yilmazbayhan, A.T. Motta, R.J. Comstock, G.P. Sabol, B. Lai, Z.H. Cai. Structure of zirconium alloy oxides formed in pure water studied with synchrotron radiation and optical microscopy: relation to corrosion rate. Journal of Nuclear Materials 324(2004) 6-22.

[30] J. Godlewski, How the tetragonal zirconia is stabilized in the oxide scale that is

formed on a zirconium alloy corroded at 400°C in steam. Zirconium in the Nuclear Industry: 10th International. Symposium, ASTM STP 1245, Baltimore (MD); 1994. p. 663-686.

[31] D. Pecheur, F. Lefebvre, A.T. Motta, C. Lemaignan, J-F. Wadier. Precipitate evolution in the Zircaloy-4 oxide layer. Journal of Nuclear Materials. 189(1992) 318.

[32] P. Bossis, J. Thomazet, F. Lefebvre. Oxide growth under irradiation. Zirconium in the Nuclear Industry. 13th International Symposium, ASTM STP 1423, Annecy, France; 2001. p. 190-221.

[33] J.L. Bechade, R. Dralet, P. Goudeau, P. Yvon. Studies of Zirconium alloy oxide layers using synchrotron radiation. Material Science Forum. (347-349)(2000) 471-478.

[34] V. Vrtlikova, J. Jaros, J. Cmakal, L. Belovsky. International topical meeting on LWR fuel performance. Park City (UT): ANS; 2000. p.401.

[35] H-S Yoo, J-G Chung, A review of pressure tube failure accident in the CANDU reactor and methods for improving reactor performance. Journal of the Korean Nuclear Society, 30 (3)(1998) 262-272.

[36]. B. Cox, Some thoughts on the mechanisms of in-reactor corrosion of zirconium alloys. Journal of Nuclear Materials 336 (2005) 331–368

[37] Final report of a coordinated research project 1998-2002. Delayed hydride cracking in zirconium alloys in pressure tube nuclear reactors. Retrieved, Aug. 20, 2010 from http://www-pub.iaea.org/MTCD/publications/PDF/te_1410_web.pdf.

[38] Maria Roth, Rameshwar Choubey, Christopher Coleman, Iain Ritchie, Measurement

of DHC Velocity in CANDU Pressure Tubes. Transactions of the 17th International Conference on Structural Mechanics in Reactor Technology (SMiRT 17) Prague, Czech Republic, (2003)17 –22;

[39] R.N. Singh, N. Kumar, R. Kishore, S. Roychaudhury, T.K. Sinha, B.P. Kashyap, Delayed hydride cracking in Zr-2.5Nb pressure tube material.l Journal of Nuclear Materials 304 (2002) 189–203

[40] D.O. Northwood, U. Kosasih, Corrosion and hydriding behavior of Zr-2.5Nb wt. pct Nb alloy nuclear reactor pressure tubing. Journal Materials for Energy Systems. 4(1) (1982)3-15.

[41] W. Qin, C. Nam, H.L. Li, J. A. Szpunar. Effects of local stress on the stability of tetragonal phase in ZrO_2 film. Journal of Alloys and Compounds 437 (2007) 280–284.

[42] B. Cox, The oxidation and corrosion of Zirconium and its alloy, J. Electrochemical Society, Vol 108(1961) 24-30.

[43] B.G. Parfeno, V. V. Gerasimov & G. I. Venediktova. Corrosion of Zirconium and Zirconium alloys IPST Press, Wiener Bindery Ltd., Jerusalem. 1969.

[44] H.J. Beie, A. Mitwalsky, F. Garzarolli, H. Ruhmann, H.J. Sell, Examinations of corrosion mechanism of Zr alloys, Zirconium in Nuclear Industry. Tenth, International Symposium, ASTM STP 1245, American Society for Testing and Materials, (1994) 615-643.

[45] Y. Ding, D.O. Northwood, SEM examination of the oxide-metal interface formed during the aqueous corrosion of a Zr-2.5 wt% Nb alloy Journal of Materials Science,

27(1992) 1045-1052

[46] W. Qin, C. Nam, H.L. Li, J.A. Szpunar, Tetragonal phase stability in ZrO_2 film formed on zirconium alloys and its effects on corrosion resistance. Acta Materialia. 55(2007)1695-1701.

[47] P. Barberis, Zirconia powders and Zircaloy oxide films: tetragonal phase evolution during 400°C autoclave tests. Journal of Nuclear Materials. 226 (1995) 34-43.

[48] J.L. Lin, H.L. Li, C. Nam, J.A. Szpunar, Analysis on volume fraction and crystal orientation relationship of monoclinic and tetragonal oxide grown on Zr–2.5Nb alloy. Journal of Nuclear Materials.334(2004) 200-206.

[49] H.G. Kim, T.H. Kim, Y.H. Jeong, Oxidation characteristics of basal (0 0 0 2) plane and prism ([illegible]) plane in HCP Zr. Journal of Nuclear Materials. 306(2002) 44-53.

[50] T. Pauporte, J. Finne, Impedance spectroscopy study of anodic growth of thick zirconium oxide films in H_2SO4, Na_2SO_4 and NaOH solutions, Journal of Applied Elecrochemistry. 36 (2006) 33-41.

[51] T. Pauporte, J. Finne, A. Kahn-Harari, D. Lincot, Growth by plasma electrolysis of zirconium oxide films in the micrometer range. Surface & Coatings Technology 199(2005)213-219.

[52] A. Bibb and J. Faschia, Trans. S.c. AIME, 230, No. 3, 415 (1964)

[53] N. Christodoulou, A.R. Causey, R.A. Holt, C.N. Tome, N. Badie, R.J. Klassen, R. Sauve, C.H. Woo, Modeling in-reactor deformation of Zr-2.5Nb pressure tubes in CANDU power reactors. Zirconium in the Nuclear Industry: Eleventh International

Symposium, ASTM STP 1295, American Society for Testing and Materials, 1996, pp. 518-537.

[54] D.D. Macdonald, The point defect model for the passive state, Journal of the Electrochemical Society, 139(1992) 3434-3449

[55] O. Pensdo-Rodriguez, M. Urquidi-Macdonald, D.D. Macdonald, Electrochemical behavior of Lithium in alkaline aqueous electrolytes. I. Thermodynamics. Journal of the Electrochemical Society, 146(1999) 1318-1325.

[56] E. Hillner, J.N. Chirigos, The effect of Lithium hydroxide and related solution on corrosion rate of Zircaloy in 680F water. Report WAPD-TM-307, Bettis Atomic Power Laboratory, Pittsburgh, Westinghouse Electric Corporation, 1962.

[57] B. Cox, C.G. Wu, Transient effects of lithium hydroxide and boric acid on Zircaloy corrosion. Journal of Nuclear Materials 224 (1995) 169-178.

[58] N. Ramasubramanian, P.V. Balakrishnan, Aqueous chemistry of Lithium hydroxide and boric acid and corrosion of Zircaloy-4 and Zr-2.5Nb alloys. Zirconium in the nuclear industry, in: 10th International Symposium, ASTM STP 1245, American Society for Testing and Materials, Philadelphia, 1994, p. 378-399.

[59] J. Krýsa,, J. Maixner, P.Matejka, V.Vrtılková, Structure and composition of zirconium oxide films formed in high pressure water with different Li^+ concentration at 360°C. Materials Chemistry and Physics 63 (2000) 1–8.

[60] B. Zhou, W. Liu, Q. Li, M. Yao, Mechanism of LiOH aqueous solution accelerating corrosion rate of zircaloy-4, Chinese Journal of Materials Research. 18(2004) 225-231.

[61] Y.S. Kim, S.C. Kwon, Crystallization and degradation of zirconium oxide in various pH solutions. Journal of Nuclear Materials 270 (1999) 165–173.

[62] F. Garzarolli, H. Seidel, R. Tricot, J.P. Gros, Oxide growth mechanism on Zirconium alloys, Zirconium in Nuclear Industry, Ninth International Symposium, ASTM STP1132, American Society for Testing and Materials, 1991, pp 395-415.

[63] B. Cox and C. Wu, Dissolution of zirconium oxide films in 300°C LiOH. Journal of Nuclear Materials, 199(1993)272-284.

[64] B. Cox, M. Ungurelu, Y.M. Wong, C. Wu, Mechanism of LiOH degradation and H_3BO_3 repair of ZrO_2 films, ASTM STP 1295, American Society for Testing and Materials, West Conshohocken, PA, 1996, pp. 114-136

[65] Young-Ho Lee, Hyung-Kyu Kim, Effect of spring shapes on the variation of loading conditions and the wear behavior of the nuclear fuel rod during fretting wear tests. Wear 263(2007) 451-457.

[66] G.A. Markov, G.V. Mmarkova, USSR Patent 526961, Bulletin of Inventions, 32(1976) 1.

[67] A.V. Nikolaev, G.A. Markov, B.I. Peshchevitskij, Izv. SO AN SSSR. Ser. Khim. Nauk, 5(12)(1977) 32.

[68] L.A. Snezhko, L.A. Beskrovnyj, Yu.M. Nevkrytyj, V.I. Tchernenko, Zashch. Met., 16(3)(1980) 365.

[69] L.A. Snezhko, G.V. Rozenboym, V.I. Tchernenko, Zashch. Met., 17(5)(1981), 618.

[70] L.A. Snezhko, V.I. Tchernenko, Elektron. Obrab. Mater., (2)(1983) 25.

[71] L.A. Snezhko, V.I. Tchernenko, Elektron. Obrab. Mater., (4)(1983) 38.

[72] V.I. Tchernenko, L.A. Snezhko, C.B. Tchernova, Zashch., Met. 20(3)(1984) 454.

[73] L.A. Snezhko, S.G. Pavlus, V.I. Tchernenko, Zashch. Met., 20(4)(1984) 292.

[74] G.A. Markov, M.K. Mironova, O.G. Potapova, Izv. AN SSSR. Ser. Neorgan. Mater., 19(7)(1983)1110.

[75] A.A. Petrosyants, V.N. Malyshev, V.A. Fyedorov, G.A. Markov, Trenie Iznos, 5(2)(1984)350.

[76] V.N. Malyshev, S.I. Bulychev, G.A. Markov, V.A. Fyedorov, A.A. Petrosyants, V.V. Kudinov, M.H. Shorshorov, Fiz. Khim. Obrab. Mater., (1)(1985)82.

[77] V.A. Fyedorov, V.V. Belozerov, N.D. Velikosel'skaya, S.I. Buychev, Fiz. Khim. Obrab. Mater., 4(1988)92.

[78] V.S. Rudnev, P.S. Gordienko, preprint no. 3384-B87, Inst. Khimii DVO AN SSSR, Vladivostok, 1987.

[79] O.A. Khrisanfova, P.S. Gordienko, preprint no. 2986-B89, Inst. Khimii DVO AN SSSR, Vladivostok, 1987.

[80] P.S. Gordienko, P.M. Nedozorov, L.M. Volkova, T.P. Yarovaya, O.A. Khrisanfova, Zashch. Met., 25(1)(1989) 125.

[81] A. L. Yerokhin, V.V. Lyubimov, R.V. Ashitkov, Phase formation in ceramic coatings during plasma electrolytic oxidation of aluminum alloys Ceramics International 24 (1998)1-6.

[82] H. Zhou, Z. Li, J. Du, J. Zhang, . Ji, Oxide coatings on zirconium alloy deposited by

AC microarc oxidation. Rare Met. Mater. Eng. 34(2005) 1113-1333.

[83] D. Zhang, X. Bai, B. Chen, F. Liu, Z. Wu, Microarc oxidation of zircaloy-4, Rare Met. Mater. Eng. 32 (2003) 658–661.

[84] M.D. Klapkiv, N.Yu. Povstyana, H.M. Nykyforchyn. Production of conversion oxide-ceramic coatings on zirconium and titanium alloys. Materials Science, 42(2) (2006) 277-286.

[85] W. Xue, Z. Deng, Y. Lai, R. Chen, Analysis of phase distribution for ceramic coatings formed by microarc oxidation on aluminum alloy, Journal of American Ceramic Society 81(1998) 1365–1368.

[86] W. Xue, Z. Deng, R. Chen, T. Zhang, H. Ma, Microstructure and properties of ceramic coatings produced on 2024 aluminum alloy by microarc oxidation, Journal of Material Science. 36 (2001) 2615–2619.

[87] D.O. Northwood, U. Kosasih. Corrosion and hydriding behavior of Zr-2.5 wt. pct Nb alloy nuclear reactor pressure tubing. J. Materials for Energy Systems, 4(1)(1982) 3-15.

[88] E. Bardal, Corrosion and Protection, Springer-Verlag London Berlin Heidelberg, USA, 2004.

[89] J. Godlewski, J.P. Gross, M. Lambertin, M. Wadier, J.F. Weidinger. Raman spectroscopy study of the tetragonal-to-monoclinic transition in zirconium oxide scales and determination of overall oxygen diffusion by nuclear microanalysis of O^{18}. Zirconium in the Nuclear Industry in: 9th International Symposium. vol. 1132, ASTM-STP, 1991, p. 416-436.

[90] A.J.G. Maroto, R. Bordoni, M. Villegas, A.M. Olmedo, M.A. Blesa, A. Iglesias, P. Koenig, Growth and characterization of oxide layers on zirconium alloys Journal of Nuclear Materials. 229 (1996) 79-92.

[91] Y.P. Lin, J. Deluca, On the effects of heat treatment and surface orientation on corrosion and hydrogen ingress of Zr–2.5Nb pressure tube material. Journal of Nuclear Materials 265 (1999) 1-11.

VITA AUCTORIS

Ying Chen was born in 1984 in Wuhan, Hubei, P.R. China. She obtained her B.Sc. from Huazhong University of Science and Technology in Material Processing and Control Engineering in 2002. She is currently a candidate for the Master's degree in Engineering Materials at the University of Windsor and hopes to graduate in Fall 2010.